

# Strange hadron production in heavy ion collisions from SPS to RHIC

C. Blume<sup>1</sup> and C. Markert<sup>2</sup>

<sup>1</sup>Institut für Kernphysik,

Johann Wolfgang Goethe-Universität Frankfurt, Frankfurt, Germany.

<sup>2</sup>University of Texas at Austin, Austin, Texas 78712, USA.

October 22, 2018

## Abstract

Strange particles have been a very important observable in the search for a deconfined state of strongly interacting matter, the quark-gluon plasma (QGP), which is expected to be formed in ultra-relativistic heavy ion collisions. We review the main experimental observations made at the Super Proton Synchrotron (SPS) at CERN, Geneva, and at the Relativistic Heavy Ion Collider (RHIC) at Brookhaven National Laboratory (BNL). The large amount of recently collected data allows for a comprehensive study of strangeness production as a function of energy and system size. We review results on yields, transverse mass and rapidity spectra, as well as elliptic flow. The measurements are interpreted in the context of various theoretical concepts and their implications are discussed. Of particular interest is the question whether strange particles are in any way sensitive to a partonic phase. Finally, a compilation of experimental data is provided.

## Contents

<b>1</b>	<b>Introduction</b>	<b>3</b>
1.1	Strangeness enhancement as QGP signal . . . . .	4
<b>2</b>	<b>Theoretical aspects</b>	<b>5</b>
2.1	Recent developments . . . . .	5
2.2	Transport models . . . . .	6
2.3	Statistical models . . . . .	9
<b>3</b>	<b>Experimental overview</b>	<b>12</b>
3.1	Basic observations . . . . .	12
3.2	Experimental techniques . . . . .	13
3.2.1	Charged kaons . . . . .	14
3.2.2	Hyperons and $K_S^0$ . . . . .	15
3.2.3	Corrections . . . . .	17

<b>4</b>	<b>Energy dependence</b>	<b>18</b>
4.1	Strangeness enhancement at different energies . . . . .	18
4.2	Structures in the energy dependence of particle yields . . . . .	23
4.2.1	The $K/\pi$ ratios . . . . .	23
4.2.2	Other particle ratios . . . . .	25
4.2.3	The $\phi$ Meson . . . . .	27
4.3	Spectra . . . . .	30
4.3.1	Transverse momentum spectra . . . . .	30
4.3.2	Rapidity spectra . . . . .	34
<b>5</b>	<b>System size dependence</b>	<b>38</b>
5.1	Core and corona model . . . . .	40
5.1.1	Centrality dependence . . . . .	40
5.1.2	Comparison of different collision systems . . . . .	43
5.2	Scaling with $N_{\text{part}}$ and $N_{\text{bin}}$ . . . . .	44
<b>6</b>	<b>Strangeness at intermediate and high <math>p_t</math></b>	<b>45</b>
6.1	Baryon to meson ratios . . . . .	46
6.2	Nuclear suppression factors ( $R_{\text{AA}}$ and $R_{\text{CP}}$ ) . . . . .	47
<b>7</b>	<b>Elliptic flow <math>v_2</math> of strange particles</b>	<b>49</b>
7.1	$v_2$ scaling as a function of momentum . . . . .	49
7.2	Partonic versus hadronic flow . . . . .	51
<b>8</b>	<b>Conclusions</b>	<b>53</b>
<b>9</b>	<b>Data compilation</b>	<b>55</b>
9.1	Energy dependence . . . . .	55

Table 1: Properties of the strange particles discussed in this review [10]. Listed are the valence quark content, the strangeness  $S$ , the isospin, spin and parity  $I(J^P)$ , the mass and the decay channels which are most important for experiments, together with their branching ratio (B.R.) and decay length  $c\tau$ .

Particle	Quarks	$S$	$I(J^P)$	Mass (MeV/ $c^2$ )	Decay particles	B.R. (%)	$c\tau$ (cm)
$K^+$ ( $K^-$ )	$u\bar{s}$ ( $\bar{u}s$ )	+1 (-1)	$\frac{1}{2}(0^-)$	493.677	$\mu^+\nu_\mu$ ( $\mu^-\bar{\nu}_\mu$ )	63.55	371.2
$K_S^0$	$d\bar{s}, s\bar{d}$	—	$\frac{1}{2}(0^-)$	497.614	$\pi^+ \pi^-$	69.2	2.68
$\phi$	$\bar{s}s$	0	$0(1^-)$	1019.455	$K^+ K^-$	48.9	$4.63 \times 10^{-12}$
					$e^+ e^-$	$2.95 \times 10^{-2}$	
					$\mu^+ \mu^-$	$2.87 \times 10^{-2}$	
$\Lambda$ ( $\bar{\Lambda}$ )	$uds$ ( $\bar{u}\bar{d}\bar{s}$ )	-1 (+1)	$0(\frac{1}{2}^+)$	1115.683	$p \pi^-$ ( $\bar{p} \pi^+$ )	63.9	7.89
$\Xi^-$ ( $\bar{\Xi}^+$ )	$dss$ ( $\bar{d}\bar{s}\bar{s}$ )	-2 (+2)	$\frac{1}{2}(\frac{1}{2}^+)$	1321.71	$\Lambda \pi^-$ ( $\bar{\Lambda} \pi^+$ )	99.887	4.91
$\Omega^-$ ( $\bar{\Omega}^+$ )	$sss$ ( $\bar{s}\bar{s}\bar{s}$ )	-3 (+3)	$0(\frac{3}{2}^+)$	1672.45	$\Lambda K^-$ ( $\bar{\Lambda} K^+$ )	67.8	2.46

## 1 Introduction

This review article attempts to summarize the main ideas and observations concerning strangeness in heavy ion reactions that have emerged during the SPS and RHIC program. Heavy ion collisions at these energies are believed to create energy densities that allow to explore states of matter beyond the deconfinement phase transition predicted by quantum chromodynamics (QCD). It separates matter composed of interacting hadrons from a new state of matter, the so-called quark-gluon plasma (QGP), where the confinement of quarks and gluons inside hadrons is removed. The order of this phase transition is not finally established. While for a vanishing baryonic chemical potential  $\mu_B = 0$  different lattice QCD studies agree on a cross over type, the situation for  $\mu_B > 0$  is still unclear. The exact value of the critical temperature  $T_C$  for  $\mu_B = 0$  is also still under debate. While according to [1]  $T_C$  lies in the range 146 – 170 MeV, depending on the investigated order parameter, the authors of [2] find critical temperatures between 180 – 200 MeV. Several calculations predict that the cross over line will turn into a first order phase transition [3, 4, 5], thus giving rise to the presence of a critical point in the QCD phase diagram, while other lattice QCD investigations result in a cross over for all  $\mu_B$  [6].

The study of strange hadron production always played a special role in the investigation of QGP matter. Initially this was motivated by the early suggestion that an enhanced production of strange particles, relative to p+p collisions, might provide a signature of a QGP formation. Even though strangeness enhancement has been established experimentally, many new theoretical developments have shed new light on the experimental facts. Over the years also many unexpected experimental findings have altered the viewpoint on strangeness as an observable. Strange particles have also been instrumental in the investigation of new phenomena that appeared in heavy ion physics (e.g. quark number scaling of elliptic flow). Table 1 summarizes the properties of the different strange particle species that have been measured in heavy ion reactions. After the bulk of the heavy ion program at the SPS has finished and the RHIC program has passed its 10th year, this is a good point in time to take a snapshot of the current situation and to summarize the main observations.

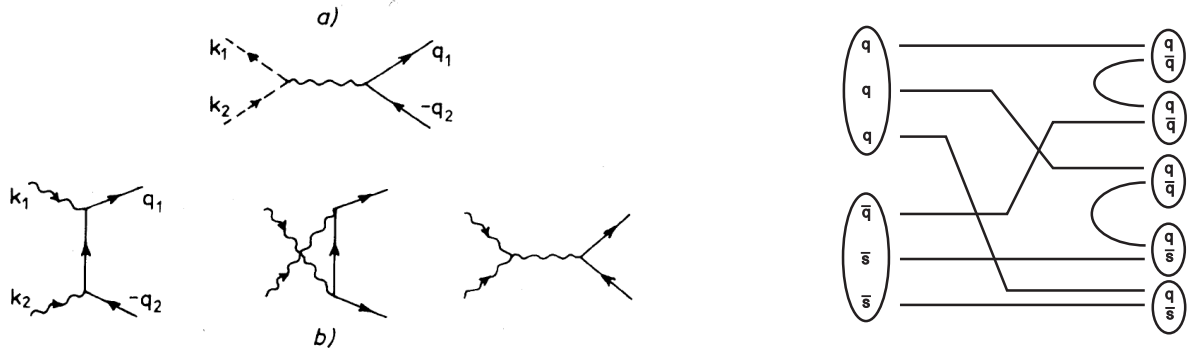


Figure 1: Left: The lowest order QCD diagrams for  $s\bar{s}$  production ((a)  $q\bar{q} \rightarrow s\bar{s}$ , (b)  $gg \rightarrow s\bar{s}$ ) [7]. Right: Schematic picture for the reaction  $\Xi^- + N \rightarrow 3\pi + 2K$  [34].

## 1.1 Strangeness enhancement as QGP signal

The main motivation for measuring strange particles in heavy ion reactions is the expectation that their production rates per participating nucleon should be enhanced with respect to elementary nucleon-nucleon collisions, if a quark-gluon plasma is formed. Strangeness enhancement has been among the first signals suggested for a QGP state [7, 8, 9]. The argumentation by Rafelski and Müller is based on two considerations. One is that in a plasma of quarks and gluons strangeness can be easily produced via pair production of strange-anti-strange quark-pairs. The basic processes are the fusion of two gluons or of two light quarks into a  $s\bar{s}$ -pair (see also left panel of Fig. 1):

$$g + g \leftrightarrow s + \bar{s} \quad q + \bar{q} \leftrightarrow s + \bar{s} \quad (q = u, d). \quad (1)$$

For these reactions the  $Q$ -value corresponds to only the current mass of the produced  $s\bar{s}$ -pair  $Q_{\text{QGP}} = 2m_s \approx 200$  MeV [10]. In contrast, the energetically cheapest way of producing strangeness in a nucleon-nucleon reaction is via associated production channels:

$$N + N \rightarrow N + \Lambda + K. \quad (2)$$

In this case the mass difference and thus the  $Q$ -value is already much higher:  $Q_{\text{ass.}} = m_\Lambda + m_K - m_N \approx 670$  MeV. As a consequence it should be much easier to generate strangeness once a plasma state has been formed.

The second important point is that the equilibration times of partonic reactions, especially due to the gluon fusion process, are much shorter than the ones of hadronic reactions. The difference is especially large, if rare multi-strange (anti-)baryons are considered. In a partonic scenario with typical temperatures of  $T = 200$  MeV equilibration times of  $\tau_{\text{QGP}}^{\text{eq}} \approx 10$  fm are theoretically achievable in an ideal gas of quarks and gluons [7]. This is on the order of the total duration of a heavy ion reaction, measured from the first collisions to the final freeze-out of the hadrons. However, the timespan of the QGP phase will be still shorter than this, so that these partonic processes might not be sufficient to drive the system to a complete chemical equilibrium. On the other hand, it was found in [9], that in a gas of free hadrons, including resonances, the typical times to reach an equilibrium state depend strongly on the strange particle species. While for particles with strangeness  $|S| = 1$ , like the kaon and  $\Lambda$ , chemical equilibrium might be attainable after  $\tau_{\text{HG}}^{\text{eq}}(K) \approx 30$  fm, the timescales for rare (anti-)hyperons should be an order of magnitude longer. Following these arguments, it would thus be very difficult to produce multi-strange particles ( $\Xi$ ,  $\bar{\Xi}$ ,  $\Omega^-$ ,  $\bar{\Omega}^+$ ) in large abundances in a hadron resonance gas, while the presence of a QGP would be reflected in much higher production rates of these particles. In the latter case, the multi-strange particles would just form via quark coalescence at freeze-out and the yields

should be close to the chemical equilibrium expectation. A review of these theoretical considerations can be found in [11, 12].

## 2 Theoretical aspects

In the following we review the basic theoretical ideas that motivate the measurement of strange particles in heavy ion reactions. Beginning with the early suggestion of strangeness enhancement as a signature for a QGP formation, we discuss the further evolution of this idea and alternative approaches. Since transport and statistical models are widely employed for the interpretation of strangeness data, we discuss their main features in two extra sections.

### 2.1 Recent developments

Since these early calculations mentioned above, the theoretical understanding of strangeness production has evolved further. An overview over more recent theoretical developments is given in [13]. One important point is the fact that the assumption of an ideal gas, as used in the calculations in [7, 9], is not valid for heavy ion reactions. As the data on elliptic flow at RHIC have shown, the matter produced in heavy ion collisions at high energies corresponds in its properties rather to a liquid with very low viscosity [14, 15, 16, 17]. Results from lattice QCD indicate that QGP matter is characterized by the presence of strong correlations and bound states, which will prevail for temperatures significantly larger than the critical temperature [18, 19, 20]. Therefore, it is inappropriate to treat partonic scattering processes non-perturbatively, as done in the original calculations. Attempts to take this into account, e.g. by hard thermal loop resummation [21], cut-off model for gluons [22], and massive, thermal gluons [23, 24, 25], seem to indicate that the partonic equilibration times might rather increase [13]. However, this issue is still not solved and further theoretical developments in this direction are needed. New insights into the problem of equilibration in a QGP might arise from approaches such as parton cascades [26] or the investigation of plasma instabilities [27]. Both result in a very fast equilibration on timescales equal or even below the expected QGP lifetimes in heavy ion reactions. Still, quantitative evaluations of the implications for strangeness production are missing.

Another aspect relevant for strangeness production in heavy ion collisions is that some features of particle production observed at RHIC for intermediate transverse momenta  $p_t$ , such as baryon-meson ratios and  $v_2$  scaling of elliptic flow, have raised new interest in quark coalescence as the possibly dominating hadronization process in this  $p_t$  region. Coalescence has been suggested very early on [28] and is an important ingredient of the original line of arguments to suggest strangeness enhancement as a signature for QGP formation [7, 8, 9]. Recent implementations of this idea [29, 30, 31, 32, 33] have been successful in describing the basic features of the measurements (see discussion in Section 6.1).

In the recent years also new mechanisms to generate strange particles in a hadron gas have been suggested. These include multi-meson fusion processes, such as

$$\bar{Y} + N \leftrightarrow n \pi + n_s(\bar{Y}) K, \quad (3)$$

which can additionally contribute to the yield of strange anti-baryons in a dense hadronic medium [34].  $n_s(\bar{Y})$  denotes the number of anti-strange quarks in anti-hyperon  $\bar{Y}$ . The right panel of Fig. 1 shows a scheme for the reaction  $\Xi + N \rightarrow 3\pi + 2K$  at the quark level, whose back reaction might give a sizable contribution to the  $\Xi$  rates, since in a hot and dense fireball the number densities  $n$  and  $n_s(\bar{Y})$  may be high enough. However, at RHIC energies this effect seems not to be sufficient for an equilibration during the lifetime of the hadronic state of the reaction [35, 36]. In [37] it has been pointed out that the contribution from hadronic many body collisions should be strongly enhanced close to the phase boundary between hadron gas and QGP, due to a rapid increase of the particle densities with

temperature in the vicinity of  $T_C$ . The observation of equilibrated strangeness yields might therefore be interpreted as a direct evidence for a phase transition. Another approach that would explain a fast equilibration inside the lifetime of the hadronic phase is the inclusion of so-called Hagedorn states [38, 39]. Hagedorn states (HS) are high mass resonances produced near  $T_C$  that follow an exponential mass spectrum [40, 41] and provide an efficient way of producing (anti-)baryons and kaons via reactions such as  $n\pi \rightarrow \text{HS} \rightarrow n'\pi + B\bar{B}$  and  $n\pi \rightarrow \text{HS} \rightarrow n'\pi + K\bar{K}$  due to their large decay widths.

Another point of view is based on the argument that particle production via the strong interaction always leads to a configuration of maximum entropy, only constrained by energy, baryon number, and strangeness conservation [42, 43, 44]. The observed particle abundances would thus not result from a dynamical equilibration, but are a consequence of the hadronization process. Therefore strangeness yields would always be close to their equilibrium value and an enhancement in A+A collisions is rather due to a suppression in p+p collisions due to the much stronger effect of the conservation laws.

Strangeness production in a hadron gas would also be enhanced, if hadron masses decrease due to medium modifications inside the hot and dense fireball and thus lead to reduced  $Q$  values for hadronic reactions. At the chiral phase transition, which lattice QCD predicts to happen before [1] or in coincidence with [2] the deconfinement transition, the masses of the strange mesons should approach to ones of non-strange mesons, leading to a flavor equilibrated state [13]. In [45] it has been investigated within a chiral SU(3) model for the chemical and thermal equilibrium case to what extent a chiral phase transition is reflected in the observable particle ratios. Since this turns out to have a large effect, the experimentally determined particle ratios can only be understood, if the chemical freeze-out happens slightly below the chiral phase transition line.

## 2.2 Transport models

Hadronic transport models provide an important baseline for comparisons to the experimentally observed strangeness production. Since these models are based on hadronic degrees of freedom and string excitation only, they allow to explore to what extent the observed features of the data can be understood in a purely hadronic scenario. They can therefore provide a benchmark that, to a certain extent, allows to judge, whether there is room for a potential partonic effect in the interpretation of a given experimental observation. However, when interpreting results from transport calculations one should be aware that these models might reach conditions (e.g. local energy densities) that cannot easily be reconciled with a purely hadronic scenario. But on the other hand, these type of models very easily allow to generate comparison data for different experimental situations, like centrality selection, center-of-mass energies, etc.

Examples of hadronic transport models used in heavy ion physics for studying strangeness production are Ultra-relativistic Quantum Molecular Dynamics (UrQMD) [46, 47], Relativistic Quantum Molecular Dynamics (RQMD) [48], Hadron-String Dynamics (HSD) [49]. Other models, such as A-Multi-Phase-Transport (AMPT) model [50] include both, hadronic and partonic, degrees of freedom. The EPOS model (Energy-conserving quantum mechanical multiple scattering approach, based on Partons, Off-shell remnants, and Splitting of parton ladders) [51], on the other hand, follows a phenomenological approach that is based on a initial parton model.

The UrQMD and the HSD model both implement binary elastic and inelastic hadronic scattering processes at lower center-of-mass energies and string excitation at higher  $\sqrt{s_{\text{coll}}}$ . They differ slightly in the number of hadronic states that are implemented. UrQMD 1.3, for instance, includes all baryonic resonances up to masses of 2 GeV and mesonic resonances up to 1.9 GeV, as documented by the Particle Data Group. Above these masses hadronic excitations are treated within a string model with meson formation times on the order of 1 - 2 fm/c. In the recent version 2.3 the hadron resonance spectrum has been extended toward a continuous distribution of resonance states for meson-baryon reactions between  $1.67 \text{ GeV} < \sqrt{s_{\text{coll}}} < 3 \text{ GeV}$  [52]. This version includes Pythia [53] to model initial hard collisions for high

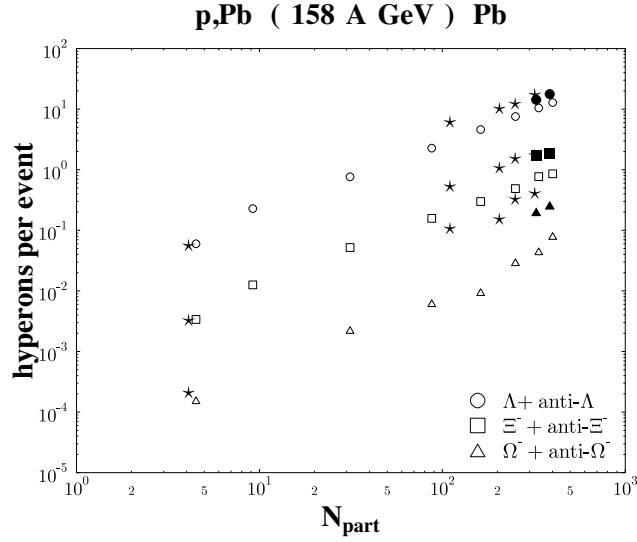


Figure 2: The sum of hyperons and anti-hyperons at midrapidity as a function of the number of participants for Pb+Pb and p+Pb collisions at 158A GeV. The experimental data by the WA97 collaboration [111] are represented by stars, while the open symbols correspond to default UrQMD calculations. The full symbols denote UrQMD results derived with reduced masses or, equivalently, enhanced string tension [60].

energy reactions ( $\sqrt{s_{\text{coll}}} > 10$  GeV). The HSD model on the other hand includes nucleons,  $\Delta$ ,  $N^*(1440)$  and  $N^*(1535)$  resonances, strange baryons and their resonances ( $\Lambda$ ,  $\Sigma$ ,  $\Sigma^*$ ,  $\Xi$ ,  $\Xi^*$ , and  $\Omega$ ), as well as their anti-particles, and the  $0^-$  and  $1^-$  octet meson states. Above  $\sqrt{s_{\text{coll}}} \approx 2.6$  GeV inelastic hadronic collisions are described by the FRITIOF model [54]. Both model approaches are adjusted to reproduce the known elementary nucleon-nucleon, meson-nucleon, and meson-meson cross sections over a wide kinematic range as well as possible. Beyond the simple superposition of independent nucleon-nucleon collisions, therefore additional effects are modeled as they are present in a nuclear environment. These include rescattering processes between the reaction products, which can lead to strangeness exchange reactions like  $\bar{K} + Y \leftrightarrow \pi + \Xi$  ( $Y = \Lambda, \Xi$ ), and thus enhance the production of  $\Xi$ .

Generally, transport models provide a reasonable description of the production rates of particles with only one strange quark (kaons and  $\Lambda$ ) [55, 56, 57], even though there are remaining discrepancies in various details. However, it has frequently been shown that the observed enhancement factors of multi-strange particles cannot easily be understood in the context of conventional hadronic transport models without invoking more exotic features as, e.g., color ropes [58, 59, 60, 61, 62]. This is illustrated in Fig. 2 which shows a comparison of measured hyperons yields at 158A GeV to UrQMD results obtained with standard parameters. While the data for p+Pb collisions are reasonably described by the model, substantial differences between measurement and model are visible for central nucleus-nucleus reactions. In case of the  $\Omega$  there is an order of magnitude between data and the transport model result. The rates of multi-strange baryons can be matched by the model by either lowering the masses of the constituent quarks or increasing the string tension ( $\kappa = 3$  GeV/fm, compared to the standard value of  $\kappa = 1$  GeV/fm) in an artificial manner (see filled symbols in Fig. 2) [60]. So far it has not been possible to describe the enhancement of multi-strange baryons in a conventional hadronic scenario. However, multi-meson fusion processes [34], which can contribute to the yield of strange anti-baryons in a dense hadronic medium and might thus reduce the discrepancy between hadronic models and the data (see discussion in the previous section), should also be taken into account in a transport approach. First steps into this direction have been done within the HSD model [49, 63], but a systematic and quantitative evaluation of this effect has not yet been performed, mainly due to the large amount of

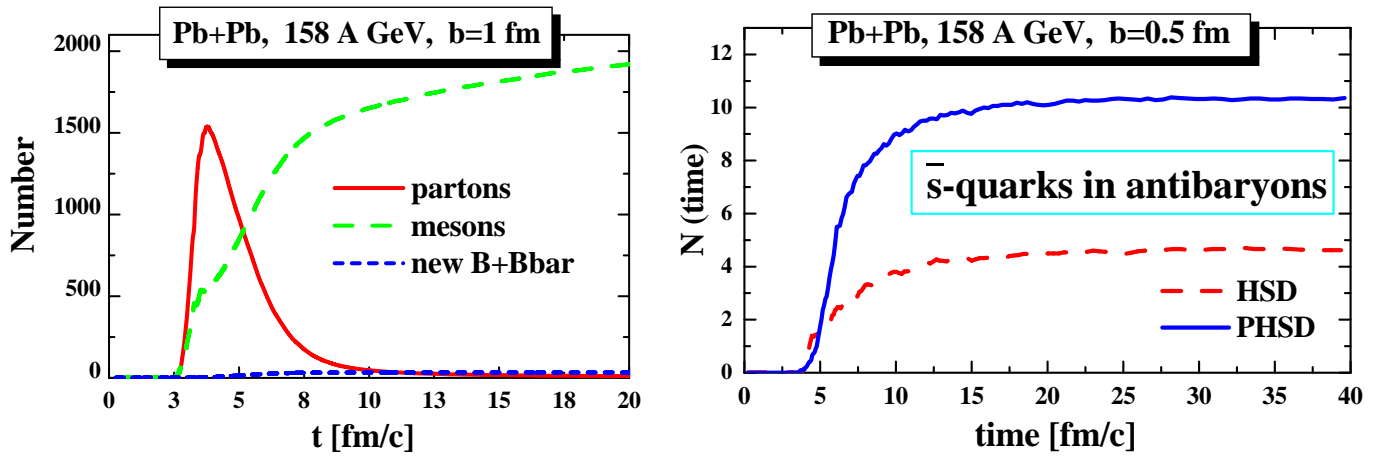


Figure 3: Left: The number of produced partons (solid red line), mesons (long dashed green line), and baryon-anti-baryon pairs (short dashed blue line) as a function of time for central Pb+Pb at 158A GeV (impact parameter  $b = 1$  fm), as calculated with the PHSD model [56, 64]. Right: The number of  $\bar{s}$  quarks contained in anti-baryons for central Pb+Pb collisions at 158A GeV from PHSD (solid blue line) and HSD (dashed red line) [56].

required computing resources.

An extension of the purely hadronic transport models is the Parton-Hadron-String Dynamics (PHSD) transport approach, which includes also interacting partons as dynamic quasiparticles matched to reproduce recent lattice QCD results [56, 64]. The transition from partonic to hadronic degrees of freedom is described by fusion of quark-antiquark pairs or three quarks (antiquarks), obeying color neutrality, flavor and energy-momentum conservation. An analysis of SPS data with this model shows that up to 40 % of the collision energy is stored in partonic degrees of freedom. The left panel of Fig. 3 illustrates how at top SPS energy ( $\sqrt{s_{\text{NN}}} = 17.3$  GeV) already around 1500 partons are created in the early phase of the collision. This partonic phase can have a significant effect on the transverse mass distributions of kaons, due to repulsive partonic mean fields and initial parton scatterings, as well as on the production rates of multi-strange anti-baryons. As shown in the right panel of Fig. 3 the number of anti-strange quarks contained in anti-baryons increases by roughly a factor two in comparison to the purely hadronic HSD model. This approach therefore allows to estimate to which extent the presence of a partonic phase is needed in order to describe (multi-)strange particle production in heavy ion collisions.



## 2.3 Statistical models

Statistical models represent another theoretical approach that plays an important role for the understanding of strangeness production in heavy ion collisions. Several implementations of this model are frequently applied in this context, e.g. Becattini et al. [65], Braun-Munzinger et al. [66], THERMUS [67], SHARE [68], and THERMINATOR [69]. The codes for latter three models are publicly available. Based on the assumption that particle yields at the end of all inelastic interactions are corresponding to the chemical equilibrium expectation, these type of models have generally been quite successful in describing measured multiplicities with a small set of parameters. The basic ingredient of these models are the partition functions, either grand-canonical, canonical, or micro-canonical. While the canonical or even micro-canonical ensembles have to be used to describe small systems (e.g. p+p) [44], the grand-canonical approximation provides a good description in the case of large systems such as central Au+Au or Pb+Pb collisions. In the grand-canonical formulation of the statistical model, the mean hadron multiplicities  $\langle N_i \rangle$  are defined as [70]:

$$\langle N_i \rangle = (2J_i + 1) \frac{V}{(2\pi)^3} \int d^3p \frac{1}{\gamma_s^{-s_i} \exp[(E_i - \mu \cdot \mathbf{q}_i)/T_{\text{ch}}] \pm 1} \quad (4)$$

The parameters are the chemical freeze-out temperature  $T_{\text{ch}}$ , the chemical potentials  $\mu$ , the volume  $V$ , the strange quark fugacity  $\gamma_s$ , the spin  $J_i$  and the number of strange quarks  $s_i$  of a given particle type  $i$ . To account for the different statistical behavior, the  $+$  sign in the denominator is valid for fermions, while the  $-$  sign is used for bosons. The strange quark fugacity  $\gamma_s$  allows for the possibility that strangeness might not be fully equilibrated ( $\gamma_s < 1$ ) and is used in some implementations of the statistical model [65, 71], while other versions assume a full equilibrium also for strange particles ( $\gamma_s = 1$ ) [66, 72]. Other implementations allow the non-strange quarks to be out of equilibrium as well and therefore introduce yet an additional factor  $\gamma_q$  [73, 74]. The chemical potentials  $\mu_S$  and  $\mu_Q$  are determined by the constraint of global strangeness and charge conservation, while the baryonic chemical potential  $\mu_B$  is a free fit parameter. Some implementations of the statistical model (e.g. [65]) directly calculate multiplicities according to Eq. (4) and therefore also have to adjust the volume  $V$ . If instead particle ratios are fitted, as it is done in [66], the volume parameter drops out and only  $T_{\text{ch}}$  and  $\mu_B$  remain as free parameter (for  $\gamma_s = 1$ ). Another aspect that has been frequently debated is whether the statistical model analysis should be restricted to midrapidity yields or if rather  $4\pi$  integrated multiplicities should be used [65, 75]. This issue plays mainly a role for SPS energies, at which it is difficult to separate the central fireball and the fragmentation regions, where the physics will be different. At RHIC energies these regions will be well separated and for most particle species anyway only midrapidity  $dN/dy$  values are experimentally available. The necessity of including  $\gamma_s$  in the fits as a free parameter seems to some extent arise from the choice of  $4\pi$  multiplicities as input. At least at SPS energies  $\gamma_s$  comes out closer to one if midrapidity values are used [75, 76].

Figure 4 shows two different fits with statistical models to heavy ion data, measured at  $\sqrt{s_{\text{NN}}} = 17.3$  GeV [76] and  $\sqrt{s_{\text{NN}}} = 200$  GeV [77]. These examples show that the yields of all strange particles, including the rare  $\Omega$  and  $\Xi^+$ , agree quite well with the chemical equilibrium expectation, both at the SPS and at RHIC. In models that include  $\gamma_s$  as a free parameter it is found that  $\gamma_s$  is usually larger than 0.6 - 0.7 [78], thus indicating that strange particle production seems to be at least not far away from the equilibrium value. One notable exception to this behavior is the  $\Lambda(1520)$  resonance, whose yield has been found to be below the prediction of the statistical model by almost five standard deviations (see left panel of Fig. 4). Due to its short lifetime ( $c\tau = 12.6$  fm) the resonance decays to a large part still inside the fireball. As a consequence its decay particles will be subject to elastic scattering processes in the medium which in turn reduce the yield of  $\Lambda(1520)$  that is reconstructible via an invariant mass analysis. In addition the regeneration cross section in the hadronic phase is smaller than the one for scattering processes of the decay particles, which results in overall suppression of the measurable resonances [79].

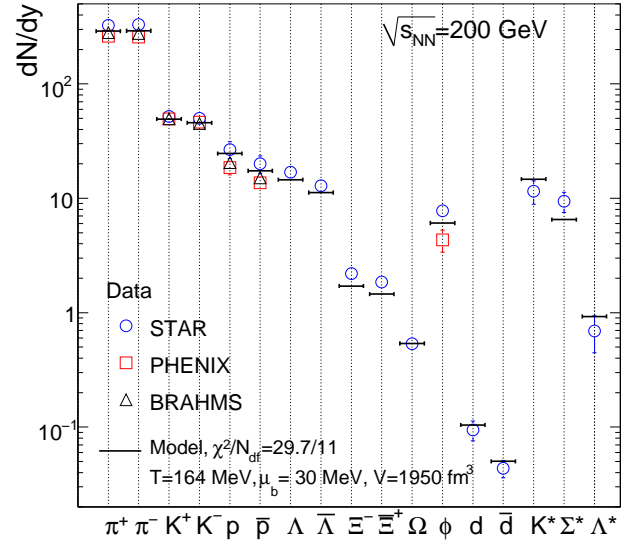
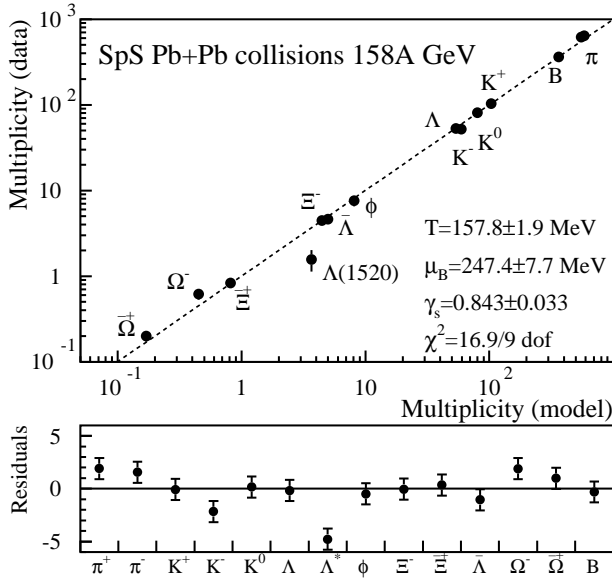


Figure 4: Left: The measured particle multiplicities versus the result of a statistical model fit for Pb+Pb collisions at  $\sqrt{s_{NN}} = 17.3$  GeV [76]. The lower panel shows the fit residuals. Right: Measured hadron yields around midrapidity for Au+Au collisions at  $\sqrt{s_{NN}} = 200$  GeV, together with a statistical model fit, resulting in the shown parameters [77].

This is the case for the  $\Lambda(1520)$  and the  $K(892)$  at SPS and RHIC energies [80]. Depending on the suppression a lower limit for the lifetime of the hadronic phase can be derived [81]. Due to this effect it is suggested to exclude the resonances from statistical model fits in order to determine freeze-out parameters.

It has been realized quite early that the resulting parameters  $T_{ch}$  and  $\mu_B$  lie on a single freeze-out curve, which follows a constant energy density over particle density of  $\langle E \rangle / \langle N \rangle \approx 1$  GeV [72] (see left panel of Fig. 5). This has been interpreted as a consequence of the changing composition of the hadron gas at chemical freeze-out, moving from a nucleon gas at low temperatures to a mainly meson dominated gas at high temperatures. As a result the average rest mass per particle  $\langle M \rangle$  of the hadron gas decreases with increasing temperature, thus compensating the increasing thermal contribution to the energy density such that, in a non-relativistic approximation,  $\langle E \rangle / \langle N \rangle \approx \langle M \rangle + 3/2 T_{ch} \approx 1$  GeV results [72]. Therefore, the two chemical freeze-out parameters  $T_{ch}$  and  $\mu_B$  do not vary independently of each other, when the center-of-mass energy of the reaction is changed. If furthermore the  $\sqrt{s_{NN}}$  dependence of  $\mu_B$  is parametrized, particle ratios at different energies can be predicted within the statistical model approach. In [82] the following phenomenological parametrization was suggested:

$$\mu_B(s_{NN}) \simeq \frac{a}{(1 + \sqrt{s_{NN}}/b)}; \quad a \simeq 1.27 \text{ GeV}; \quad b \simeq 4.3 \text{ GeV}. \quad (5)$$

The resulting  $\sqrt{s_{NN}}$  dependence of  $T_{ch}$  and  $\mu_B$  is shown in the right panel of Fig. 5. Based on this parametrization it was shown in [82] that a maximum of the relative strangeness production is to be expected around  $\sqrt{s_{NN}} = 7 - 8$  GeV (see Section 4.2 for a detailed discussion). Alternative suggestions to parametrize the chemical freeze-out curve have been made (e.g. by requiring a fixed total (anti-)baryon densities of  $n_B \approx 0.12 \text{ fm}^{-3}$  [83], or a fixed value of the entropy density,  $s/T^3$ , of approximately 7 [84, 85]). Other parameterizations of the energy dependence of the chemical freeze-out parameters

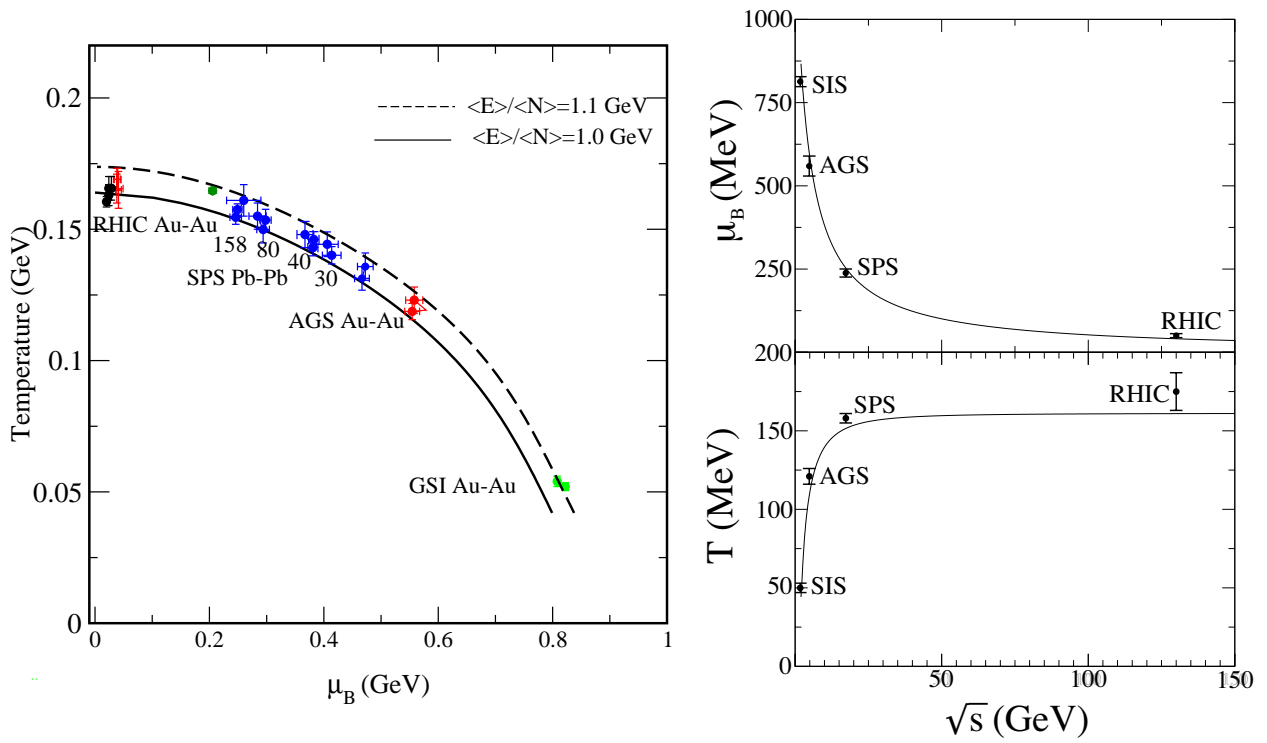


Figure 5: Left: The chemical freeze-out parameters  $T_{\text{ch}}$  and  $\mu_B$  for different energies, as obtained from fits to data from RHIC, SPS, AGS, and SIS. The lines correspond to the freeze-out conditions  $\langle E \rangle / \langle N \rangle = 1$  GeV and 1.1 GeV [88]. Right: The variation of  $T_{\text{ch}}$  and  $\mu_B$  as a function of energy. The lines are the parametrization according to Eq. (5), using the freeze-out condition  $\langle E \rangle / \langle N \rangle = 1$  GeV (Fig. is adapted from [82]).

can be found in [78]. Even though these parameterizations result in similar  $T_{\text{ch}} - \mu_B$  curves, they are motivated by different physical interpretations. For instance, fixed baryon density criterion is based on the picture that the freeze-out line is determined by a critical  $n_B$  below which inelastic baryon-baryon and baryon-meson interactions cease to change the chemical composition.

At low energies or for small systems, such as p+p, the description of particle yields with a statistical model has to be based on the canonical, or micro-canonical, ensemble [44, 86, 87]. In these ensembles strangeness production will be suppressed due to the small correlation volume in which strangeness conservation has to be fulfilled [89]. Therefore, it has been suggested to model the system size dependence of strangeness production by a transition from a canonical ensemble to a grand-canonical one [90].

### 3 Experimental overview

This section summarizes the history of the main experimental observations that have been made in order to establish strangeness enhancement in high energy heavy ion reactions. Also, we shortly review the experiments at the SPS and RHIC and the experimental techniques that have been employed to measure strange particles.

#### 3.1 Basic observations

The prediction outlined above triggered numerous experimental efforts in order to establish whether strangeness enhancement is realized in high energy heavy ion reactions. Early attempts at the AGS and SPS were limited to the measurement of particles with  $|S| = 1$  (i.e. kaons,  $\Lambda$ , and  $\bar{\Lambda}$ ), and to smaller reaction systems (Si+Au, O+Au, S+S, S+Au) [91, 92, 93, 94, 95, 96, 97, 98, 99]. But already with these data it was possible to establish that there is indeed an enhancement of strangeness production for kaons and  $\Lambda$  relative to pion production compared to p+p and p+A collisions [92, 98, 100]. However, since the yields of  $|S| = 1$  particles measured in A+A can as well be understood in terms of a hadron resonance gas, including rescattering processes [55, 101], this observation cannot unambiguously be interpreted as a signature for QGP formation. Therefore, dedicated experiments focused in the following on the measurement of multi-strange (anti-)baryons in S+A and p+A collisions [102, 103, 104, 105, 106, 107, 108, 109, 110]. One of the important results of the first heavy ion period at the SPS was that also  $\Xi^-$  and  $\bar{\Xi}^+$  production is enhanced in S+W collisions with respect to p+W interactions [108]. With the availability of Pb beams at the SPS these studies were extended in the years after 1994 toward a systematic study of the system size dependence of this effect, including the rare  $\Omega$  hyperon [111, 112, 113]. A review of the experimental results available after the first round of CERN experiments with Pb beams at 158A GeV can be found in [114].

Figure 6 shows the strange particle enhancement in Pb+Pb collisions relative to p+Be interactions as observed by the NA57 experiment [112]. The strangeness enhancement factor  $E_S$  is defined as:

$$E_S = \left( \frac{1}{\langle N_{\text{part}} \rangle} \frac{dN(\text{Pb+Pb})}{dy} \Big|_{y=0} \right) / \left( \frac{1}{2} \frac{dN(\text{p+p(Be)})}{dy} \Big|_{y=0} \right) \quad (6)$$

In order to account for the larger reaction volume of the nucleus-nucleus system, the measured yields are normalized by the averaged number of participating nucleons  $\langle N_{\text{part}} \rangle$ . This quantity is usually derived from a Glauber model calculation [115, 116]. A clear hierarchy of the enhancement factors for the different particle species is observed: While for the  $\Lambda$  ( $S = -1$ ) the enhancement reaches values of 3 – 4,  $E_S$  is found to be close to 10 for the  $\Xi^-$  ( $S = -2$ ) and 20 for the  $\Omega$  ( $S = -3$ ) in central Pb+Pb collisions. Such an enhancement pattern is expected in the case of a full chemical equilibrium for a large system [90], which, according to the early publications [7, 8, 9], might be interpreted as a sign for fast partonic equilibration in a QGP. It should be pointed out that equilibration in a partonic phase at high temperatures can lead to an over-saturation of strangeness production relative to the expectation of an equilibrated hadron gas at typical chemical freeze-out temperatures, if the transition happens very suddenly [117]. In any case it demonstrates that in high energy nucleus-nucleus collisions additional mechanisms for strange particle production are at work. The strong enhancement of multi-strange baryons is the most dramatic effect observed when comparing p+p to A+A collisions (other effects like  $J/\psi$  suppression or high- $p_t$  suppression are on the order of a factor 5, while the  $\Omega$  enhancement reaches values up to 15 – 20 for central reactions).

The NA57 results [112] are a refinement of the previous WA97 measurements [111] and thus supposed to supersede these data. While NA57 and WA97 use p+Be collisions as a baseline measurement, other experiments compare the A+A data to p+p collisions [113, 118, 119]. There are indications that

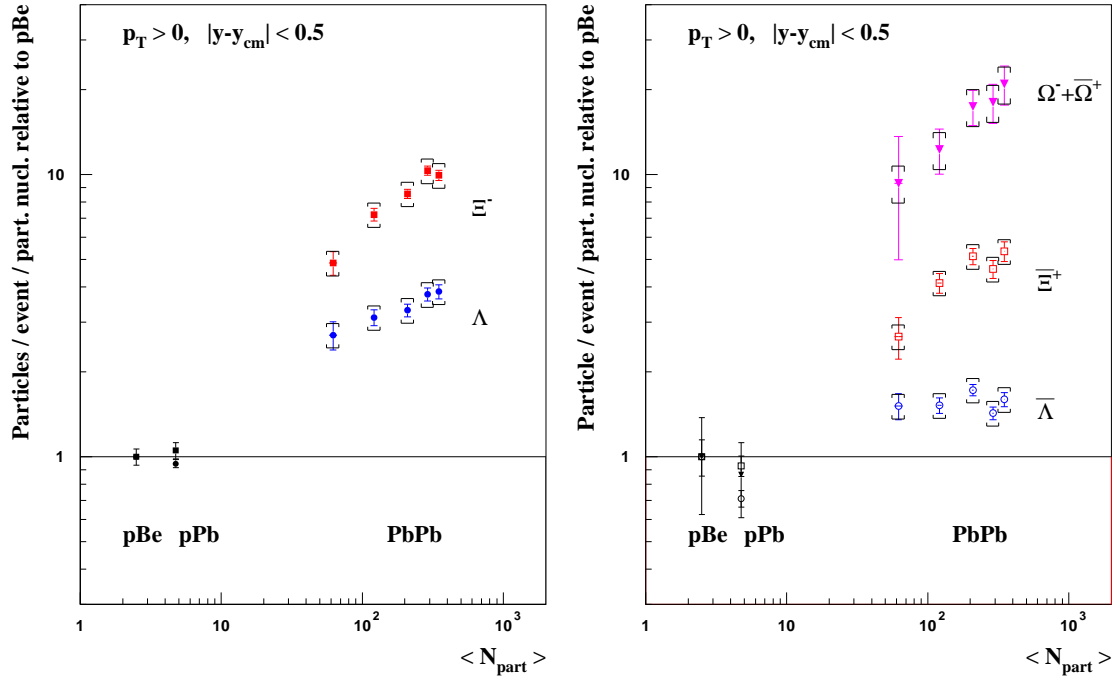


Figure 6: The enhancement of strange particle production with respect to p+Be collisions as a function of the number of participating nucleons, measured by the NA57 collaboration for Pb+Pb collisions at 158A GeV (Fig. adapted from [112]).

strangeness production is already enhanced in p+A collisions relative to p+p scaled by  $N_{\text{part}}$  [120, 121] and that a simple participant scaling is therefore violated. A projectile nucleon that collides more than once behaves different than one that is participating in a single binary collision (see also the discussion on the core corona model in Section 5.1). Even though this effect cannot be explained by a QGP formation, since the created fireball is too small, and it also not sufficient to explain the enhancement in A+A [120], it shows that an understanding of p+A reactions is an important prerequisite for the interpretation of heavy ion collisions. A consequence of this effect is that the measured enhancement in A+A will be less if p+A is used as a reference instead of p+p.

### 3.2 Experimental techniques

The strange particles listed in Table 1 have been measured by several experiments, both at the SPS and at RHIC. In Pb+Pb era at the SPS, these are the WA97, NA44, NA45, NA49, NA50, NA57, and NA60 experiments, while at RHIC data on strange particle production were gathered mainly by the STAR, PHENIX and BRAHMS collaborations (see Table 2). A detailed summary of the available data measured at different center-of-mass energies can be found in section 9.1.

The reconstruction of strange particles is done via two basic experimental methods, which are employed by the experiments listed above. On one side there is the direct reconstruction as a charged particle track ( $K^\pm$ ) and the indirect reconstruction via their weak decay topology ( $K_S^0$ , hyperons, and  $K^\pm$  via kinks). In the following, a short description of the basic methods is given and their strengths and associated difficulties (e.g. required corrections) are discussed.

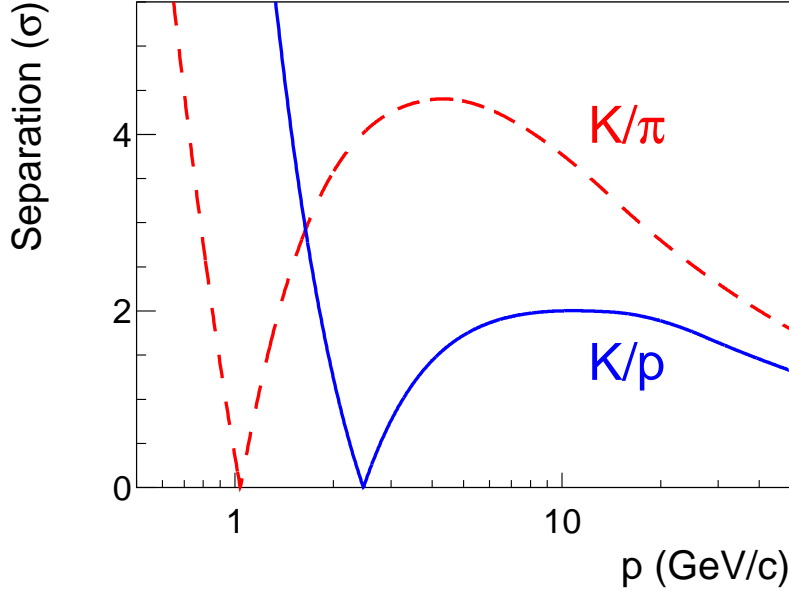


Figure 7: The separation of kaons to pions and protons as achievable by specific energy loss ( $dE/dx$ ) measurements for a resolution of 4% as obtained by the NA49 experiment [123].

### 3.2.1 Charged kaons

In the case of charged kaons, a direct identification of the particles can be performed. Their trajectory can be reconstructed and their identity derived from either their specific energy loss ( $dE/dx$ ) in the detector material, their time-of-flight (TOF), the kink decay topology, or their Čerenkov signal.

The main advantage of using the specific energy loss for particle identification is that it is usually measured with the same device that is used for tracking (e.g. time projection chambers (TPC) or silicon detectors) and that therefore the same acceptance can be covered. This allows to identify particles in large regions of phase space. The charged particles traveling through the active volume of the detectors lose energy by atomic collisions in the gas (TPC, drift chamber) or silicon (Si-detectors). The released charge depends only on the velocity of the particle, as described by the Bethe-Bloch formula

$$-\frac{dE}{dx} = Kz^2 \frac{Z}{A} \frac{1}{\beta^2} \left[ \frac{1}{2} \ln \left( \frac{2m_e c^2 \beta^2 \gamma^2 T_{\max}}{I^2} \right) - \beta^2 - \frac{\delta(\beta\gamma)}{2} \right], \quad (7)$$

and thus allows to separate different particle species experimentally, if their momentum is known.  $K$  is a constant,  $z$  the charge of the incident particle,  $m_e$  the electron mass,  $Z$  the atomic number and  $A$  the atomic weight of the detector medium,  $\beta$  the velocity of the incident particle in units of  $c$ ,  $T_{\max}$  the maximum kinetic energy which can be imparted to a free electron in a single collision,  $I$  the mean excitation energy of the detector medium in eV,  $\gamma = (1 - \beta^2)^{-1/2}$ , and  $\delta(\beta\gamma)$  the density effect correction [10]. At lower momenta ( $p < 3 - 4$  GeV for pions), where the specific energy loss follows the  $1/\beta^2$  dependence of the Bethe-Bloch curve, the kaons can be easily separated from protons and pions. Therefore the  $dE/dx$  method is very well suited for kaon identification in collider experiments up to momenta of  $p \leq 0.7$  GeV/c [122]. Above this momentum the kaon band crosses the pion band and a clear separation is difficult. In fixed target experiments at higher energies, where due to the additional Lorentz-boost particles have to be measured at higher laboratory momenta, the  $dE/dx$  method becomes more involved. Because in the high momentum region the specific energy loss is described by the relativistic rise region of the Bethe-Bloch curve, where the bands of pions, kaons, and

Table 2: Overview on experiments measuring strange particles at the SPS and at RHIC.

Experiment	Particles	Reaction systems	$\sqrt{s_{\text{NN}}}(\text{GeV})$	$4\pi$
NA44	$K^\pm$	Pb+Pb	17.3	—
NA57 (WA97)	$K_S^0, \Lambda, \Xi, \Omega$	p+A, Pb+Pb	8.7, 17.3	—
NA45	$\phi \rightarrow e^+ + e^-$	Pb+Pb	17.3	—
NA49	$K^\pm, \phi, \Lambda, \Xi, \Omega$	p+p, C+C, Si+Si, Pb+Pb	6.3, 7.6, 8.7, 12.3, 17.3	yes
NA50	$\phi \rightarrow \mu^+ + \mu^-$	Pb+Pb	17.3	—
NA60	$\phi \rightarrow \mu^+ + \mu^-$	In+In	17.3	—
STAR	$K^\pm, \phi, \Lambda, \Xi, \Omega$	p+p, d+Au, Cu+Cu, Au+Au	9.2, 62.4, 130, 200	—
PHENIX	$K^\pm, \phi, \Lambda$	Au+Au	130, 200	—
BRAHMS	$K^\pm$	p+p, Au+Au	62.4, 200	yes

protons are relatively close together. But also in these cases the  $dE/dx$  signal has been successfully employed for kaon identification. For instance the NA49 experiment was specifically designed to reach a  $dE/dx$  resolution of 4% [123] (the resolution for STAR is better than 8% [124]), which is sufficient to de-convolute the measured  $dE/dx$  spectra and to extract charged kaon yields on a statistical basis [125, 126]. Figure 7 shows the separation power that can be achieved with this resolution.

The time-of-flight method, in many cases combined with a  $dE/dx$  measurement, can provide a clean identification of charged kaons in the momentum range  $p \leq 2.0 \text{ GeV}/c$  [125, 126, 127, 128, 129]. To apply this method, the path length and the momentum of a given particle has to be known, as well as the precise time-of-flight. The required time resolution typically has to be below 100 ps, which can easily be achieved with scintillator based TOF detectors in combination with a fast start detector. Since the TOF method requires a separate detector, the acceptance region of the TOF measurement is in most cases, due to cost reasons, smaller than the one available for tracking. Modern techniques, such as resistive plate chambers (RPC), allow to build TOF detectors with a large acceptance. These detectors can cover, e.g., the full  $2\pi$  azimuth of the TPC in the STAR and ALICE experiments.

Sometimes an alternative way of reconstructing charged kaons is followed, which exploits the topology of a weak decay, namely  $K^\pm \rightarrow \mu^\pm + \nu_\mu(\bar{\nu}_\mu)$  or  $K^\pm \rightarrow \pi^\pm + \pi^0$ . Since the neutral particles are not detected, the reconstruction algorithms try to identify this decay by looking for kinks in the tracks of charged particles. This method is complementary to  $dE/dx$  or TOF measurement and can provide an independent way of particle identification with different systematic effects [130]. However, there are substantial sources of background, like charged hyperon and pion decays, as well as multiple scattering in the detector material [114]. The method is limited to particles that decay inside the sensitive area of the tracking devices which reduces the available statistics.

### 3.2.2 Hyperons and $K_S^0$

The other method, which is used for the majority of strange particles, is based on the analysis of their decay topology. This method requires the simultaneous reconstruction of 2 ( $K_S^0, \Lambda, \bar{\Lambda}$ ) or 3 ( $\Xi^-, \Xi^+, \Omega^-, \bar{\Omega}^+$ ) charged tracks. Figure 8 illustrates the topologies of a  $\Lambda$ , respectively  $\Omega^-$ , decay. In order to search for  $V^0$  candidates (i.e.  $K_S^0, \Lambda$ , and  $\bar{\Lambda}$ ), all oppositely charged tracks are combined into pairs and the distance of closest approach (DCA) between them is searched for. The position of the DCA gives the possible secondary vertex position. Since weak decays are characterized by long lifetimes of the mother particles, a large fraction of their decay vertices has a substantial spatial distance to the

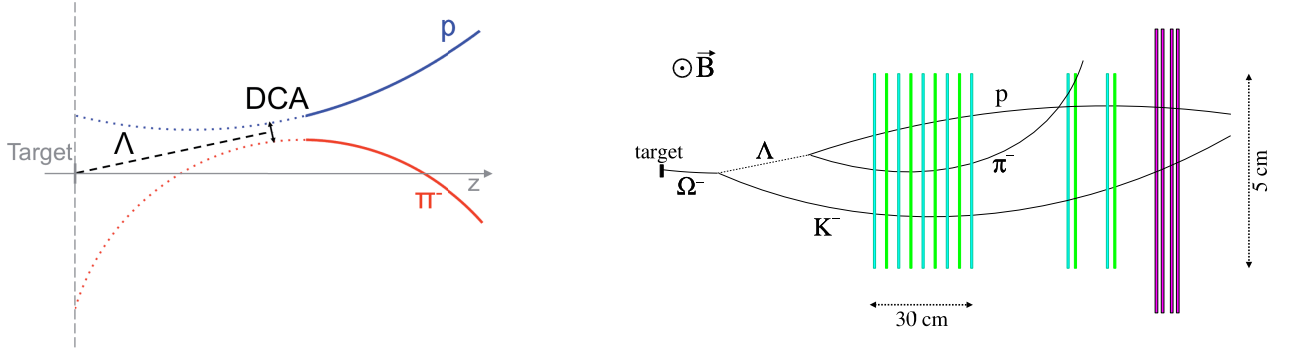


Figure 8: Left: The topology of the decay  $\Lambda \rightarrow p + \pi^-$ . The solid lines correspond to the reconstructed particle tracks of the proton and the negative pion, while the dotted ones represent their extrapolations through the magnetic fields toward the target plane. Shown is the distance of closest approach (DCA) between the two charged tracks. Right: Illustration of the reconstruction of the decay  $\Omega^- \rightarrow \Lambda + K^-$  within the NA57 setup (not to scale) [112].

interaction vertex. Therefore, the requirement of a minimal distance between both allows to reduce the combinatorial background, which to a large extent results from combining primary tracks. As the corresponding decay lengths are on the order of centimeters (see Table 1), the secondary vertex resolution has to be in the same order or better for collider experiments. The requirements are less stringent in the case of fixed target experiments, since the average decay lengths are larger due to the additional Lorentz boost. In many cases (e.g. E895 [131], NA49 [58], STAR [132, 133], and PHENIX [134]) TPCs or drift chambers provide sufficient spatial resolution for this purpose. Other experiments (e.g. NA57 [112]) use silicon detectors as a tracking device, which provide much better vertex resolution in the sub-millimeter region and a higher rate capability at the expense of a reduced acceptance. In large collider experiments both techniques, TPC and silicon, are combined (e.g. ALICE [135] and STAR). By applying additional topological cuts (e.g. on the pointing angle of the mother momentum vector relative to the main vertex position) or using additional particle identification on the daughter tracks, the combinatorial background can be further reduced. For the particle pair assigned to a given  $V^0$  candidate the invariant mass is calculated based on a mass hypothesis by assigning either the pion mass to both tracks ( $K_S^0$ ) or the pion and the proton mass ( $\Lambda$ ) to the positively and negatively charged track, respectively. From the resulting invariant mass distributions the yields of the corresponding mothers particles can be extracted. Typically a mass resolution around 4 MeV is achieved.

$\Lambda$  and  $K_S^0$  can also be reconstructed without measuring the decay vertex position, as has been demonstrated by PHENIX [134] and NA45 [136]. The drawbacks of this approach are an increased combinatorial background and a poorer mass resolution, while the benefit is a somewhat reduced sensitivity to the accuracy of the detector simulation.

$\Lambda$  ( $\bar{\Lambda}$ ) candidates from this first step can then be combined with a third charged track to form  $\Xi^-$  ( $\bar{\Xi}^+$ ) and  $\Omega^-$  ( $\bar{\Omega}^+$ ) candidates. Since the  $\Lambda$  are in these cases daughter particles, it is usually required that their momentum vector does not point back to the interaction vertex, in contrast to the case of the



primary  $\Lambda$ . This method has been successfully applied to heavy ion reactions to measure systematically the production of the rare  $\Omega^-$  and  $\bar{\Omega}^+$  [59, 112, 133], although usually the sum  $\Omega^- + \bar{\Omega}^+$  is shown in order to increase the statistical significance.

### 3.2.3 Corrections

The different detection techniques for strange particles differ in their necessary corrections. The ones for the direct measurement of charged kaons are mainly determined by the single track acceptance and reconstruction efficiency, which is usually quite high (typically  $> 90\%$  at higher momenta), thus resulting in relatively small correction factors. In contrast, the reconstruction of the decay topology requires the measurement of two charged tracks. Therefore any acceptance losses and inefficiencies enter quadratically. Additionally, the algorithms for the secondary vertex reconstruction usually cause losses which have to be corrected, mainly due to the cuts applied to reduce the combinatoric background. As a consequence, the corrections for this method are higher than for the single track measurements and have to be carefully determined by a Monte Carlo simulation (e.g. for  $\Lambda$  the efficiencies vary typically between  $5\%$  and  $50\%$ , depending on momentum). On the other side, the particle identification of the topological method is clean and unambiguous.

Another correction that is necessary for some particles is the correction for feed-down from weak decays. This is important for  $\Lambda$  and  $\bar{\Lambda}$ , where part of the measured yield is originating from the decays  $\Xi^-(\bar{\Xi}^+) \rightarrow \Lambda(\bar{\Lambda}) + \pi^-(\pi^+)$ <sup>1</sup>. Due to the long decay lengths of the weak decays, the fraction of accepted feed-down particles strongly depends on the detector geometry, the reconstruction algorithm, and the applied cuts (typical values for the size of the feed-down correction are  $5\%$  to  $20\%$  for  $\Lambda$ , for  $\bar{\Lambda}$  it can be even higher). Therefore, this correction has to be applied at the analysis stage and cannot be calculated properly afterward without exact knowledge of the experimental conditions. This argument does not apply to strong and electro-magnetic decays, which all happen close to the reaction zone. There, all decay particles will be included in the measured yields and can thus easily be subtracted, if necessary. For instance, the measured  $\Lambda$  multiplicities usually refer to the sum  $\Lambda + \Sigma^0$ , since  $\Lambda$  from the decay  $\Sigma^0 \rightarrow \Lambda + \gamma$  cannot be separated experimentally from the primary ones without performing an additional photon measurement.

---

<sup>1</sup>The weak decays  $\Omega^-(\bar{\Omega}^+) \rightarrow \Lambda(\bar{\Lambda}) + K^-(K^+)$  are usually ignored, since their contribution is marginal.

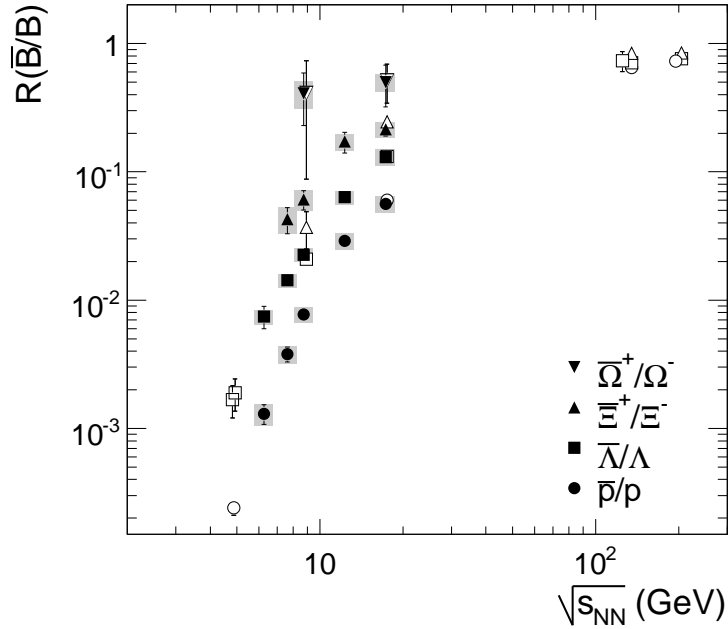


Figure 9: The  $\bar{p}/p$ ,  $\bar{\Lambda}/\Lambda$ ,  $\bar{\Xi}^+/\Xi^-$ , and  $\bar{\Omega}^+/\Omega^-$  ratios around midrapidity in central Pb+Pb and Au+Au collisions as a function of  $\sqrt{s_{NN}}$ . Shown are data by the SPS experiments NA49 [58, 59, 137], NA44 [138] and NA57 [112, 139], from AGS [140, 141, 142, 143] and RHIC experiments [128, 132, 133, 134, 144, 145, 146].

## 4 Energy dependence

The large amount of data at different center-of-mass energies that have been accumulated at the SPS and at RHIC over the recent years allows, together with AGS measurements from low energies, to compile a relatively complete picture of the energy dependence for most strangeness related observables. Of special interest is the  $\sqrt{s_{NN}}$  evolution of the observed strangeness enhancement. Also, several intriguing structures in the energy dependences have emerged, for instance in the  $K^+/\pi^+$  ratio. The  $\phi$  meson, which might be directly sensitive to the partonic phase of the collision, deserves a special attention and is treated in a separate subsection. We also discuss the  $\sqrt{s_{NN}}$  dependence of transverse and longitudinal spectra.

### 4.1 Strangeness enhancement at different energies

In order to answer the question whether the observed strangeness enhancement can really be caused by a fast equilibration in a partonic phase, the investigation of its energy dependence provides important information. Following this argument one should observe an onset of strangeness enhancement when going from low center-of-mass energies toward higher ones. At lower energies, where the energy densities should be too low to form a deconfined state, any enhancement relative to elementary collisions can only be due to secondary hadronic interactions, which are, at least in the case of multi-strange baryons, unlikely to drive the system toward chemical equilibrium. It has been pointed out quite early that the enhancement for kaons is, in contrast to naive expectations, rising toward lower energies [151, 152]. A similar observation has been made for  $\Lambda$  [58], while for multi-strange particles the current experimental situation still is unclear. Data on multi-strange particles for heavy ion collisions at lower energies are scarce and have large errors, while p+p reference data are essentially not existent. While first attempts

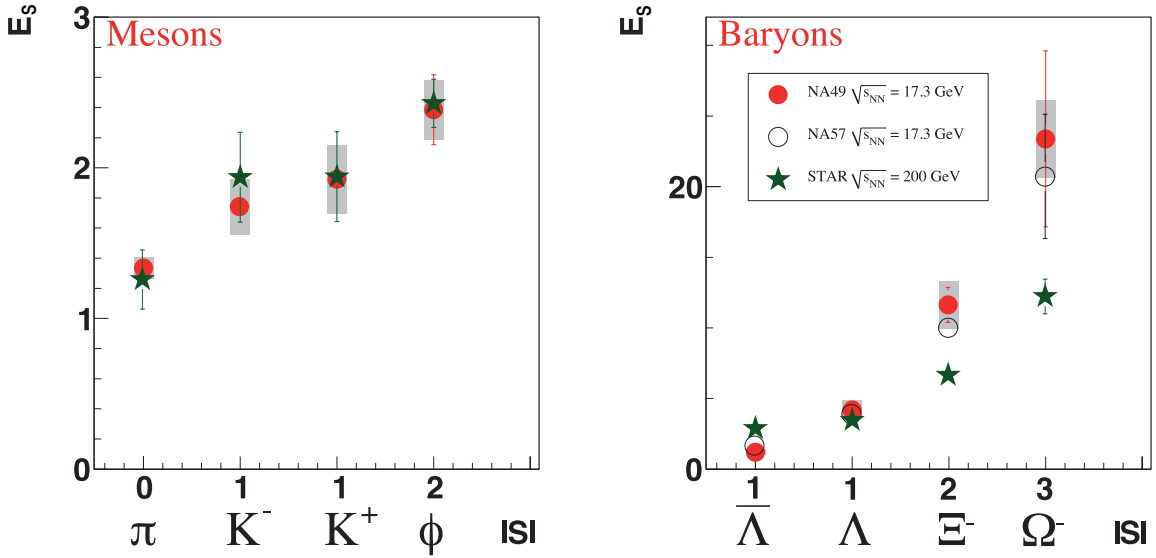


Figure 10: The enhancement factor  $E_S$  for midrapidity yields measured in central Pb+Pb (Au+Au) collisions at  $\sqrt{s_{NN}} = 17.3$  GeV (200 GeV) versus the number of strange valence quarks for mesons (left) and baryons (right) [118]. Shown are data by the NA49 collaboration (filled circles) [58, 59, 125, 147, 148, 149], by the NA57 collaboration (open circles) [112], and by the STAR collaboration (filled stars) [119, 122, 150]. NA49 and STAR use p+p collisions as baseline, while in the case of NA57  $E_S$  is calculated relative to p+Be collisions.

into this direction have been done for heavy ion collisions [131, 153], there is still a lack of reference data from p+p or p+A collisions at the same energies. Threshold effects play an important role at very low energies and complicate any interpretation. Nevertheless, it is interesting to observe that  $\Xi^-$  measurements at very low energies are close (Au+Au at 6A GeV, E895 collaboration [131]), or even above (Ar+KCl at 1.76A GeV, HADES collaboration [153]), the expectation for an equilibrated hadron gas [82, 154].

At higher energies, a clear trend in the energy dependence of strangeness enhancement emerges. The comparison of the hyperon enhancement factors measured at top SPS energy ( $\sqrt{s_{NN}} = 17.3$  GeV) and top RHIC energy ( $\sqrt{s_{NN}} = 200$  GeV) shows that the enhancement for baryons is actually higher at SPS. As shown in the right panel of Fig. 10, the enhancement factor  $E_S$  (Eq. (6)) is larger for  $\Xi^-$  and  $\Omega^-$  at  $\sqrt{s_{NN}} = 17.3$  GeV than at  $\sqrt{s_{NN}} = 200$  GeV. However, for  $\Lambda$  and mesons ( $K^+$ ,  $K^-$ ,  $\phi$ ) the enhancement is essentially the same at both energies (left panel of Fig. 10). Preliminary data by the NA57 collaboration indicate that in central Pb+Pb collisions at  $\sqrt{s_{NN}} = 8.7$  GeV the  $\Xi^-$  enhancement is again larger as compared to p+Be collisions than at  $\sqrt{s_{NN}} = 17.3$  GeV [155]. The main reason for this behavior is that the strangeness production in p+p (p+Be) collisions is rising faster with energy than in nucleus-nucleus reactions. For instance, the  $\bar{\Xi}^+/\pi^+$  ratio changes by a factor of  $\sim 3.8$  in p+p and of only  $\sim 2.9$  in central A+A between  $\sqrt{s_{NN}} = 17.3$  GeV and 200 GeV [58, 120, 122, 133, 147, 156]. This is even more pronounced for the  $\Xi^-/\pi^-$  ratio, since for central nucleus-nucleus collisions this ratio is decreasing between the two energies by roughly 20% (see Fig. 14), while at the same time it is rising in p+p collisions by 25%. In the context of statistical models the suppression of strangeness production is understood as a consequence of the small available volume, requiring a canonical ensemble, which results in a strong reduction of the available phase space for strange particles. Along with the center-of-mass energy the overall multiplicity in p+p reaction increases, and thus the effective volume, with the result of a less effective phase space suppression. Proton-proton collisions therefore slowly approach the chemical equilibrium values for large systems (which then can be described by a grand-canonical

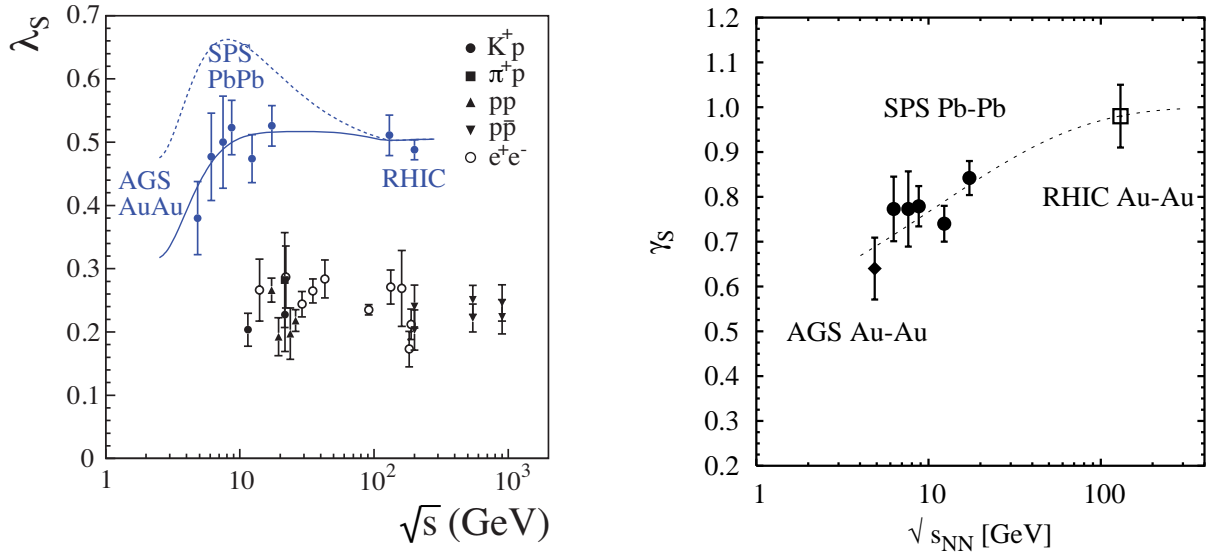


Figure 11: Left: The energy dependence of the Wroblewski factor  $\lambda_s$  as determined via fits of a statistical hadron gas model to multiplicities measured in elementary ( $e^+e^-$ ,  $K^+p$ ,  $\pi^+p$ ,  $pp$ ,  $p\bar{p}$ ) as well as central heavy ion collisions [157]. The dashed line is a prediction for a fully equilibrated hadron gas, the solid line an interpolation of fits including an additional strangeness suppression factor  $\gamma_s$  (Fig. is adapted from [157]). Right: The energy dependence of the strangeness undersaturation factor  $\gamma_s$  at chemical freeze-out [78]. The dashed line is a phenomenological parametrization in the form  $\gamma_s = 1 - 0.606 \exp \left\{ -0.0209 \sqrt{A \sqrt{s_{NN}}} \right\}$ , where  $A$  is the atomic mass number, fulfilling  $\gamma_s \rightarrow 1$  for  $\sqrt{s_{NN}} \rightarrow \infty$  [78].

ensemble), such as heavy ion collisions.

The  $\bar{\Lambda}$  deviates from the general trend, because its enhancement significantly increases with center-of-mass energy. But in this case the strong change of the net-baryon density in A+A collisions with energy and the consequently strongly changing anti-baryon/baryon ratio is dominating the energy evolution of the  $\bar{\Lambda}$  enhancement. The sensitivity of a given anti-baryon to this effect depends on its strangeness content. As a consequence a clear hierarchy of the anti-baryon/baryon ratio  $R$  is visible,  $R(\bar{\Omega}^+/\Omega^-) > R(\bar{\Xi}^+/\Xi^-) > R(\bar{\Lambda}/\Lambda) > R(\bar{p}/p)$ , and the energy dependence of the ratios gets significantly weaker with increasing strangeness content (see right panel of Fig. 9).

Another way of looking at the energy dependence of strangeness enhancement is studying the Wroblewski factor  $\lambda_s$  [65]. It is defined as the ratio of the mean multiplicities of the newly produced valence quark-antiquark pairs [158]:

$$\lambda_s = \frac{2 \langle s\bar{s} \rangle}{\langle u\bar{u} \rangle + \langle d\bar{d} \rangle} \quad (8)$$

Since usually not all hadron multiplicities for a given reaction system are measured, the determination of  $\lambda_s$  has to rely on some input from models. In Fig. 11  $\lambda_s$  has been extracted from fits with a statistical hadron gas model for elementary collisions, as well as for central heavy ion reactions [157]. The  $\lambda_s$  values determined for nucleus-nucleus collisions are found to be a factor 2 higher than for elementary collisions, even at the lowest SPS energy ( $\sqrt{s_{NN}} = 6.3$  GeV). There is an indication for a rise of  $\lambda_s$  at lower energies ( $\sqrt{s_{NN}} < 6$  GeV), but from then on  $\lambda_s$  stays at a constant value of  $\approx 0.5$ , well above the value of  $\approx 0.25$  found for elementary collisions. This demonstrates again that strangeness production is globally enhanced in heavy ion reactions, already at very low energies. However, it remains to be seen whether this is not only true for the global strangeness production, but as well for the rare multi-strange

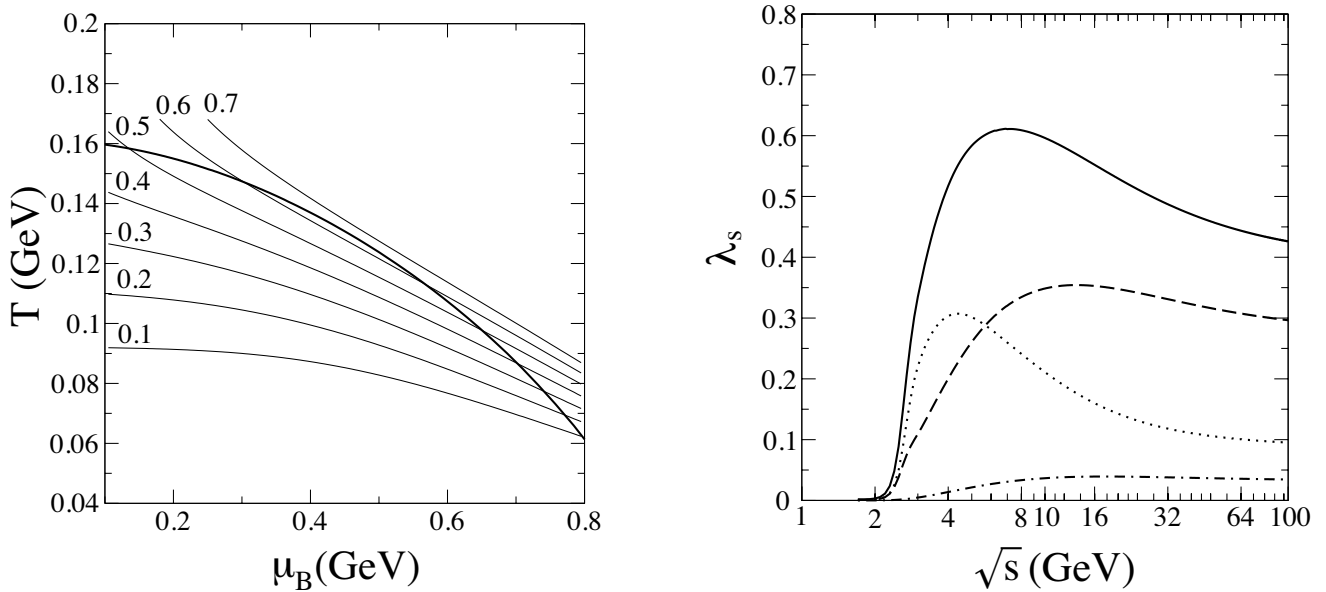


Figure 12: Left: Lines of constant Wroblewski factor  $\lambda_s$  in the  $T_{\text{ch}} - \mu_B$  plane. The thick solid line without labeling represents the chemical freeze-out curve defined by  $\langle E \rangle / \langle N \rangle \simeq 1$  GeV [82]. Right: The contributions to the Wroblewski factor from strange baryons (dotted line), strange mesons (dashed line), and with hidden strangeness (dash-dotted line) in the full equilibrium case (i.e.  $\gamma_s = 1$ ) [82]. The sum of all contributions is given by the solid line. (Figs. are adapted from [82].)

baryons.

In the statistical model approach by Becattini et al. [78] the strangeness undersaturation factor  $\gamma_s$  is a free parameter in the fits to the particle yields. The right panel of Fig. 11 shows the energy dependence of  $\gamma_s$  for nucleus-nucleus collisions between AGS and RHIC energies. A slow increase with  $\sqrt{s_{\text{NN}}}$  from 0.7 - 0.8 at SPS toward a value of  $\gamma_s = 1$  at RHIC is observed. This would indicate that strangeness production is not yet fully equilibrated at the SPS, even though it is already very close to the full equilibrium case.

Under the full equilibrium condition (i.e.  $\gamma_s = 1$ ) the statistical model results in a well defined connection between a given chemical freeze-out position in the  $T_{\text{ch}} - \mu_B$  plane and the Wroblewski factor. The left panel of Fig. 12 shows the lines of constant  $\lambda_s$  in the  $T_{\text{ch}} - \mu_B$  plane [82]. Based on the parametrization of the  $\sqrt{s_{\text{NN}}}$  dependence of  $\mu_B$ , as e.g. given in Eq. (5), and the  $\langle E \rangle / \langle N \rangle \approx 1$  GeV freeze-out criterion (solid line in the left panel of Fig. 11), which connects  $T_{\text{ch}}$  to a given  $\mu_B$ , a unique curve for the energy dependence of  $\lambda_s$  can thus be constructed [82]. This curve is shown as solid line in the right panel of Fig. 12 and is characterized by a distinct maximum of relative strangeness production around  $\sqrt{s_{\text{NN}}}$  of 6 - 8 GeV (corresponding to  $\mu_B \approx 500$  MeV and  $T_{\text{ch}} \approx 130$  MeV). The dotted line in the

left panel of Fig. 11 is based on a similar approach, but uses different parameterizations of the energy dependence of the chemical freeze-out parameters [157]. It follows from these considerations that the relative contributions to  $\lambda_S$  change with energy. While at lower energies, where  $\mu_B$  is large, the produced strange quarks are to a large extent contained in strange baryons (dotted line), the relative strangeness production at higher energies ( $\sqrt{s_{NN}} > 6$  GeV, corresponding to  $\mu_B < 500$  MeV) is dominated by strange mesons (dashed line). The maximum in  $\lambda_S$  at lower energies is thus mainly due to the contribution of the strange baryons. Also strange mesons contribution exhibits a maximum, which is, however, less pronounced and shifted toward higher energies. This expected maximum of relative total strangeness production is reflected in the energy dependence of various strange to non-strange particle ratios, as discussed in the following sections.

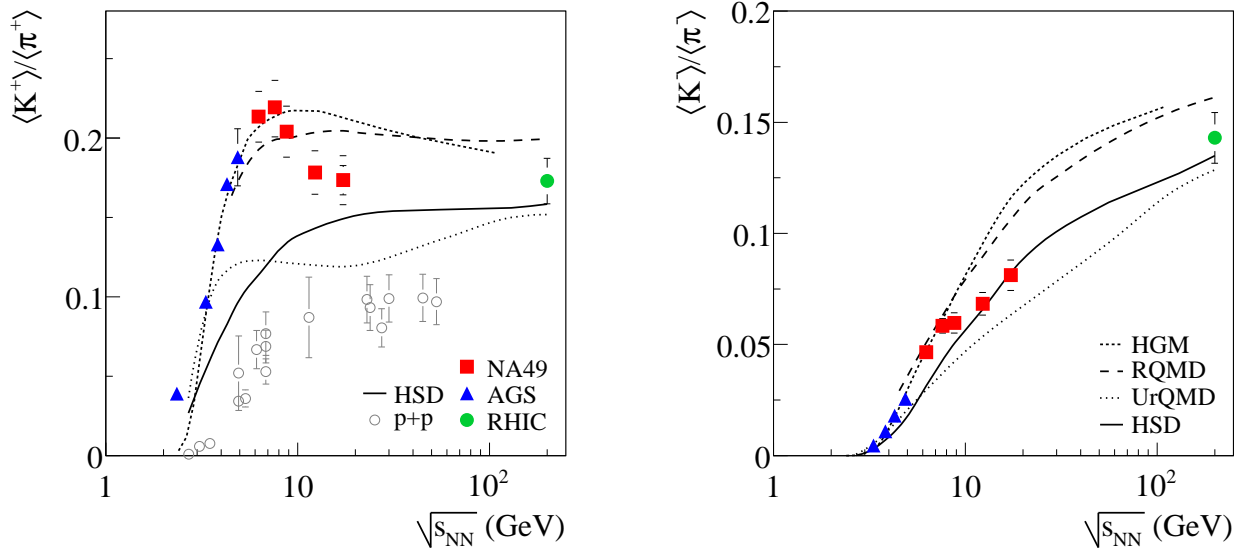


Figure 13: The energy dependence of the  $\langle K^+ \rangle / \langle \pi^+ \rangle$  ratio (left panel) and the  $\langle K^- \rangle / \langle \pi^- \rangle$  ratio (right panel) measured in central Pb+Pb and Au+Au collisions (solid symbols) [125, 126, 159, 160, 161, 162, 163, 164, 165, 166] compared to results from p+p( $\bar{p}$ ) reactions (open symbols) [151, 167] and from the transport models HSD (solid line) [49, 63], UrQMD (dotted line) [46], and RQMD (long dashed line) [48] and from a statistical hadron gas model (short dashed line) [72, 82].

## 4.2 Structures in the energy dependence of particle yields

Apart from the search for an onset of strangeness enhancement, the measurement of strange particle abundances in heavy ion collisions at different center-of-mass energies revealed new insights into the physics of strangeness production. Data from several experiments at the AGS, SPS, and RHIC allow to compile a comprehensive overview for central A+A collisions. In the following, only some of the most interesting features seen in the energy dependences shall be discussed. A compilation of the  $\sqrt{s_{NN}}$  dependences of the midrapidity yields of all strange particles is given in section 9.1 (see Figs. 40 and 41 and Tables 3–11).

### 4.2.1 The $K/\pi$ ratios

One of the most prominent observations in this context is a pronounced maximum in the energy dependence of the  $K^+/\pi^+$  ratio around  $\sqrt{s_{NN}} = 7$  GeV [126], as shown in the left panel of Fig. 13. The  $K^-/\pi^-$  ratio, in contrast, exhibits a rather smooth energy dependence with only a slight indication for a kink at the position of the maximum in the  $K^+/\pi^+$  ratio (right panel of Fig. 13). Transport models like RQMD [48], UrQMD [46], and HSD [49, 63, 168] are generally not able to describe the structures seen in the data. For instance, they just predict localized turnover in the energy dependence of the  $K^+/\pi^+$  ratio, but not the observed maximum. Similar discrepancies are present for the  $K^-/\pi^-$  ratio, although they are not so visible in this case, due to the less pronounced structure in its energy dependence.

On the other hand, a structure like the observed one has been predicted in [169] for the energy dependence of the strangeness to entropy ratio as a consequence of the onset of deconfinement. This prediction is based on the statistical model of the early stage [170], which is an extension of Fermi's statistical model of particle production that takes into account two different states of matter, a confined

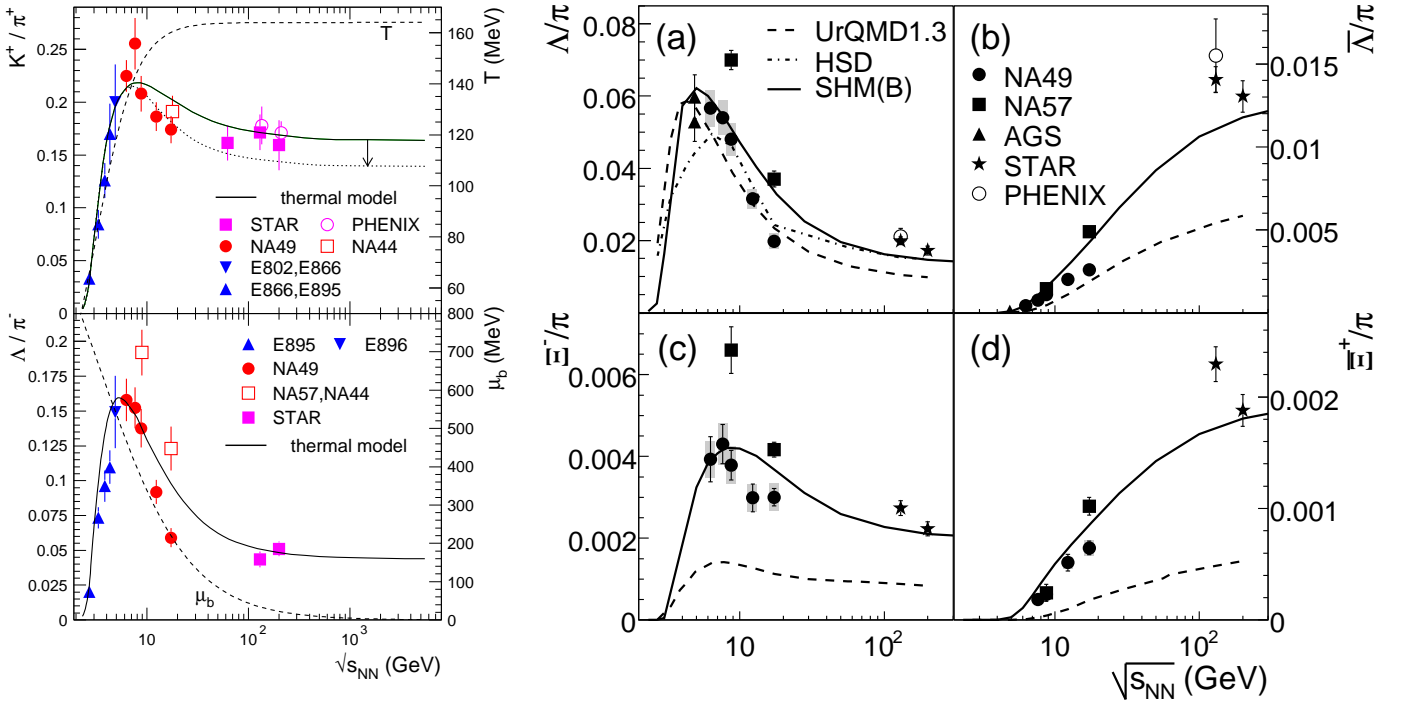


Figure 14: Left: The energy dependence of the rapidity densities  $dN/dy$  around midrapidity of  $K^+$  and  $\Lambda$ , divided by the ones of  $\pi^+$ , respectively  $\pi^-$ , for central Pb+Pb and Au+Au collisions. The solid line is the result of a statistical model calculation. The dotted line gives the  $K^+/\pi^+$  ratio including the additional effect of higher mass resonances. The dashed lines show the energy dependence of the temperature  $T_{ch}$  (upper panel) and of the baryonic chemical potential  $\mu_b$  (lower panel) [77]. Right: The energy dependence of the rapidity densities  $dN/dy$  around midrapidity of  $\Lambda$ ,  $\bar{\Lambda}$ ,  $\Xi^-$ , and  $\Xi^+$  divided by the total pion rapidity densities ( $\pi = 1.5 (\pi^- + \pi^+)$ ) for central Pb+Pb and Au+Au collisions [58, 112, 130, 132, 133, 134, 139, 141, 142, 143, 145, 146, 159, 171]. Please note that the vertical error bars correspond to the statistical errors only. Also shown are results for the transport models UrQMD (dashed line) [46] and HSD (dash-dotted line) [49, 63], as well as a statistical hadron gas model (solid line) [75].

(hadron gas) and a deconfined (QGP) state. The initial state is described by Fermi-Landau conditions, which allows to define the energy density at a given center-of-mass energy. At a critical temperature  $T_C$  a first order phase transition is assumed. This temperature corresponds via the energy density to a certain center-of-mass energy and is adjusted such that the transition occurs around  $\sqrt{s_{NN}} \approx 7 - 8$  GeV. The model assumes full statistical equilibrium in the initial stage of the reaction. Strangeness and entropy are conserved throughout the evolution of the system. Once the transition energy is passed, a change in the energy dependence of the strangeness to entropy ratio is expected due to the change of mass of the strangeness carriers and of the available number of degrees of freedom. At low energies strangeness is confined in hadrons with high mass, leading to a steep energy dependence of the strangeness to entropy ratio. At high energies, above  $T_C$ , the mass of the strangeness carriers is assumed to be reduced to the mass of the strange quarks, resulting in an almost flat energy dependence of this ratio. The charged pion multiplicity is assumed to be proportional to the entropy production. Since the  $K^+$  are carrying almost half of the produced anti-strange quarks<sup>2</sup> and are thus directly sensitive to the total (anti-)strangeness production, the  $K^+/\pi^+$  ratio should exhibit the same behavior as the total strangeness to entropy ratio.

<sup>2</sup>The other half is mainly contained in  $K^0$ , due to isospin symmetry, while strange anti-baryons do not contribute significantly at lower energies.



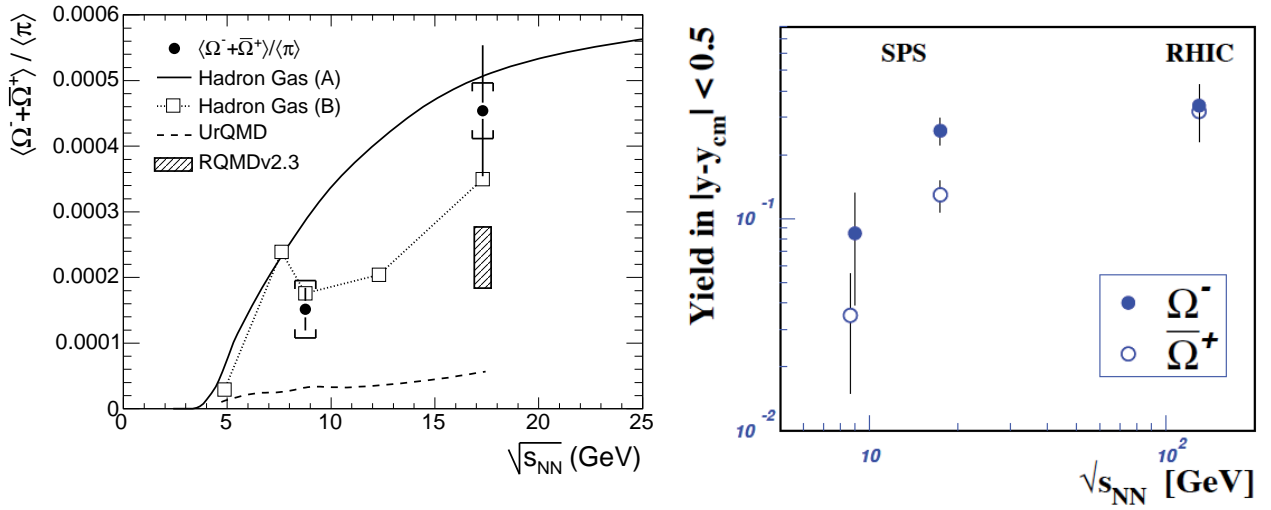


Figure 15: Left: The energy dependence of the  $\langle \Omega^- + \bar{\Omega}^+ \rangle / \langle \pi \rangle$  ratio in central Pb+Pb collisions [59]. Also shown are results for the transport models UrQMD (dashed line) [46] and RQMD (hashed box) [172], as well as of statistical hadron gas models, one with strangeness undersaturation factor  $\gamma_s$  (dotted line with empty boxes) [76] and one without (solid line) [82]. Right: the energy dependence of the  $\Omega^-$  and  $\bar{\Omega}^+$  rapidity densities  $dN/dy$  around midrapidity for central Pb+Pb [139] and Au+Au [132] collisions.

Even though this interpretation is highly debated and relies on simplified assumptions (e.g. ideal gas equations), the structure in the  $K^+/\pi^+$  ratio might nevertheless be indicative for a sudden change in the nature of the reaction system produced in this energy region.

The statistical hadron gas approach, using a parametrized  $\sqrt{s_{NN}}$  dependence of the chemical freeze-out temperature  $T_{ch}$  and the baryonic chemical potential  $\mu_B$  (see Eq. (5)), as based on fits to the measured particle ratios [72, 82], also results in a maximum of the  $K^+/\pi^+$  ratio at approximately the right position, although its width is clearly wider than the data (see short dashed curve in left panel of Fig. 13). However, a recent extension of this model that includes the scalar  $\sigma$  meson and high mass resonances ( $m > 2$  GeV) [77], following the early ideas of Hagedorn [40, 41], leads to an improved description of the data (left panel of Fig. 14). In [77] it has therefore been argued that the special form of the energy dependence of the  $K^+/\pi^+$  ratio would be a consequence of reaching the limiting temperature predicted by Hagedorn [173] and therefore indirectly indicate the presence of a quark-gluon plasma phase.

#### 4.2.2 Other particle ratios

Similar maxima as in the case of the  $K^+/\pi^+$  ratio, although not as sharp, can be observed in the ratios of strange baryons to pions (panel (a) and (c) of Fig. 14) [58]. While the  $\Lambda/\pi$  ratio is relatively well described by transport models, the  $\Xi^-/\pi$  ratio is clearly under-predicted by the HSD model [49, 63]. Generally, hadronic transport models are not able to match the measured abundances of multi-strange (anti-)baryons (see Fig. 14(d) and left panel of Fig. 15). The primary production mechanism of string fragmentation does not favor the generation of particles with multiple strangeness without going to unrealistic parameter settings (see discussion in Section 2.2) and subsequent rescattering processes add only little to the final multiplicities. Multi-meson fusion processes might help to approach the data, but the currently available transport codes do not yet include this feature.

Statistical hadron gas models generally provide a relatively good description of multi-strange par-

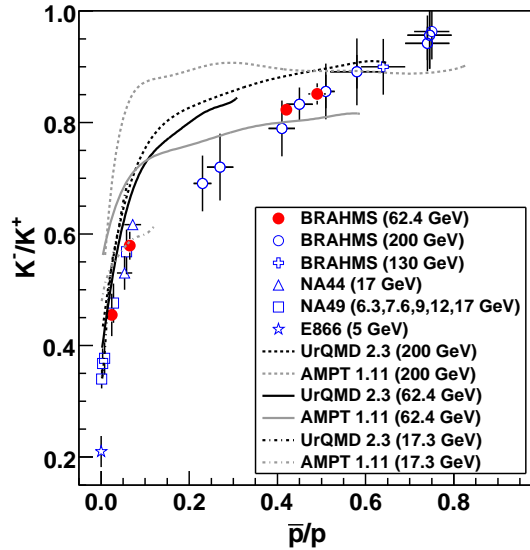


Figure 16: The  $K^-/K^+$  ratio as a function of the  $\bar{p}/p$  ratio [174]. The data are taken from several experiments [125, 126, 137, 140, 166, 174, 175] and are measured for central collisions at different  $\sqrt{s_{NN}}$  and rapidities. Also shown are various model predictions [46, 47, 50, 176].

ticles<sup>3</sup> [76, 75], including the  $\Omega$  (left panel of Fig. 15). So far, all measurements of strange particle multiplicities in heavy ion reactions are in reasonable agreement with the expectation for an equilibrated hadron gas at all energies, although in some implementations of this model, which use  $4\pi$  integrated multiplicities as input, the additional strangeness undersaturation parameter  $\gamma_s$  is needed to provide a proper fit to the data everywhere [76] (see discussion in Section 2.3). There is no indication yet for any significant departure from the chemical equilibrium values at lower energies [131, 153].

In the statistical model approach the maxima of the  $\Lambda/\pi$ ,  $\Xi^-/\pi$ , and  $K^+/\pi$  ratios are due to the specific dependence of the baryonic chemical potential  $\mu_B$  on the center-of-mass energy. This results in a maximum of relative strangeness production around  $\sqrt{s_{NN}} = 7$  GeV [82]. The right panel of Fig. 12 shows how, according to this model, the Wroblewski factor  $\lambda_s$  changes with energy. Especially the contribution from strange baryons exhibits a distinct maximum around  $\sqrt{s_{NN}} = 4$  GeV, which in the data is most clearly visible in the  $\Lambda/\pi$  ratio (Fig. 14(a)). The position of the maximum is expected to shift toward higher energies with increasing strangeness content of the baryon, and the maximum should be less pronounced for the  $\Xi^-$  and the  $\Omega^-$  [177]. The observed peak in the  $\Xi^-/\pi$  ratio seems to be smaller in the NA49 measurement [58], while the NA57 data suggest a stronger energy dependence [139] (see Fig. 14(c)). For the  $\Omega$  there is no evidence for a maximum, but the current data are limited in significance and coverage (see Fig. 15).

Figure 16 shows the  $K^-/K^+$  ratio as a function of the  $\bar{p}/p$  ratio [174]. The data points measured at RHIC energies by the BRAHMS collaboration ( $\sqrt{s_{NN}} = 62.4, 130$ , and  $200$  GeV) have been measured at different rapidities, while the SPS and AGS data correspond to midrapidity. Generally, a universal dependence of the  $K^-/K^+$  on the  $\bar{p}/p$  ratio is observed. Also included are predictions from two different transport models (UrQMD [46, 47] and AMPT [50, 176]). Even though they roughly follow the trend, they do not result in the universality observed in the data. In the statistical model approach, on the

<sup>3</sup>Please note that concerning the hyperon multiplicities there are still remaining discrepancies between the experiments NA49 and NA57 at the SPS (Figs. 14 and 41), which exceed the quoted systematic errors. These are present for all particles at  $158A$  GeV and for  $\Lambda$  and  $\Xi^-$  at  $40A$  GeV. Possible reasons might be difficulties in correcting trigger inefficiencies (NA57) or an insufficient correction of the multiplicity dependent reconstruction efficiency (NA49). But despite extensive discussion between the collaborations the origin of these discrepancies were never finally resolved.

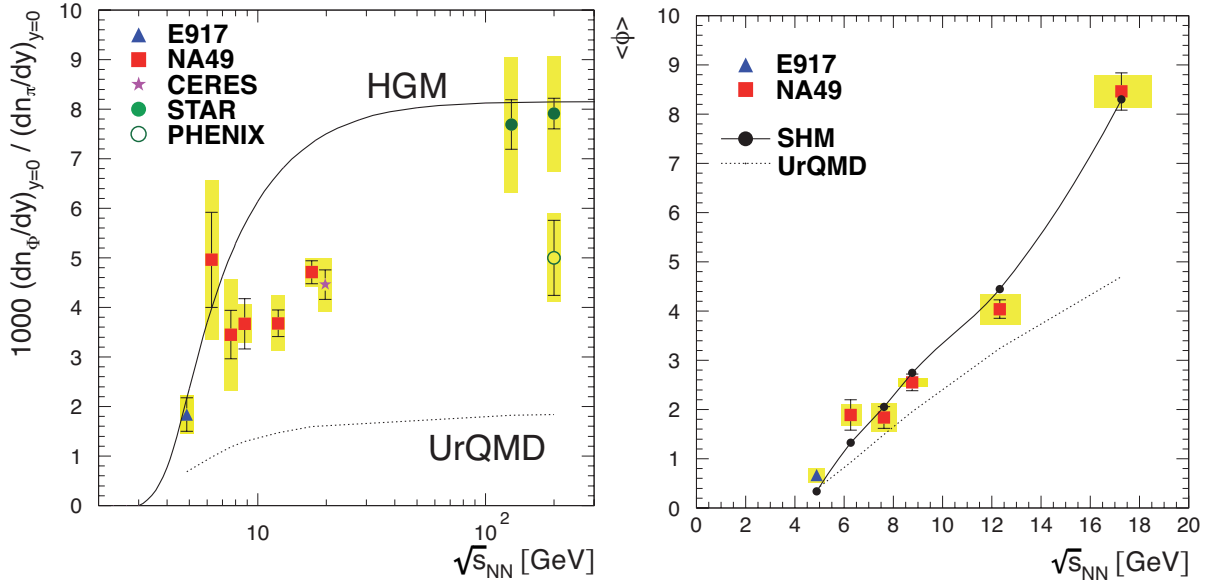


Figure 17: Left: The  $\phi/\pi$  ratio at midrapidity in central nucleus-nucleus collisions as a function of the center-of-mass energy [149]. Also shown are the predictions of a statistical hadron gas model [75] and of the transport model UrQMD1.3 [46]. Right: The total  $\phi$  multiplicity in central nucleus-nucleus collisions as a function of the center-of-mass energy [149]. The filled circles, connected by a solid line, represent results from a fit with a statistical hadron gas model that includes a strangeness undersaturation factor  $\gamma_s$  [78]. The dotted curve shows the prediction of the UrQMD model [46]. (The Figs. are adapted from [149].)

other side, the  $\bar{p}/p$  ratio is defined by the baryo-chemical potential  $\mu_B$  and the chemical freeze-out temperature  $T_{ch}$  as [178]

$$\frac{\bar{p}}{p} = \exp\left(\frac{-2\mu_B}{T_{ch}}\right). \quad (9)$$

Thus, the  $\bar{p}/p$  ratio, measured in the given rapidity range, should provide a good estimate of the local  $\mu_B$ . Under the assumption that the freeze-out temperature  $T_{ch}$  is constant, the  $\bar{p}/p$  ratio would therefore fully determine the chemical composition of the system. A fireball observed at high rapidities and high energies (e.g.  $\sqrt{s_{NN}} = 200$  GeV) would be equivalent to one at midrapidity and lower energies (e.g.  $\sqrt{s_{NN}} = 17.3$  GeV), and the measured particle ratios should be the same, as shown for the  $K^-/K^+$  ratio in Fig. 16. A detailed analysis [179] shows that both parameters,  $\mu_B$  and  $T_{ch}$ , depend on rapidity, but can be related via the freeze-out condition  $\langle E \rangle / \langle N \rangle \approx 1$  GeV [72]. However, the dependence of  $\mu_B$  on rapidity is found to be stronger at SPS energies than at RHIC.

#### 4.2.3 The $\phi$ Meson

Among the strange particles, the  $\phi$  meson has been of special interest. Due to its  $s\bar{s}$  valence quark structure it is strangeness neutral and should therefore not be sensitive to any hadro-chemical effects, as they are described in statistical hadron gas models by a strangeness undersaturation factor  $\gamma_s$  or the canonical suppression for small systems. However, if the  $\phi$  production was dominated by quark coalescence from a partonic phase of the reaction, its sensitivity would be even more pronounced. In this case, any strangeness undersaturation should affect the  $\phi$  rather as  $\gamma_s^2$ . On the other side, in a hadronic phase  $\phi$  mesons can be produced by kaon coalescence,  $K^+ + K^- \rightarrow \phi$ .

The energy dependence of the  $\phi/\pi$  ratio, measured around midrapidity in central nucleus-nucleus

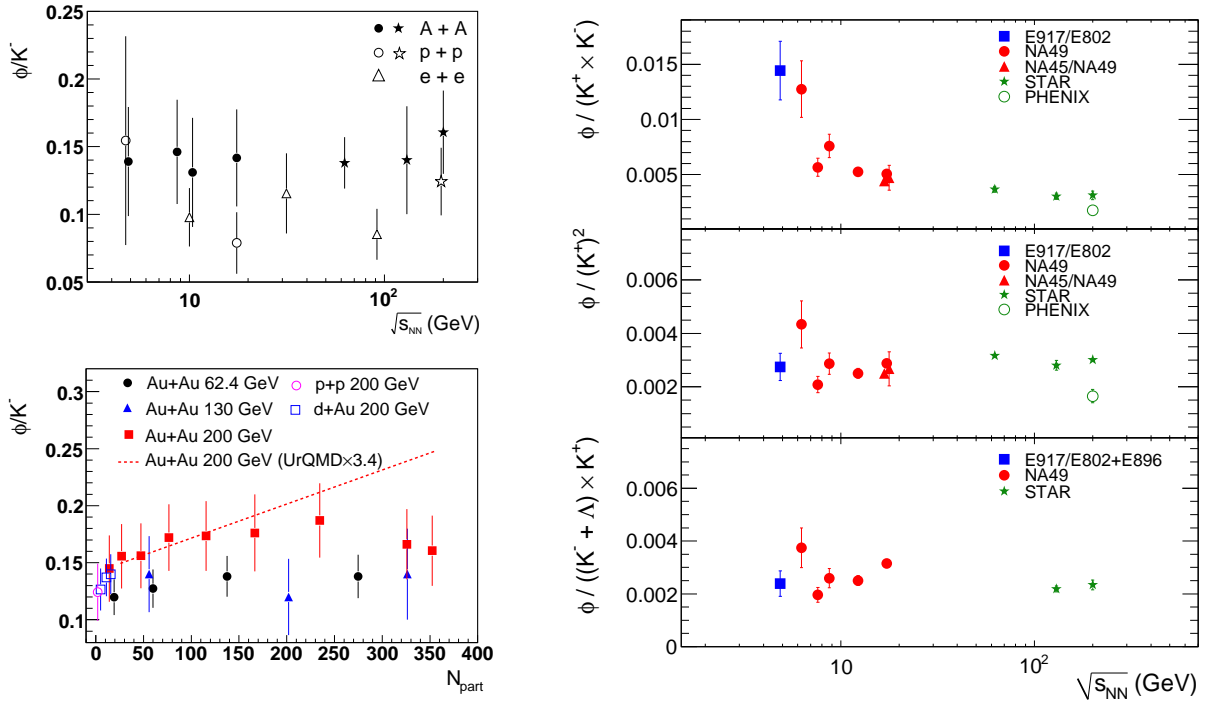


Figure 18: Upper left: The energy dependence of the  $\phi/K^-$  ratio in nucleus-nucleus (full symbols),  $e^+e^-$  (open triangles), and p+p (open circles and star) collisions [180]. Lower left: The system size dependence of the  $\phi/K^-$  ratio in different collisions systems. The dashed line shows scaled results for the transport model UrQMD [46]. Right: The energy dependence of the  $\phi$  yield, normalized by the product of the  $K^+$  and  $K^-$  yield (top), the square of the  $K^+$  yield (middle), and the product of the  $K^+$  yield with the sum of the  $K^-$  and  $\Lambda$  yields (bottom). All yields are measured around midrapidity for central Pb+Pb or Au+Au collisions. Shown are only statistical errors. The data are taken from [58, 122, 125, 126, 128, 133, 141, 145, 149, 160, 180, 181, 182, 183, 184, 185].

collisions, is summarized in the left panel of Fig. 17 [149]. This ratio increases monotonically with center-of-mass energy without any significant structure. The data are compared to a statistical hadron gas model, assuming full strangeness equilibration (i.e.  $\gamma_s = 1$ ) [75]. While this model matches the STAR measurement at high energies<sup>4</sup>, it does not provide a good description at the intermediate energies. On the other hand, if  $\gamma_s$  is included in the fits as a free parameter, the  $\phi$  yields can be described rather well (see right panel of Fig. 17). This sensitivity of the strangeness neutral  $\phi$  meson to the  $\gamma_s$  parameter suggests that the abundances of strange quarks are already determined in the partonic and not in the subsequent hadronic phase.

In a hadronic scenario the  $\phi$  can be produced via kaon coalescence. For instance in the hadronic transport model UrQMD [46] this is the dominant production mechanism. The predictions of this model are compared to the data as well (see Fig. 17). At AGS energies the model under-predicts the  $\phi/\pi$  ratio at midrapidity by a factor of 2 (left panel) and is further below the measurements at SPS and RHIC energies. For the unnormalized total yields the discrepancy is smaller (right panel), but still prominent at higher energies. This leads to the conclusion that kaon coalescence is not sufficient to explain the amount of observed  $\phi$ . There are two other observations that substantiate this point of view: the first is that the  $\phi/K^-$  ratio does not increase with system size, as predicted by UrQMD (see

<sup>4</sup>Please note that there is an unresolved discrepancy between the STAR and PHENIX measurement. The latter is lower by 40% than STAR. The difference is essentially in the low  $p_t$  region, while at higher transverse momenta the measurements are roughly in agreement.

lower left panel of Fig. 18), but is essentially flat. The second experimental indication is based on the comparison of the measured widths of the  $\phi$  rapidity distributions  $\sigma_\phi$  to the widths expected in the case of kaon coalescence (see discussion in Section 4.3.2).

It is a remarkable observation that the  $\phi/K^-$  ratio seems to be independent not only of the system size, but also of the center-of-mass energy of the reaction systems (see left panel of Fig. 18) [180]. Alternatively, one finds that the midrapidity  $\phi$  yields scale as well with the  $K^+$  yield squared (middle right panel of Fig. 18). Since the number of  $K^+$  is directly proportional to the number of produced anti-strange quarks (= number of strange quarks), the  $\phi$  production thus might only depend on the product of  $s$  and  $\bar{s}$  quarks. Since the  $s$  quarks are to a large extent contained in the  $K^-$  and  $\Lambda$ , the product  $s \cdot \bar{s}$  should be roughly proportional to  $K^+ \cdot (K^- + \Lambda)$ . The ratio  $\phi/(K^+ \times (K^- + \Lambda))$  is similarly energy independent than  $\phi/(K^+)^2$  (lower right panel of Fig. 18) and has approximately the same value ( $0.2 - 0.3 \cdot 10^{-3}$ ). On the other hand, the ratio  $\phi/(K^+K^-)$ , as it might be suggested by a naive kaon coalescence scenario, is clearly not energy independent (upper right panel of Fig. 18).

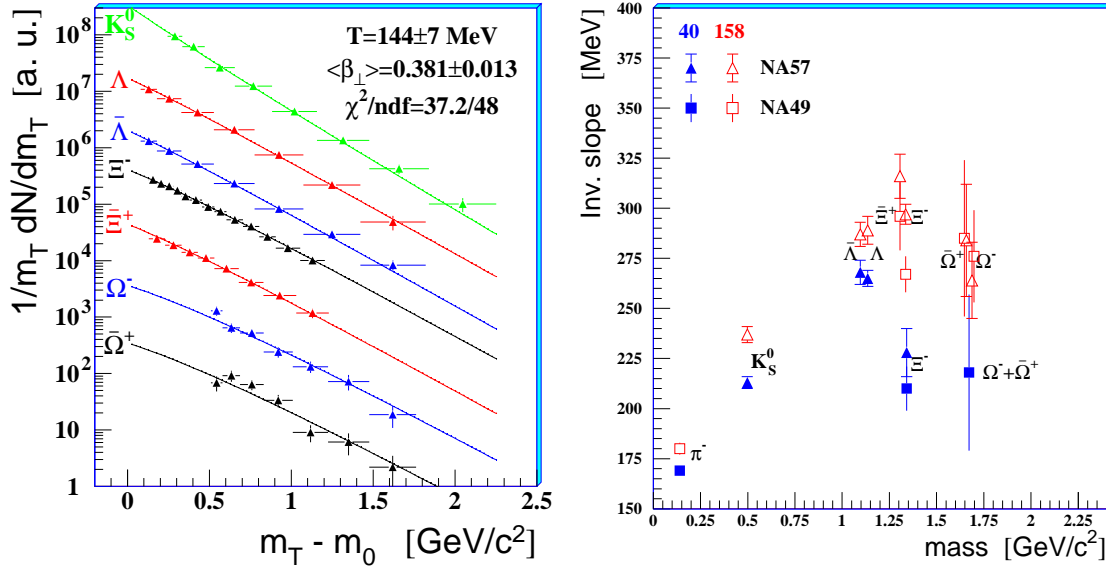


Figure 19: Left: The  $m_t$  spectra of  $K_S^0$ ,  $\Lambda$ ,  $\bar{\Lambda}$ ,  $\Xi^-$ ,  $\bar{\Xi}^+$ ,  $\Omega^-$ , and  $\bar{\Omega}^+$  as measured by NA57 for central Pb+Pb collisions at 158A GeV (Fig. adapted from [186]). This solid lines represent the result of a fit with a hydrodynamically inspired model [187]. Right: The inverse slope parameters as a function of the particle mass measured in central Pb+Pb collisions at 40A GeV (closed symbols) and at 158A GeV (open symbols). The data are from the NA57 [188] and the NA49 [59, 189, 190] collaboration.

### 4.3 Spectra

This section discusses the dependence of transverse mass spectra ( $m_t = \sqrt{p_t^2 + m^2}$ ) on the center-of-mass energy of the reaction, which gives insight into the evolution of radial flow. This is of interest especially for multi-strange baryons, since they could reveal the onset of a partonic contribution. The inverse slope parameters extracted from  $m_t$  spectra of charged kaons exhibit a step-like feature in their energy dependence, which might be connected to a first order phase transition. Further the measured rapidity spectra at different center-of-mass energies and attempts to connect thermal parameters determined at different rapidities and at different energies are discussed.

#### 4.3.1 Transverse momentum spectra

Transverse mass spectra have been measured for all strange particle species at different center-of-mass energies. As an example, the left panel of Fig. 19 shows the  $m_t$  spectra of  $K_S^0$  and hyperons, measured by the NA57 collaboration in Pb+Pb collisions at 158A GeV. Since strange particles span a relatively wide range of rest masses (between  $m(K^\pm) = 493.677 \text{ MeV}/c^2$  and  $m(\Omega) = 1672.45 \text{ MeV}/c^2$ ), they provide an ideal probe for the effects of transverse expansion, which is generated by the high energy density in the fireball. Especially the question to which extent the radial flow is caused by the partonic stage of the reactions can be addressed with multi-strange particles. In order to quantify the spectral shape, the invariant  $m_t$  spectra are usually fitted by an exponential function

$$\frac{dN}{m_t dm_t dy} \propto \exp\left(-\frac{m_t}{T^*}\right). \quad (10)$$

with  $T^*$  as the inverse slope parameter. For kaons the exponential results in a very good fit over a larger region of  $m_t$ . Heavier particles exhibit deviation from an exponential behavior, due to the stronger

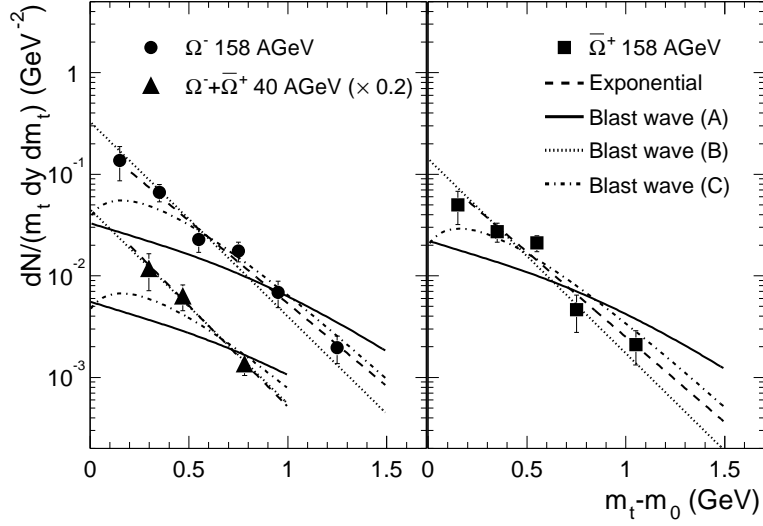


Figure 20: The transverse mass spectra of  $\Omega^-$  and  $\bar{\Omega}^+$  in central Pb+Pb collisions at 158A GeV and of the sum  $\Omega^- + \bar{\Omega}^+$  at 40A GeV [59]. The dashed curve shows a fit with an exponential. The solid, dotted, and dash-dotted curves represent a model including transverse expansion [187]. The used parameters are  $T_{fo} = 90$  MeV and  $\langle\beta_{\perp}\rangle = 0.5$  (A),  $T_{fo} = 170$  MeV and  $\langle\beta_{\perp}\rangle = 0.2$  (B), and  $T_{fo} = 127$  MeV and  $\langle\beta_{\perp}\rangle = 0.5$  (C). In (A) and (B) a linear velocity profile is used, while (C) was calculated with a constant expansion velocity.

influence of radial flow which introduces a convex shape in the spectra. Therefore, the fit result will depend on the  $m_t$  range in which the fit is performed. Nevertheless, a comparison of the inverse slope parameter  $T^*$  extracted for different particles at different energies, reveals already interesting features. In the right panel of Fig. 19 such a comparison for 40A and 158A GeV beam energy is shown [188]. The inverse slope parameters increase linearly with particle mass up to the  $\Lambda$ . This can be understood as a consequence of the radial expansion of the fireball, which, in a simplified picture, introduces an additional component to the effective inverse slope parameter  $T^*$ , that depends on the particle mass  $m$  and the expansion velocity  $v_{\perp}$  as

$$T^* \approx T_{fo} + \frac{1}{2}mv_{\perp}^2. \quad (11)$$

While the kinetic freeze-out temperature  $T_{fo}$  is assumed to be the same for all particles, the second term introduces the observed mass dependence of  $T^*$ . The slightly higher  $T^*$  measured at 158A GeV would thus indicate that the average radial expansion velocity still increases between the two energies. However, the  $\Xi$  and  $\Omega$  do not fit into this systematics. At 158A GeV their inverse slope parameter is at the same level as the one measured for the  $\Lambda$ , while at 40A GeV it is significantly lower. Apparently, the multi-strange particles do not participate in the radial flow to the same extent as the particles with one or no strange constituent quark. This also follows from the analysis shown in Fig. 20 [59]. Here the  $m_t$  spectra of the  $\Omega$  are compared to a hydrodynamically inspired model, which assumes a transversely expanding emission source [187]. Such an analysis avoids the problems connected to the use of an inverse slope parameter, whose value for heavy particles can depend on the fit range in  $m_t$ . The parameters of this model are the kinetic freeze-out temperature  $T_{fo}$  and the transverse flow velocity  $\beta_s = v_s/c$  at the surface. Assuming a linear radial velocity profile  $\beta_{\perp}(r) = \beta_s r/R_s$ , as motivated by hydrodynamical calculations, the  $m_t$  spectrum can be computed from

$$\frac{dN}{m_t dm_t dy} \propto \int_0^{R_s} r dr m_t I_0\left(\frac{p_t \sinh \rho}{T_{fo}}\right) K_1\left(\frac{m_t \cosh \rho}{T_{fo}}\right), \quad (12)$$

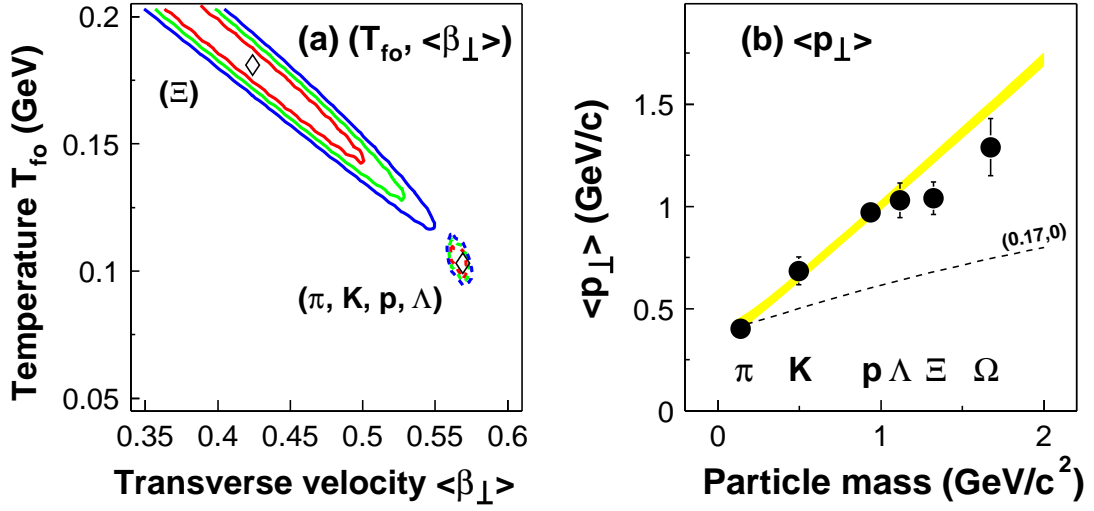


Figure 21: Left: The kinetic freeze-out temperature  $T_{fo}$  versus the transverse flow velocity  $\langle\beta_{\perp}\rangle$  for the hydrodynamically inspired model fits to the  $m_t$  spectra [132]. The 1, 2, and 3 sigma contours are shown. Solid curves are for a simultaneous fit to the  $\Xi^-$  and  $\Xi^+$ . Dashed curves are a separate fit to the  $\pi$ , K, p, and  $\Lambda$  data as measured by the STAR collaboration. The diamonds represent the best fit in both cases (Fig. adapted from [132]). Right: The mean transverse momentum  $\langle p_{\perp} \rangle$  for identified particles as a function of the particle mass [132]. The band follows from the three sigma contour of the fit to  $\pi$ , K, p, and  $\Lambda$ , as shown in the left panel, and the dashed curve is for  $T_{fo} = 170$  MeV and  $\langle\beta_{\perp}\rangle = 0$ .

where  $R_s$  is the radius of the source and  $\rho = \tanh^{-1}\beta_{\perp}$  the boost angle. The curve labeled (A) is calculated with the parameters derived from a simultaneous fit to kaons, (anti-)protons  $\Lambda$ , and  $\phi$  ( $T_{fo} = 90$  MeV and  $\langle\beta_{\perp}\rangle = 0.5$ ). The clear disagreement to the measured  $\Omega$   $m_t$  spectra illustrates that the freeze-out conditions for the  $\Omega$  are different than for the lighter hadrons. A much better agreement can be achieved, if the freeze-out parameters taken from a fit to  $J/\psi$  and  $\psi'$  spectra [191] are used, as shown as curve (B) in Fig. 20. This indicates that the  $\Omega$  has similar kinetic freeze-out conditions than the  $J/\psi$ . The same observation was made at RHIC energies (see Fig. 21). Using the same model different freeze-out parameters are extracted for the  $\Xi$  than for the lighter hadrons. The averaged transverse momentum of the  $\Xi$  and  $\Omega$  departs from the linear increase with particle mass, similar to the inverse slope parameters shown in the right panel of Fig. 19.

The interpretation of this behavior follows from the assumption that rare particles as the  $\Xi$  and  $\Omega$  have a lower hadronic scattering cross section than light hadrons [192] and therefore do not participate in the radial flow that is developing during the hadronic phase of the fireball evolution. This leads to the conclusion that a substantial part of the transverse expansion probed by these particles has to be generated during the partonic phase. Thus, the  $\Xi$  and  $\Omega$  would be directly sensitive to the pressure in the early phase of the reaction. The rapid increase of the inverse slope parameters measured for these particles in the SPS energy range (right panel of Fig. 19) would thus indicate that the partonic part of the flow is beginning to develop at these energies.

The  $m_t$  spectra of kaons provide important information on the transverse dynamics of the reaction system. Calculations within hybrid hydrodynamics and transport approaches [193, 194] indicate that kaons freeze out slightly earlier than nucleons and  $\Lambda$  (e.g. in [195] decoupling times of  $\tau_{fo} \approx 14$  fm/c are found for mesons and  $\tau_{fo} \approx 18$  fm/c for nucleons,  $\Lambda$  and  $\Sigma$ ), and thus they will be less sensitive to the late rescattering phase. Their  $m_t$  spectra can be very well described by a single exponential (Eq. (10)) and can thus be characterized by just one parameter, the inverse slope parameter  $T^*$ . The energy dependence of  $T^*$  for charged kaons exhibits an interesting feature, as shown in Fig. 22. While  $T^*$  is



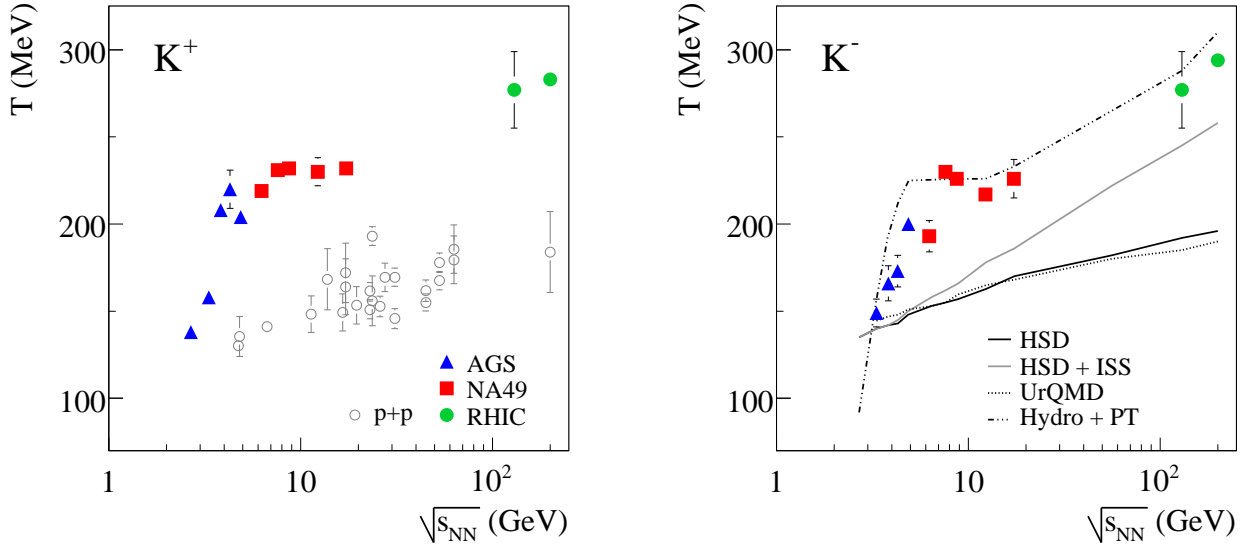


Figure 22: The energy dependence of the inverse slope parameters  $T^*$  of  $K^+$  (left) and  $K^-$  (right) measured at midrapidity in central Pb+Pb and Au+Au collisions [126]. The  $K^+$  slope parameters are compared to results for  $p + p(\bar{p})$  collisions [196] (left). The curves shown in the right panel represent various model predictions.

rising rapidly with center-of-mass energy for  $\sqrt{s_{NN}} < 7 - 8$  GeV, it is rather constant or only slightly increasing above this energy. A similar observation has been made for the averaged transverse mass  $\langle m_t \rangle - m$  of pions and protons [126, 197]. In proton-proton collisions such a behavior is not observed (see left panel of Fig. 22) [196].

The  $dN/dy$  dependence of the mean transverse momentum has been suggested as a signature for a first order phase transition to a deconfined state quite a while ago within the concept of Landau's hydrodynamical model [198]. Originally, this has been proposed as an interpretation of the dependence of  $\langle p_t \rangle$  on  $dN/dy$  observed in  $p + \bar{p}$  collisions at  $\sqrt{s_{NN}} = 540$  GeV. While the fireball volume produced in these reactions is most likely too small to create a QGP state, attempts have been made to apply a similar interpretation to the observed structure in the energy dependence of the inverse slope parameters of kaons [199]. While hadronic transport model calculations are generally not able to properly reproduce the observed structure (see right panel of Fig. 22) [46, 55, 168], the data can be described by a hydrodynamical model assuming a first order phase transition between a hadronic and a deconfined phase (dash-dotted curve in right panel of Fig. 22) [199]. If initial conditions calculated event-by-event with the NEXUS event generator [200, 201] are used, the same model is able to simultaneously describe yields, transverse mass and rapidity spectra. Another hydro approach, which uses a dynamical description of the freeze-out conditions [202], also results in a good match to the data, but turns out to be less sensitive to a specific equation-of-state and thus does not necessarily require a phase transition. A similar observation has been made with a model that combines hadronic transport and hydrodynamics [203]. Also here it was found that the way the freeze-out procedure is implemented can have as much influence on the final result as the equation-of-state that is used. Even though it is quite possible that the measured energy dependence of the inverse slope parameters might be due to a first order phase transition, it is currently difficult to establish an unambiguous theoretical connection. At the moment it is also still unclear whether in the center-of-mass energy range discussed here a first order phase transition is to be expected. While most lattice QCD calculation expect a change from a cross over to a first order phase boundary at higher  $\mu_B$ , corresponding to lower  $\sqrt{s_{NN}}$  [3, 4, 5], the results obtained

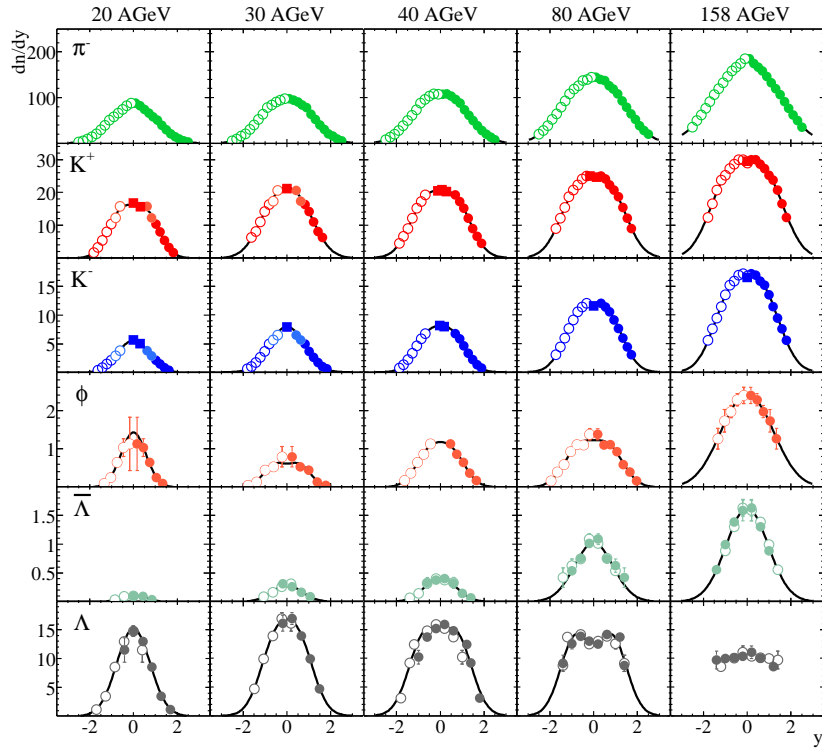


Figure 23: The rapidity spectra of  $\pi^-$ ,  $K^+$ ,  $K^-$ ,  $\phi$ ,  $\bar{\Lambda}$ , and  $\Lambda$  as measured by the NA49 collaboration in central Pb+Pb collisions at 158A GeV [197]. The closed circles indicate measured data points, while open ones are reflected around midrapidity. The solid lines represent fits with a single Gaussian or the sum of two Gaussians.

by [6] rather indicate that the phase transition is of the type of a cross over also at higher  $\mu_B$ .

#### 4.3.2 Rapidity spectra

At the SPS rapidity spectra in the forward hemisphere have been measured by the NA49 collaboration for charged kaons,  $\phi$ , and hyperons at five different beam energies [58, 59, 125, 126, 149]. Part of these spectra are shown for central Pb+Pb collisions in Fig. 23. The NA57 collaboration performed measurements of rapidity distributions for  $K_S^0$ ,  $\Lambda$ ,  $\bar{\Lambda}$ ,  $\Xi^-$ ,  $\bar{\Xi}^+$ , and  $\Omega^- + \bar{\Omega}^+$  in the lab rapidity range  $2.5 < y < 3.5$  for the 53% most central Pb+Pb collisions at 158A GeV [204]. At RHIC no measured rapidity distributions are available for most particle types, since most detectors only cover the midrapidity region. The only exception is provided by the BRAHMS collaboration, which can cover a large part of the forward hemisphere. BRAHMS has measured in central Au+Au collisions at  $\sqrt{s_{NN}} = 64.2$  GeV and 200 GeV rapidity distributions of  $dN/dy$  and  $\langle p_t \rangle$  for charged kaons (see Fig. 24) [166, 174]. In order to avoid assumptions on longitudinal phase space distributions, the measurement of  $dN/dy$  distributions over a large range of rapidities is a prerequisite for the precise determination of  $4\pi$  integrated total yields. Therefore, measurements of the total multiplicities at RHIC energies are only available by the BRAHMS collaboration for charged pions and kaons (see Tables 3–11).

The rapidity spectra of strange mesons can reasonably be described by a Gaussian distribution at all energies [149, 166] (Figs. 23 and 26), although in some cases the sum of two Gaussians, displaced relative to midrapidity, can result in a slightly better fit [125, 126]. This observation is also true for anti-baryons ( $\bar{\Lambda}$ ,  $\bar{\Xi}^+$ ) [58] and for the  $\Omega$  [59]. Baryons, such as the  $\Lambda$  and  $\Xi^-$ , have a wider distribution which is changing drastically with beam energy, because their light valence quark structure is connected

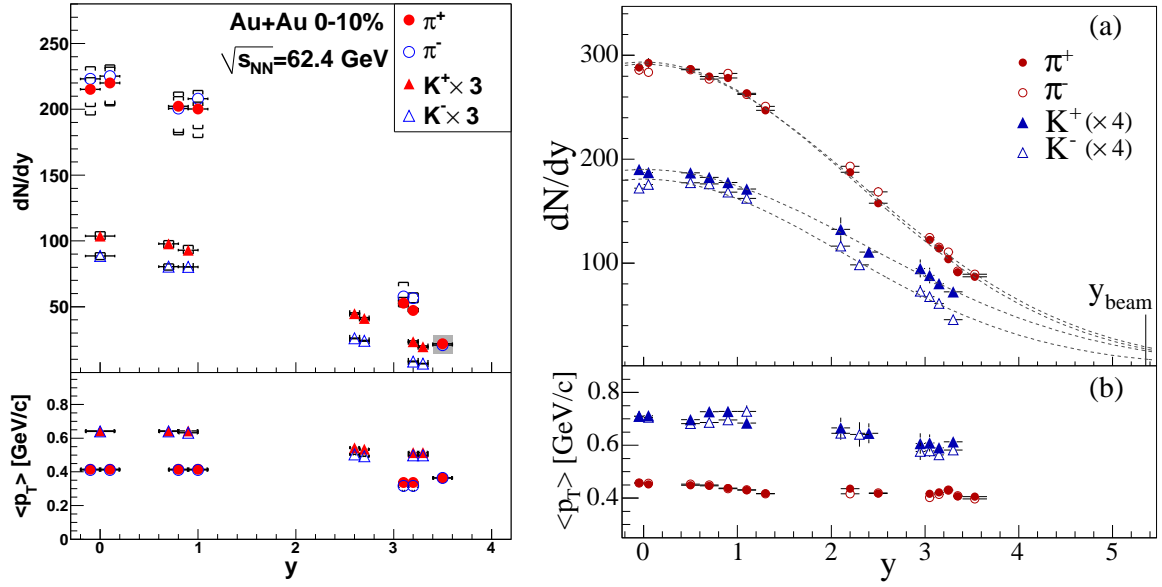


Figure 24:  $dN/dy$  (upper panels) and the averaged transverse momentum  $\langle p_t \rangle$  (lower panels) as a function of rapidity for charged pions and kaons for central Au+Au collisions, as measured by the BRAHMS collaboration at  $\sqrt{s_{NN}} = 62.4$  GeV (left) [174] and at  $\sqrt{s_{NN}} = 200$  GeV (right) [166].

to the ones of the originally colliding nucleons. This is in particular visible for the  $\Lambda$ , whose distribution changes from a Gaussian shape at 20A GeV to a spectrum that is essentially flat inside the measured region at 158A GeV (see lowest row of Fig. 23). No pronounced change with center-of-mass energy is observed for  $\Xi^-$  spectral shapes, but the widths of the rapidity distributions increase significantly faster with  $\sqrt{s_{NN}}$  than the ones measured for  $\Xi^+$  [58]. The reason for this behavior is that  $\Lambda$  and  $\Xi^-$  are sensitive to the longitudinal redistribution of net-baryon number, which depends strongly on center-of-mass energies. While at low SPS energies the net-baryon number is concentrated around midrapidity, its distribution changes very rapidly and turns from a maximum around  $y = 0$  into a shallow minimum at RHIC energies [205, 206]. Consequently, the midrapidity anti-baryon/baryon ratios exhibit a strong energy dependence. With increasing strangeness content of the baryons this effect becomes weaker, as already shown in the right panel of Fig. 9.

The systematics of the RMS widths of the rapidity spectra of  $\pi^\pm$ ,  $K^\pm$ ,  $\phi$ , and  $\bar{\Lambda}$ , i.e. those particles whose longitudinal distributions can be described by Gaussians, is summarized in the left panel of Fig. 25 [149]. For charged pions, kaons, and anti-lambdas the widths  $\sigma$  scale linearly with the beam rapidity  $y_{\text{beam}} = 2 \cosh^{-1}(\sqrt{s_{NN}}/(2m_p))$  in the SPS energy region [197]. The widths depend, at least in the SPS energy region, on the particle type as  $\sigma(\pi^-) > \sigma(K^+) > \sigma(K^-) > \sigma(\bar{\Lambda})$ . However, since at RHIC the width of the  $K^+$  approaches the one of the pions, or is even larger [166], this scaling apparently does not hold up to top RHIC energy.

A peculiar behavior can be observed for the  $\phi$  meson, whose rapidity widths are increasing much faster with beam energy than the ones of the other mesons (left panel of Fig. 25). While at 20A GeV the  $\phi$  has a rapidity distribution that is narrower than the one of the  $K^-$ , its width is comparable to the one of the  $\pi^+$  at 158A GeV. This behavior is at variance with a simple expectation based on kaon coalescence (right panel of Fig. 25). In this case the  $\phi$  rapidity distributions  $\sigma_\phi$  should depend on the measured widths of the kaon rapidity distributions  $\sigma_{K^\pm}$  in the following way:

$$\frac{1}{\sigma_\phi^2} = \frac{1}{\sigma_{K^+}^2} + \frac{1}{\sigma_{K^-}^2}. \quad (13)$$

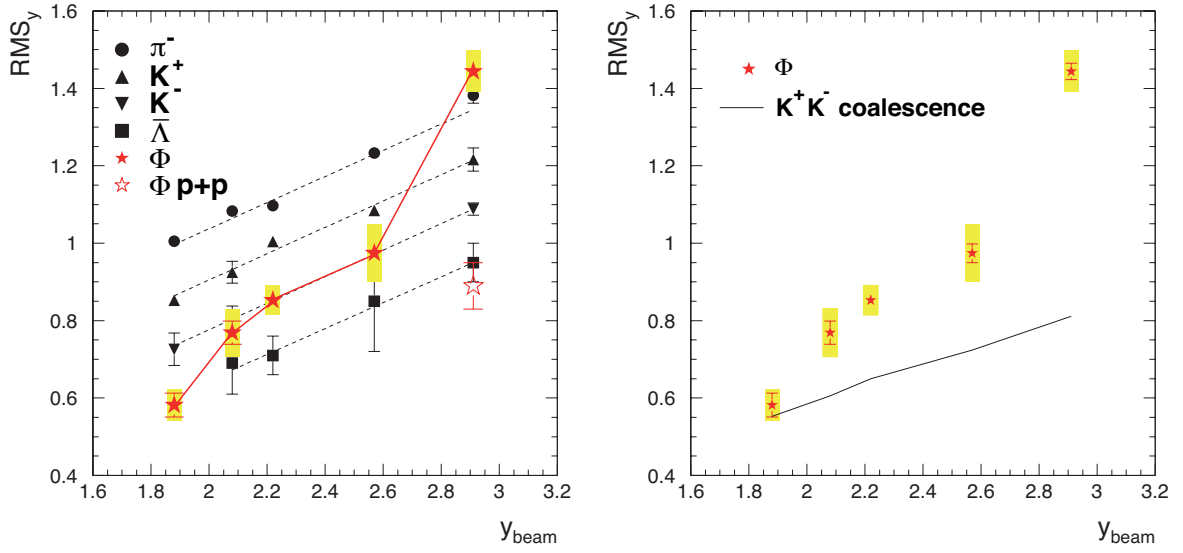


Figure 25: Left: The RMS widths of the rapidity distributions of  $\pi^-$ ,  $K^-$ ,  $K^+$ , and  $\phi$  in central Pb+Pb collisions at SPS energies as a function of the beam rapidity [125, 126, 149, 197]. Right: The widths of the rapidity distributions of  $\phi$  mesons in central Pb+Pb collisions at SPS energies as a function of the beam rapidity [149]. The data are compared to expectations from kaon coalescence (solid line). (The Figs. are adapted from [149].)

As shown in the right panel of Fig. 25, this simple scenario is clearly ruled out for nucleus-nucleus collisions. However, it is interesting to note that for p+p collisions at top SPS energy (158 GeV) the coalescence expectation, derived from the measured kaon rapidity widths according to Eq. (13), is relatively close to the measured  $\phi$  rapidity widths ( $\sigma_{\phi}^{\text{meas.}} = 0.89 \pm 0.06$  [207], compared to  $\sigma_{\phi}^{\text{coal.}} = 0.77$  as based on the kaon measurements in [208]). In addition, it is remarkable that the rapidity widths measured at top SPS energy are significantly wider in central Pb+Pb collisions compared to p+p collisions at the same energy ( $RMS_y(\text{Pb+Pb}) = 1.44 \pm 0.021 \pm 0.054$  [149] and  $RMS_y(\text{p+p}) = 0.89 \pm 0.06$  [207], see also left panel of Fig. 25). For instance, such a significant difference between p+p and A+A is not seen for charged kaons ( $K^+$ :  $RMS_y(\text{p+p}) = 1.20$  and  $RMS_y(\text{Pb+Pb}) = 1.22$ ,  $K^-$ :  $RMS_y(\text{p+p}) = 1.01$  and  $RMS_y(\text{Pb+Pb}) = 1.14$ , both at  $\sqrt{s_{NN}} = 17.3$  GeV [125, 208]).

In a publication by the BRAHMS collaboration [166] the  $K/\pi$  ratios measured at different rapidities for central Au+Au collisions at  $\sqrt{s_{NN}} = 200$  GeV were compared to the corresponding ratios determined at midrapidity, but at different center-of-mass energies. While at top RHIC energy the  $K^-/\pi^-$  ratio drops when going from midrapidity to forward rapidities, the  $K^+/\pi^+$  ratio rises. Since the  $K^+$  production is favored by the presence of baryons via associated production mechanisms (e.g.  $p + p \rightarrow p + K^+ + \Lambda$ ), the higher net-baryon number at forward rapidities at RHIC can thus increase the number of  $K^+$  relative to  $K^-$  and explain the rise in the  $K^+/\pi^+$  ratio. As the net-baryon number at midrapidity is increasing when going toward lower center-of-mass energies, the  $K^+/\pi^+$  ratio should rise to a similar level when the same net-baryon number is reached. Figure 26 contrasts the two dependences. The  $K^+/\pi^+$  ratio measured at very forward rapidities for  $\sqrt{s_{NN}} = 200$  GeV roughly corresponds to the one observed at midrapidity and  $\sqrt{s_{NN}} = 8.7$  GeV. There seems to be a universal dependence of the  $K^-/K^+$  ratio on the  $\bar{p}/p$  ratio, if measurements at different energies and rapidities are compared (see Fig. 16).

In the context of statistical models, this dependence on the net-baryon density is described by the baryo-chemical potential  $\mu_B$ . If the chemical freeze-out temperature is assumed to be constant, which is a good approximation for  $\sqrt{s_{NN}} \geq 17.3$  GeV, the change in  $\mu_B$  caused by the changing net-baryon number or the changing center-of-mass energy would therefore be the only parameter driving

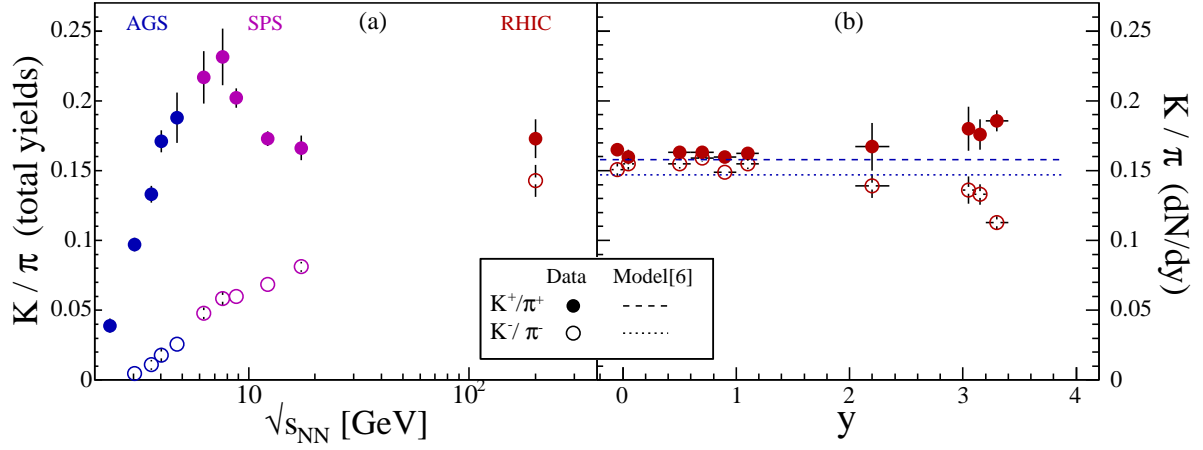


Figure 26: The  $K/\pi$  ratios, measured in full phase space for central Pb+Pb/Au+Au collisions, as a function of  $\sqrt{s_{NN}}$  (left) and of rapidity (right) at  $\sqrt{s_{NN}} = 200$  GeV [166]. The dotted and dashed lines correspond to predictions from a statistical model with rapidity independent freeze-out parameters [209].

the changes in the other particles ratios. However, this is not a universal behavior valid everywhere. For instance, the  $K^+/\pi^+$  ratio is essentially independent of rapidity at  $\sqrt{s_{NN}} = 62.4$  GeV, even though the net-baryons are changing quite dramatically with rapidity [174]. Assuming that there are no large differences between the  $\pi^+$  and  $\pi^-$  rapidity spectra (only  $\pi^-$  spectra have been measured), there are indications that for Pb+Pb collisions at  $\sqrt{s_{NN}} = 17.3$  GeV the  $K^+/\pi^+$  ratio drops instead of rises with increasing rapidity, which is opposite to the behavior seen at  $\sqrt{s_{NN}} = 200$  GeV. This can be deduced from the fact that at  $\sqrt{s_{NN}} = 17.3$  GeV the  $K^+$  rapidity width is smaller than the one for pions (see left panel of Fig. 25) [125], while it is wider at top RHIC energy (see right panel of Fig. 24). Since at  $\sqrt{s_{NN}} = 17.3$  GeV the net-baryon number is slightly rising toward forward rapidities (at least up to  $y = 1.8$  [205]), this would indicate that it is not the only driving factor for the relative strangeness production. As already mentioned in Section 4.2.2, a study of the rapidity dependence of the chemical freeze-out parameters derived from fits with a statistical model shows that both,  $T_{ch}$  and  $\mu_B$ , do depend on rapidity [179]. In the same analysis, it has been found that the dependences on  $y$  are not the same at different center-of-mass energies. The observed dependence of statistical model fit results on whether midrapidity  $dN/dy$  or  $4\pi$  integrated data are used as input (see discussion in Section 2.3) seems to be due to this effect. Strangeness production in the fragmentation region is apparently different than in the central fireball and it starts to affect the measured rapidity distributions for  $\sqrt{s_{NN}}$  below top SPS energies.

## 5 System size dependence

Strange particle production rates in heavy ion collisions, relative to elementary p+p collisions define the strangeness enhancement  $E_S$  (Eq. (6)) as already discussed in Section 3.1 of this article. Whether the strangeness enhancement in larger systems is due only to the phase space suppression in the smaller systems, such as p+p or p+A, or is indeed due to an increased strangeness production from a deconfined partonic medium is still an ongoing discussion.

An rapid increase of the strangeness enhancement factor in small systems (up to  $N_{\text{part}} = 50$ ) has been suggested by canonical models due to the restriction in phase space. In other words the volume is not sufficiently large to contain the necessary strangeness content for statistical strange particle production. Complete statistical production can be assumed when the system reaches its chemical equilibrium and is thermalized. Strangeness equilibration requires a finite number of binary collisions in an extended volume. This can only be achieved if the number of participants is larger than 50. In comparison, the light quark hadrons equilibrate faster, i.e. in a smaller system with less binary collisions. In p+p collisions the underproduction of strangeness due the limited number of binary collisions (one binary collision) is largest, which means that strangeness is suppressed, at least for collision energies up to RHIC energies.

Any centrality scaling of strangeness production with respect to the p+p yield therefore includes a strangeness suppression factor. This means that any apparent strangeness enhancement factor  $E_S$  as a function of centrality is foremost dominated by the transition of a non-equilibrated small heavy ion system into an equilibrated large system. Any remaining additional enhancement could be interpreted as a phase transition signature. The strangeness enhancement as a function of system size,  $N_{\text{part}}$  and as a function of collision energy is shown in Fig. 27 (left) for the  $\Omega$  in Pb+Pb collisions [210].

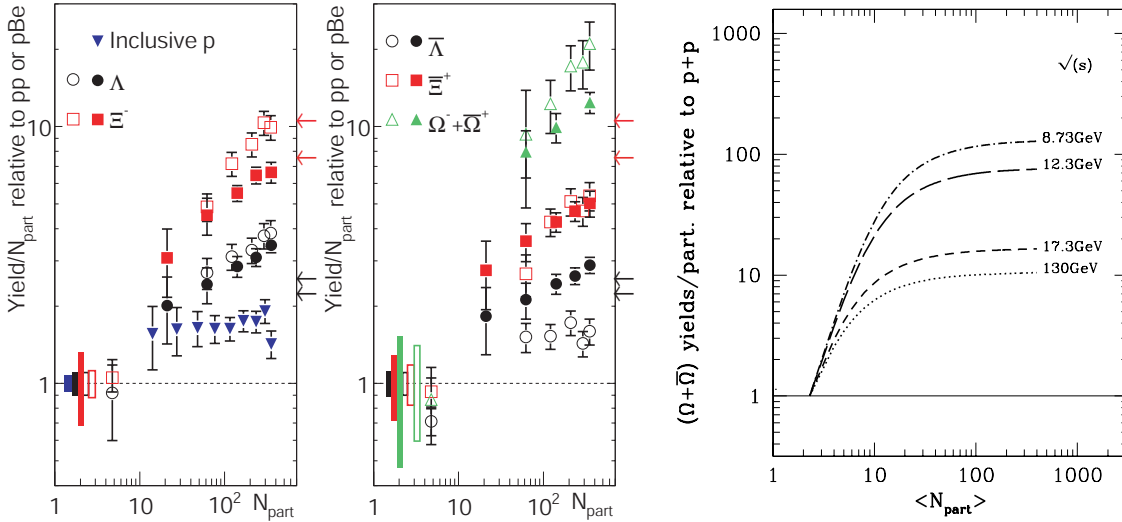


Figure 27: Left: The enhancement of inclusive protons,  $\Lambda$ ,  $\bar{\Lambda}$ ,  $\Xi^-$ ,  $\bar{\Xi}^+$ , and  $\Omega^- + \bar{\Omega}^+$  around midrapidity as measured by the STAR collaboration for Au+Au collisions at  $\sqrt{s_{\text{NN}}} = 200$  GeV (solid symbols) [119] and by the NA57 collaboration for Pb+Pb collisions at  $\sqrt{s_{\text{NN}}} = 17.3$  GeV (empty symbols) [112]. The boxes at unity show the combined statistical and systematical errors in the p+p, respectively p+Be, reference data. The arrows mark statistical model predictions for a grand-canonical ensemble and two different temperatures ( $T_{\text{ch}} = 165$  MeV and  $T_{\text{ch}} = 170$  MeV). Red arrows correspond to  $\Xi^-$  ( $\bar{\Xi}^+$ ), black arrows to  $\Lambda$  ( $\bar{\Lambda}$ ). Right: Centrality dependence of relative enhancement of the yields of  $\Omega^- + \bar{\Omega}^+$  normalized by the number of participants in central Pb+Pb to p+p reactions at different collision energies [210].



When the enhancement factor levels out it suggests that the collision region has reached sufficient size and the small volume size effects can be neglected. In statistical models, the predicted equilibration of the strangeness production, independent of the incident energy, is realized for sufficiently large volumes ( $N_{\text{part}} > 50$ ). At the highest SPS energy and the RHIC energies the  $\Omega$  yield increases by about an order of magnitude due to this phase space effect alone. Lower energies yield an even larger enhancement factor due to the more dominant suppression of strangeness production in small systems. Any additional enhancement due to deconfinement would have to be assessed on top of this 'trivial effect', i.e. it should manifest itself as an enhancement relative to the equilibrium value. Since it is assumed that at RHIC energies and below the QGP will arise only in sufficiently large systems, a systematic study of the volume dependence of the enhancement factor might give information about the onset of QGP creation.

Recent results from the LHC in elementary collisions might indicate that in high multiplicity events a phase transition might occur in p+p collisions. At RHIC energy, though, this evidence could not be obtained due to the low collisions energy [211, 212, 213].

The dependence of strangeness production on the system size (volume) of the collisions has been investigated via two methods, either by the variation of the target and beam nucleus species or by the selection of the centrality (impact parameter) of the collisions. In order to characterize the collision geometrical calculations such as Glauber [115, 116] models are used to determine the interaction volume, the number of participating nucleons (= wounded nucleons) and the number of binary collisions in the heavy ion reaction.

Measurements from STAR and NA57 at  $\sqrt{s_{\text{NN}}} = 200$  GeV and  $\sqrt{s_{\text{NN}}} = 17.3$  GeV are shown in left panel of Fig. 27. They reveal a steady increase of strange hadron production with increasing system size ( $N_{\text{part}}$ ) and increasing strange quark content. A saturation (leveling off of the enhancement factor) for large systems as predicted by statistical models is not detected. In fact, the enhancement factor continues to increase up to the most central collision ( $N_{\text{part}} = 350$ ). This observation can have different explanations. For instance, it might suggest that even in the most central events the full equilibrium value of a grand-canonical ensemble is not yet reached for multi-strange particles.

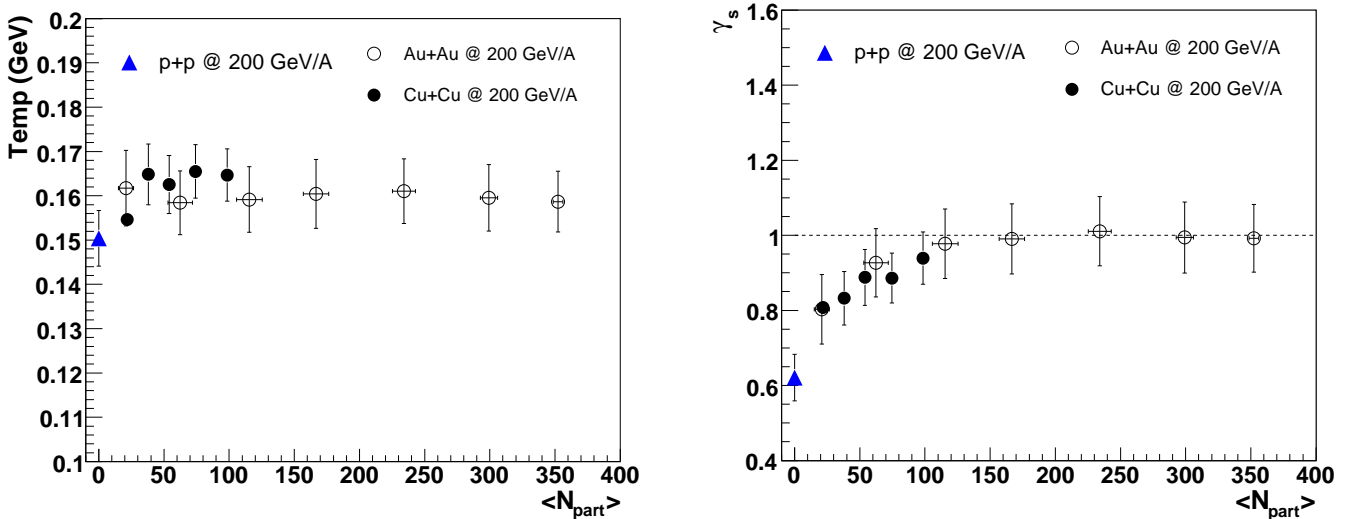


Figure 28: Temperature (left) and strangeness saturation factor ( $\gamma_s$ ) (right) as a function of the number of participants ( $N_{\text{part}}$ ) for all particles measured by the STAR experiment [214, 216], as obtained with the THERMUS code [67].

An alternative explanation for the enhancement above  $N_{\text{part}} = 50$  would be the observation of strangeness enhancement due to a QGP phase in a grand-canonical system, i.e. in systems where the volume effects of the strangeness suppression from p+p is not present anymore. Calculations of the strangeness saturation factor  $\gamma_s$  (Fig. 28 right), using a thermal model fit to STAR data [214, 215] are consistent with this interpretation. The saturation factor  $\gamma_s$  approaches unity for  $N_{\text{part}} = 100$ , which can be interpreted as evidence for an equilibrated and strangeness saturated system at these system sizes. Therefore, any further enhancement of strangeness production from  $N_{\text{part}} = 100$  on might be related to an additional contribution from a deconfined medium. At RHIC energies this could account for about half of the enhancement factor for  $\Omega$  baryons measured in central Au+Au collisions and compared to p+p collisions.

## 5.1 Core and corona model

A different conclusion can be reached if one considers a description of the interaction region in a heavy ion collision, which distinguishes between independent core and corona volumes in centrality dependent heavy ion collisions [157, 217, 218, 219]. Here the dense core behaves like a QGP volume, whereas the surrounding corona can be understood as a superposition of independent p+p collisions. The justification for such an approach is based on the realistic modeling of the nuclear surface rather than the very schematic rigid sphere calculations used in earlier models.

The effect of core-corona models is best investigated in the centrality dependence of particle production since the corona fraction continues to increase for the more peripheral systems. In other words, the core fraction, which represents the QGP volume, increases with centrality. The system might be equilibrated in a grand-canonical regime even at small  $N_{\text{part}}$  but due to the volume to surface ratio increase the strangeness enhancement factor continues to increase.

In order to investigate the strangeness enhancement, this volume effect of the core-corona ratio has to be taken into account and subtracted from the measured strangeness enhancement factor. The remaining enhancement will be the real "strangeness enhancement".

### 5.1.1 Centrality dependence

To investigate the strangeness enhancement as a function of the collision centrality the additional effects of the change in surface to volume ratio will be taken into account by unfolding the source into a corona (surface) and core term. The total volume is the superposition of the core and corona volume. Both areas will be treated independently, i.e. there are no interactions between core and corona particles.

As a consequence of this superposition in heavy ion collisions one has to calculate the relative weight, in terms of particle production, of core and corona separately as a function of centrality. The particle production of the core volume is described by a partonic medium in thermal equilibrium whereas the corona is described by the nucleon-nucleon collisions modeled by a statistical hadronization model [157] (Becattini) or alternatively by the EPOS model [218].

Figure 29 (left) shows the corona participants ( $N_{\text{PC}}$ ) as a function of the number of total participants  $N_{\text{part}}$ , which increases slightly with centrality. Although the number of corona participants increases their relative fraction of ( $N_{\text{PC}}/N_{\text{part}}$ ) drops dramatically from around 50% at  $N_{\text{part}} = 50$  to 10% at  $N_{\text{part}} = 350$ . This fraction can be calculated either with a Glauber model (red squares) or from a fit (green points) to the strange particle yields of K,  $\Lambda$ ,  $\phi$ ,  $\Xi$  and  $\Omega$  (Fig. 31) when using relative contributions from corona and core type mechanisms as shown in Fig. 29 (right). The fitted  $N_{\text{PC}}$  and the  $N_{\text{PC}}$  from Glauber model calculations are in agreement. However the errors on the corona participants  $N_{\text{PC}}$  derived from the data are very large and therefore not sensitive to falsify this approach.

To quantify the relative contribution of the two components, the fraction of nucleons that scatter more than once  $f(N_{\text{part}})$  can be used.  $f(N_{\text{part}})$  can simply be calculated with a Glauber model [115].



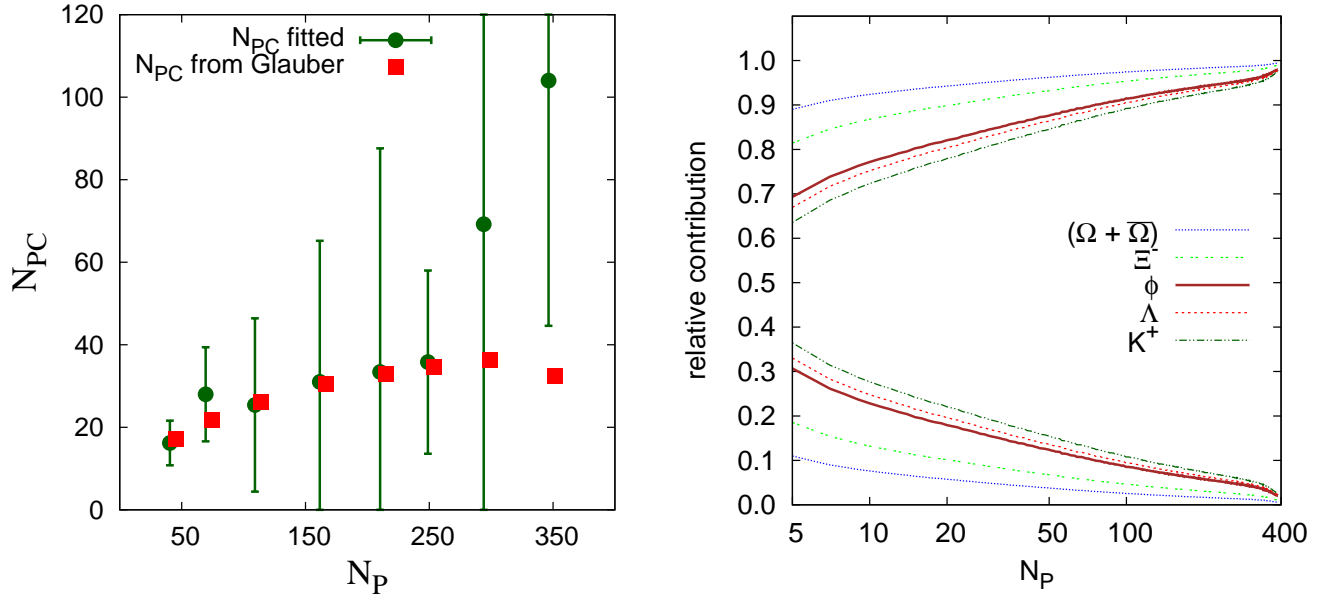


Figure 29: Left: Number of corona participants  $N_{PC}$  at different centralities as a function of the total number of participants  $N_P$ . The square dots denote the values calculated with a Glauber model while the round ones denote the values arising from fitting  $N_{PC}$  as a free parameter. The round symbols are shifted 5 units of  $N_P$  leftward for clarity. Right: Fraction of produced particles coming from core (upper lines) and corona (lower lines) as a function of centrality [220] (Becattini).

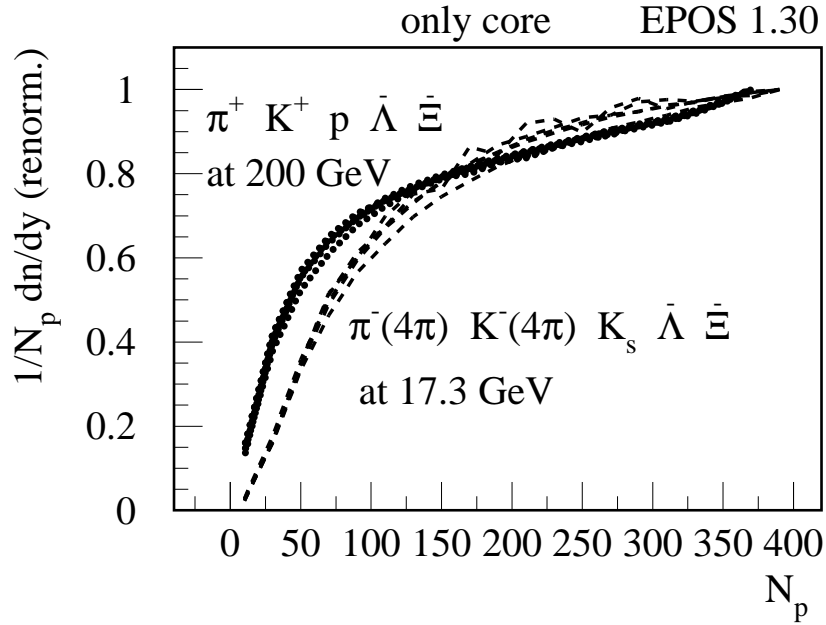


Figure 30: Multiplicity per participant as a function of  $N_P$  for the core part only. The results for  $\pi^-$ ,  $K^-$ ,  $\bar{p}$ ,  $\bar{\Lambda}$ ,  $\Xi^+$  in Au+Au collisions at  $\sqrt{s_{NN}} = 200$  GeV (dotted lines), and for  $\pi^-$ ,  $K^-$ ,  $K_s^0$ ,  $\bar{\Lambda}$ ,  $\Xi^+$  in Pb+Pb collisions at  $\sqrt{s_{NN}} = 17.3$  GeV (dashed lines) (Fig. is adapted from [218] (EPOS)).

This quantity allows for a natural interpolation between the yields  $Y$  measured in elementary p+p

( $= Y_{\text{corona}}$ ) and in central nucleus-nucleus collisions ( $= Y_{\text{core}}$ ):

$$Y(N_{\text{part}}) = N_{\text{part}} [f(N_{\text{part}}) Y_{\text{core}} + (1 - f(N_{\text{part}})) Y_{\text{corona}}] \quad (14)$$

The contribution of the core part alone is shown in Fig. 30 for a calculation using the EPOS model, which can be compared to the result from an alternative model by Becattini shown in Fig. 29 (right). The overall trend of increased particle production from the core volume of these models is the same. However, the particle yields differ, mostly in the region of small number of participants. This discrepancy can be investigated experimentally after statistically more significant data samples are obtained in particular for either small collisions systems or peripheral collisions of the heavy systems.

In summary, the derived strangeness enhancement factors from different core-corona models shown in Fig. 31 (left: Becattini, right: EPOS) describe the steady increase of the data from p+p up to the most central heavy ion collisions.

The  $\Xi^+$  yields in the more central collisions are better described by Becattini than the EPOS Model. However, this model is over-predicting the  $\Xi^+$  yield for peripheral collisions in the range of  $N_{\text{part}} < 60$ , which might be a hint that the centrality dependence cannot exclusively be described by a core/corona volume effect.

A final interpretation of this result will depend strongly on the modeling of the core volume. If the dynamics of the produced particles require the system to be partonic in nature, which is also indicated by measurements of the radial and anisotropic expansion of the system, then the enhanced strangeness production is not just a volume effect, but indeed a signature for deconfinement, at least in the core of the collision volume. The main contribution of the core-corona models to this discussion is a more precise understanding of the centrality dependence of the strange particle production which goes beyond the simple phase space argument of strangeness suppression in small systems.

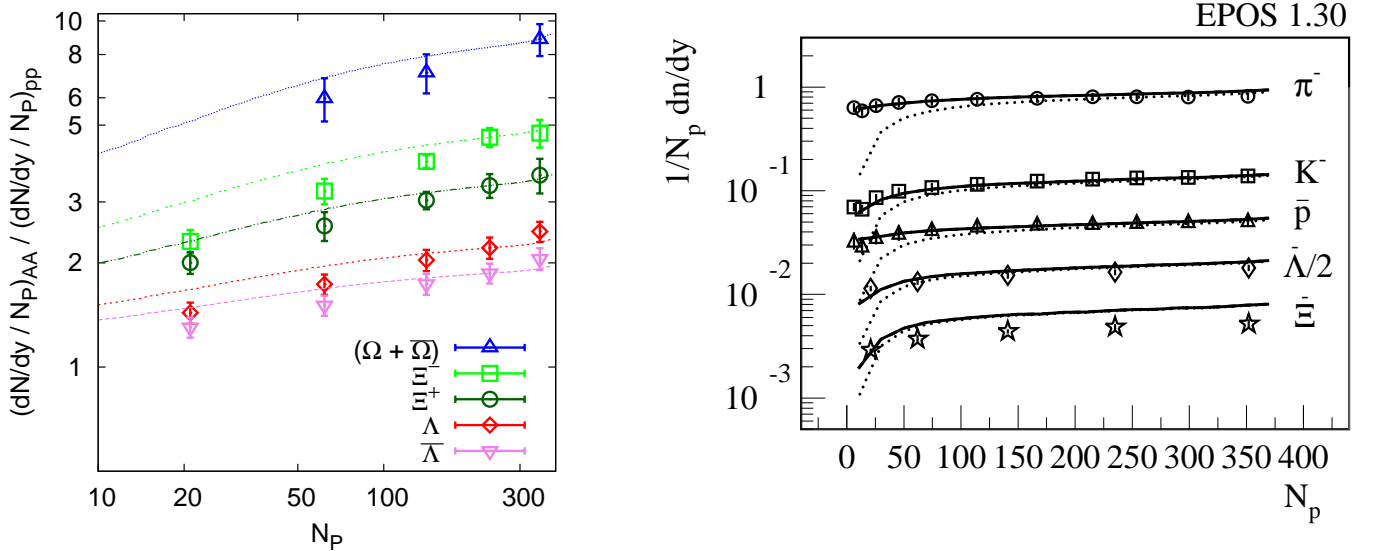


Figure 31: Left: Hyperon rapidity density measured in Au+Au collisions normalized to measurements in p+p collisions and the number of participants at  $\sqrt{s_{\text{NN}}} = 200$  GeV as a function of the number of participants [119]. The lines are theoretical calculations from Becattini et al. [157, 220]. Right: Rapidity density  $dN/dy$  per participant as a function of the number of participants ( $N_P$ ) in Au+Au collisions at  $\sqrt{s_{\text{NN}}} = 200$  GeV (RHIC) for  $\pi^-$ ,  $K^-$ ,  $\bar{p}$ ,  $\bar{\Lambda}$ ,  $\Xi^-$  together with the full calculation (full lines) and the core part only (dotted lines) (Fig. is adapted from [218] (EPOS)).

### 5.1.2 Comparison of different collision systems

A measurement which might also be explained by the core-corona approach is the apparent difference of the strangeness enhancement factors for different collision systems at the same  $N_{\text{part}}$ . This was first measured at the SPS [221] and has since then been corroborated at RHIC energies [222].

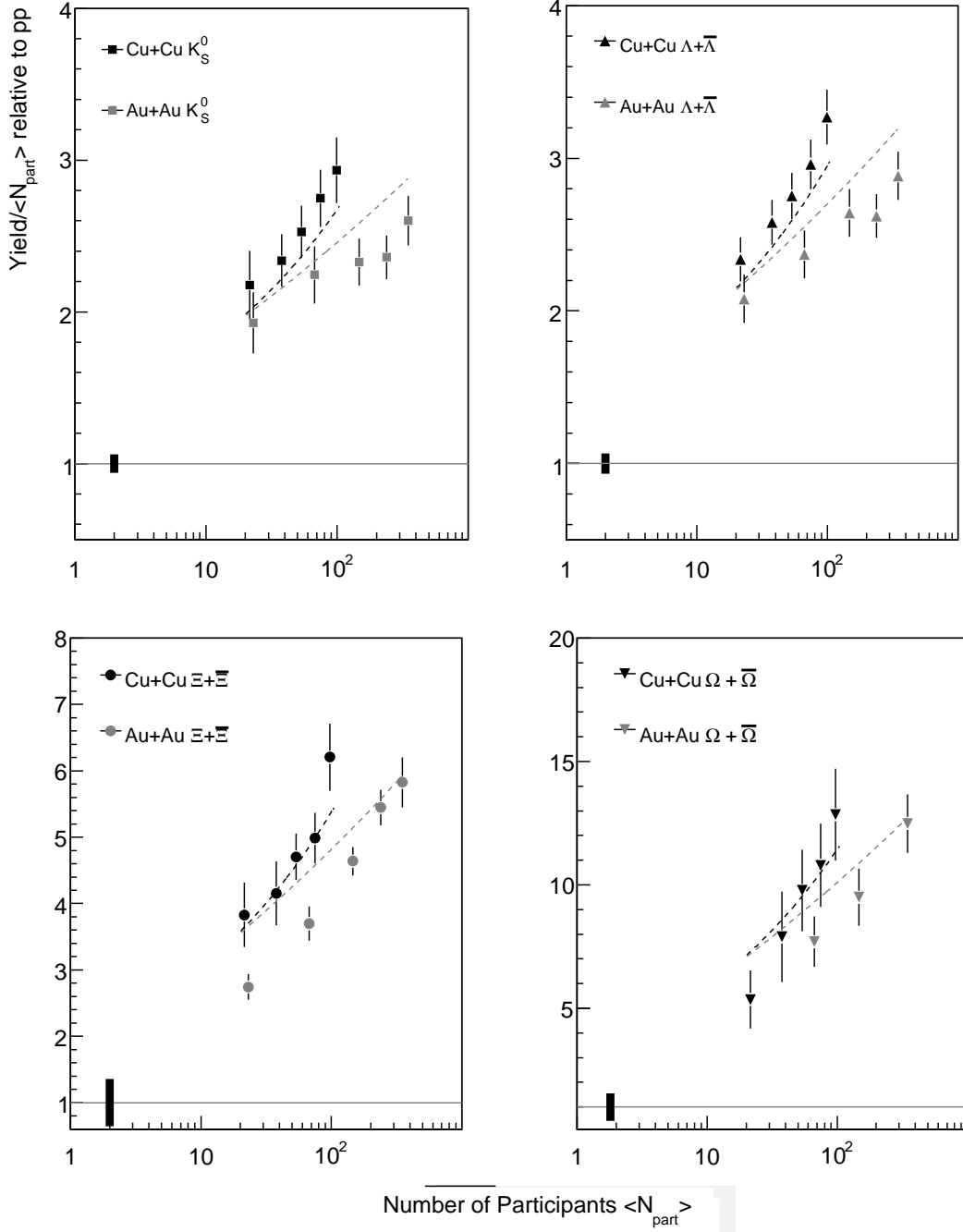


Figure 32: The enhancement factor for (multi-)strange particles at midrapidity in Cu+Cu and Au+Au collisions at  $\sqrt{s_{\text{NN}}} = 200$  GeV. The  $\Lambda$  and  $\bar{\Lambda}$  yields have been feed-down subtracted in all cases. The Au+Au multi-strange data have been previously published [133]. The black bars show the normalization uncertainties, and the uncertainties for the heavy ion points are the combined statistical and systematic [222]. The lines represents calculations with the EPOS model [218].

Figure 32 shows the difference between the Cu+Cu and Au+Au systems at  $\sqrt{s_{\text{NN}}} = 200$  GeV collision energy. For all strange particle species the smaller system exhibits larger strangeness enhancement at the same  $N_{\text{part}}$  as is summarized in Fig. 32. A possible explanation is the larger core in Cu+Cu compared to Au+Au when using a core-corona approach. At the same  $N_{\text{part}}$  the Cu+Cu collision system features a larger core fraction and thus a larger number of participants that undergo multiple collisions according to Glauber calculations. This is implemented in EPOS which describes the trend of the data in Cu+Cu better than in Au+Au collision in Fig. 32. On the other hand the effect is also visible in the AMPT model which does not feature separate core and corona volumes but rather uses string breaking and mini-jet fragmentation to describe the medium. In general though it seems true that at the same  $N_{\text{part}}$  the Cu+Cu system yields a larger contribution to the strangeness yield than the more peripheral Au+Au system.

## 5.2 Scaling with $N_{\text{part}}$ and $N_{\text{bin}}$

In the case of a chemically equilibrated bulk system of light quarks we expect rather  $N_{\text{part}}$  scaling than  $N_{\text{bin}}$  scaling for the centrality dependence of the particle yields. This is true, for example, for the protons at RHIC energies (Fig. 27 left). Their enhancement factor, which presumes  $N_{\text{part}}$  scaling, is constant as a function of the system size. In other words, the increase in proton production from peripheral to central heavy ion collisions scales with the number of participants. This hints at the dominant production of up and down quarks through thermal parton-parton interactions rather than hard scattering.

$N_{\text{part}}$  scaling does not necessarily prove that the system in its early stage is thermalized. A particle species, whose initially produced yield scales with  $N_{\text{bin}}$  and is thus not chemically equilibrated, might thermally equilibrate in the hadron phase through elastic scattering and exhibit flow features and a thermal  $p_t$  spectrum in central collisions. On the other hand, species for which the yield scales with  $N_{\text{part}}$  might exhibit non-thermal behavior in their kinematic spectra.

Generally heavier quarks (i.e. charm and bottom) are not expected to equilibrate chemically or thermally, and are mostly produced through initial parton-parton interactions which scale with the number of binary collisions,  $N_{\text{bin}}$ . Since the strange particle yield continues to increase beyond the  $N_{\text{part}}$  scaling relative to p+p, this could be viewed as a non-equilibrium signature for strange quarks. An alternative scaling method, based on an independent normalization of the constituent quarks in a hadron was suggested by H. Caines. The method takes into account the specific scaling behavior of the strange quark, which is the  $N_{\text{bin}}$  scaling. The new factor is defined as [223]:

$$C_{\text{scaling}} = \frac{N_{\text{light}} \times N_{\text{part}}}{N_q} + \frac{N_s \times N_{\text{bin}}}{N_q} \quad (15)$$

where  $N_q$  is the number of quarks in the particle,  $N_{\text{light}}$  is the number of light (u and d) quarks, and  $N_s$  is the number of strange quarks. Figure 33 right shows the relation of  $N_{\text{part}}$  and  $N_{\text{bin}}$  for different collision energies based on a Glauber calculation [115, 116]. These numbers are used to calculate the new enhancement factors in Fig. 33 left, which shows a flat distribution for all light and strange quark particle species.

This new scaling is successful on the level of 20%. Thus one could conclude that the strange quark indeed scales with  $N_{\text{bin}}$  and is thus mostly produced through initial gluon-gluon interactions. However, one exception is the scaling of the  $\phi$ , which according to Eq. (15) should scale with  $N_{\text{bin}}$ , but appears to scale better with  $N_{\text{part}}$ .

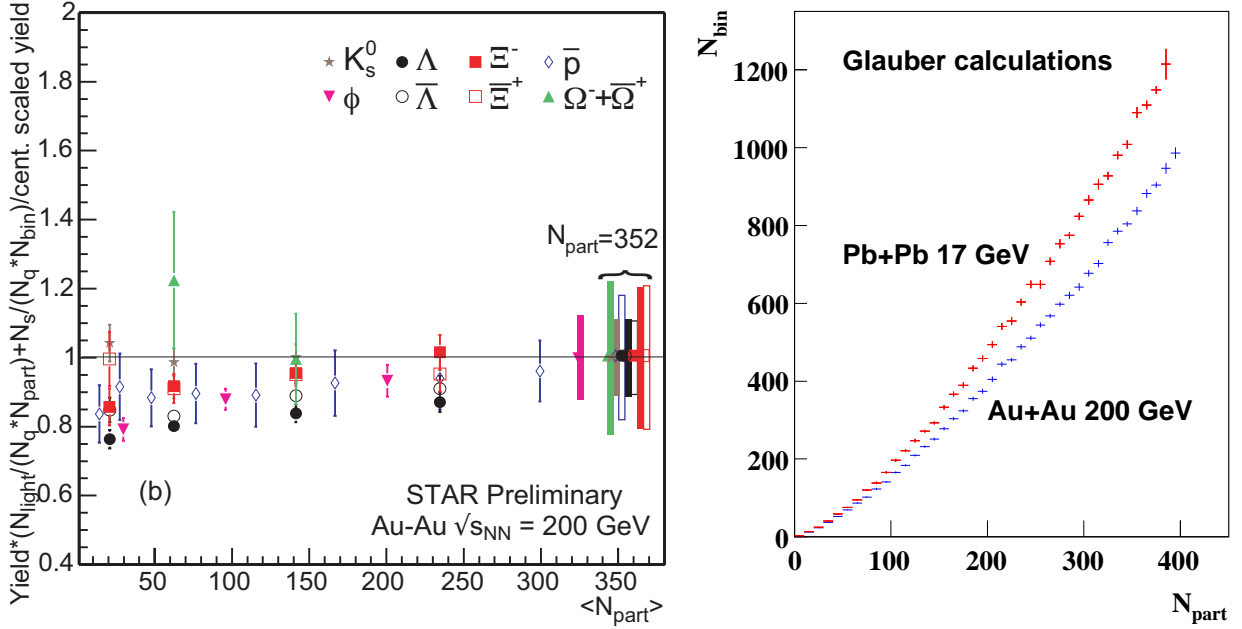


Figure 33: Left: Au+Au data scaled as defined by Eq. (15) except the  $\phi$ , which is scaled by  $N_{\text{part}}$ . All data are normalized to the most central bin [223]. Right: Number of participants versus number of binary collisions using Glauber calculation for Pb+Pb and Au+Au collision systems at  $\sqrt{s_{\text{NN}}} = 17.3$  GeV and  $\sqrt{s_{\text{NN}}} = 200$  GeV [115, 116].

## 6 Strangeness at intermediate and high $p_t$

The bulk of the particles ( $> 90\%$ ) produced in heavy ion collisions carry low momentum ( $p_t < 2$  GeV/ $c$ ) and are produced either through soft multiple parton scattering or statistical production from a thermal medium. The intermediate  $p_t$  range is commonly defined as the region between  $p_t = 2$  and 6 GeV/ $c$  and can be considered the transition region between hard processes, described by pQCD, and the aforementioned soft region. Hadron production from pure fragmentation of the hard scattered parton is only dominant at  $p_t > 6$  GeV/ $c$  based on the RHIC heavy ion results. In a medium we expect a modified parton fragmentation [225, 226, 227] which presumably softens the fragmentation function, i.e more soft particles are produced in the emitted hadron jet and pushed into a region which is dominated by the physics of the bulk. In this picture the particles in the intermediate  $p_t$  range can be due to either a large radial expansion which adds additional kinetic energy to the bulk or an enhanced quenching of high  $p_t$  jet fragments traversing the medium. An additional alternative arises if one takes into account the possibility of forming color neutral objects through recombination of partons in the deconfined medium. This recombination mechanism for hadronization has been first introduced for elementary collisions in the late 70's [28]. When applied to heavy ion collisions the initial system is a thermalized partonic medium in which partons close in phase space can recombine to form a hadron with momentum from the sum of the quark momentum.

Since the thermal spectrum of partons is likely to have a slightly higher mean momentum than the pions from the kinetic freeze-out, and the total momentum of the final hadrons depends on the number of added quarks, this mechanism populates predominantly the mid- $p_t$  range and favors baryon over meson production at a fixed intermediate  $p_t$  [29, 30]. Thus the two main experimental measures to quantify the interplay of bulk, fragmentation and recombination processes are the  $p_t$  dependent baryon to meson ratio and the  $p_t$  dependent nuclear suppression factors. Here we will first discuss the baryon to meson ratios.

## 6.1 Baryon to meson ratios

The enhanced baryon/meson ratio in the transition from  $p_t = 2 - 6$  GeV/ $c$  in heavy ion collisions indicates that particle production from the deconfined medium is neither simply statistical in nature nor can it be described through fragmentation alone. The earliest RHIC measurements of the  $p/\pi$  ratio show an increase up to  $p_t = 3$  GeV/ $c$  to unity [127, 228], a value much higher than in elementary p+p collisions [229, 230].

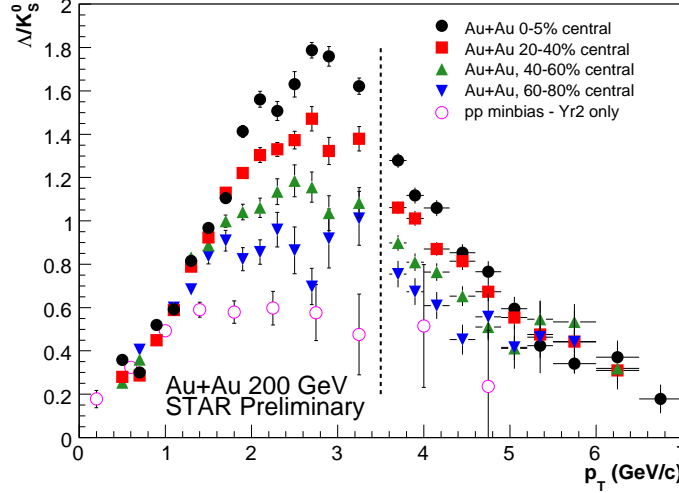


Figure 34: The  $\Lambda/K_S^0$  ratio as a function of  $p_t$  for different collision centralities for Au+Au collisions at  $\sqrt{s_{NN}} = 200$  GeV [224].

For the strange sector Fig. 34 shows the  $\Lambda/K_S^0$  ratio in Au+Au collisions at  $\sqrt{s_{NN}} = 200$  GeV out to  $p_t = 6$  GeV/ $c$  for different centralities [224]. The maximum of the distribution is at  $p_t = 2.8$  GeV/ $c$  for all collision systems including the elementary p+p collisions. However, the maximum value of the ratio for p+p collision is below unity, while it continues to increase for more central Au+Au collisions up to 1.8 in the 5% most central collision. This remarkable value means that in certain momentum regions baryon production dominates over meson production by almost a factor of two. Such an effect is impossible to model in fragmentation where the baryon production relies on the formation of di-quark out of the fragmenting proton and is thus considerably reduced in probability.

Early attempts to describe this phenomenon tried to merge a radially expanding bulk system, which pushes higher mass particles (baryons) to larger momenta than lower mass particles (mesons), with a common quenching model for high momentum hadrons [231]. Such a model qualitatively leads to a 'pile-up' of the baryon to meson ratios at mid- $p_t$ , although a quantitative comparison has never been attempted. On the other hand thermal recombination models became more quantitative over the years and now also take into account unique strangeness aspects in these particle ratios. The general recombination approach is based on the idea that since the thermal parton spectrum is exponentially falling as a function of momentum, the probability to form a high momentum three quark state is higher than the forming a two quark state of the same final state momentum. The effect is per se not unique to strange particles as shown by  $p/\pi$  ratio, but certain aspects of the process can be tested when comparing to non-strange ratios. First, the models require thermalization of the strange parton in the system prior to hadron formation [31]. Second, the relevant degree of freedom in those models is the constituent quark, i.e. the modeling requires quarks to have a finite mass which differs between  $u$ ,  $d$  and  $s$ -quarks by about 100 MeV/ $c^2$  [32]. More recent models even include recombination between bulk partons and the non-thermal hard partons [33]. These models are successful in describing the pure strange ratio of  $\Omega/\phi$  up to  $p_t \sim 4$  GeV/ $c$  as shown in Fig. 35 [232], which includes more than 95%

of the hadron yield. This is of particular relevance since the small hadronic production cross section for  $\Omega$  and  $\phi$  particles requires the particle generation to occur through partonic rather than hadronic recombination. At higher  $p_t$  the model fails for the coalescence of thermal quarks and the combination of thermal and shower (total) quarks. Only the decreasing trend of  $\Omega/\phi$  from the total quark (thermal and shower) combination is visible. Since most of the  $\phi$ -mesons are made via coalescence of seemingly thermalized  $s$ -quarks in central Au+Au collisions, the observations imply that a hot and dense matter with partonic collectivity has been formed at RHIC energies.

Although coalescence models assume particle production from a source of thermal partons their results can be incompatible with thermal equilibrium of the final hadrons in the low  $p_t$  (bulk) region. They should therefore only be applied to hadrons in a medium  $p_t$  range (e.g. 2 - 6 GeV/c). In order to not violate entropy conservation, another production mechanism is required to produce a thermal reservoir of bulk particles below 2 GeV/c. Above  $\approx 6$  GeV/c it is likely that parton fragmentation will be the most dominant mechanism.

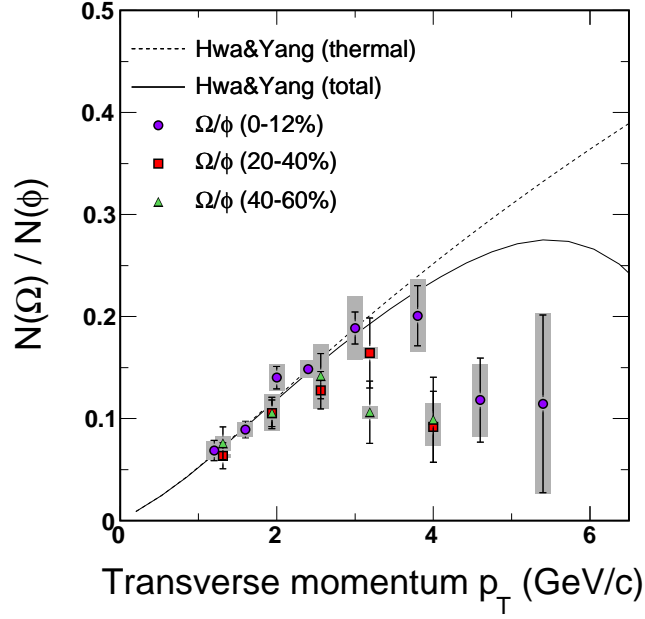


Figure 35: The  $N(\Omega)/N(\phi)$  ratio vs.  $p_t$  for three centrality bins in  $\sqrt{s_{NN}} = 200$  GeV Au+Au collisions. The solid and dashed lines represent recombination model predictions for central collisions [33] for total and thermal contributions, respectively [232]. However the coalescence model should be applied for  $p_t > 2$  GeV/c only.

## 6.2 Nuclear suppression factors ( $R_{AA}$ and $R_{CP}$ )

In order to study the medium modification of the hard process one has to determine the yield as a function of momentum. These  $p_t$  dependent studies can be quantified via the nuclear modification factor defined by the yield in p+p ( $d^2\sigma^{NN}/dp_t dy$ ) and A+A ( $d^2N^{AA}/dp_t dy$ ) collisions, normalized by the binary collision scaling factor  $N_{bin}$  and the inelastic cross section for p+p collisions ( $\sigma_{inel}^{NN}$ ):

$$R_{AA} = \frac{\sigma_{inel}^{NN}}{N_{bin}^{AA}} \frac{d^2N^{AA}/dp_t dy}{d^2\sigma^{NN}/dp_t dy} \quad (16)$$

Since the accumulation of sufficient statistics in the elementary p+p collisions required several run periods, the early RHIC results on nuclear suppression were based on  $R_{CP}$ , which is the momentum

dependent yield of central ( $d^2N^{\text{cent}}/dp_t dy$ ) divided by the peripheral ( $d^2N^{\text{per}}/dp_t dy$ ) collisions and normalized by their respective number of binary collisions ( $N_{\text{bin}}$ ) (see Fig. 36 right).

$$R_{\text{CP}} = \frac{N_{\text{bin}}^{\text{per}}}{N_{\text{bin}}^{\text{cent}}} \frac{d^2N^{\text{cent}}/dp_t dy}{d^2N^{\text{per}}/dp_t dy} \quad (17)$$

For non-strange light quark particles this observable is roughly equivalent to  $R_{\text{AA}}$  since the light flavor production scales well from p+p to peripheral A+A collisions. In the strange sector, though, one would expect a distinct difference between  $R_{\text{CP}}$  and  $R_{\text{AA}}$  based on the strangeness suppression in the elementary collisions which was discussed in the previous chapter.  $R_{\text{CP}}$  attempts to eliminate this phase space effect by normalizing the central spectrum to a more peripheral spectrum where one expects the strangeness suppression to be already minimized.

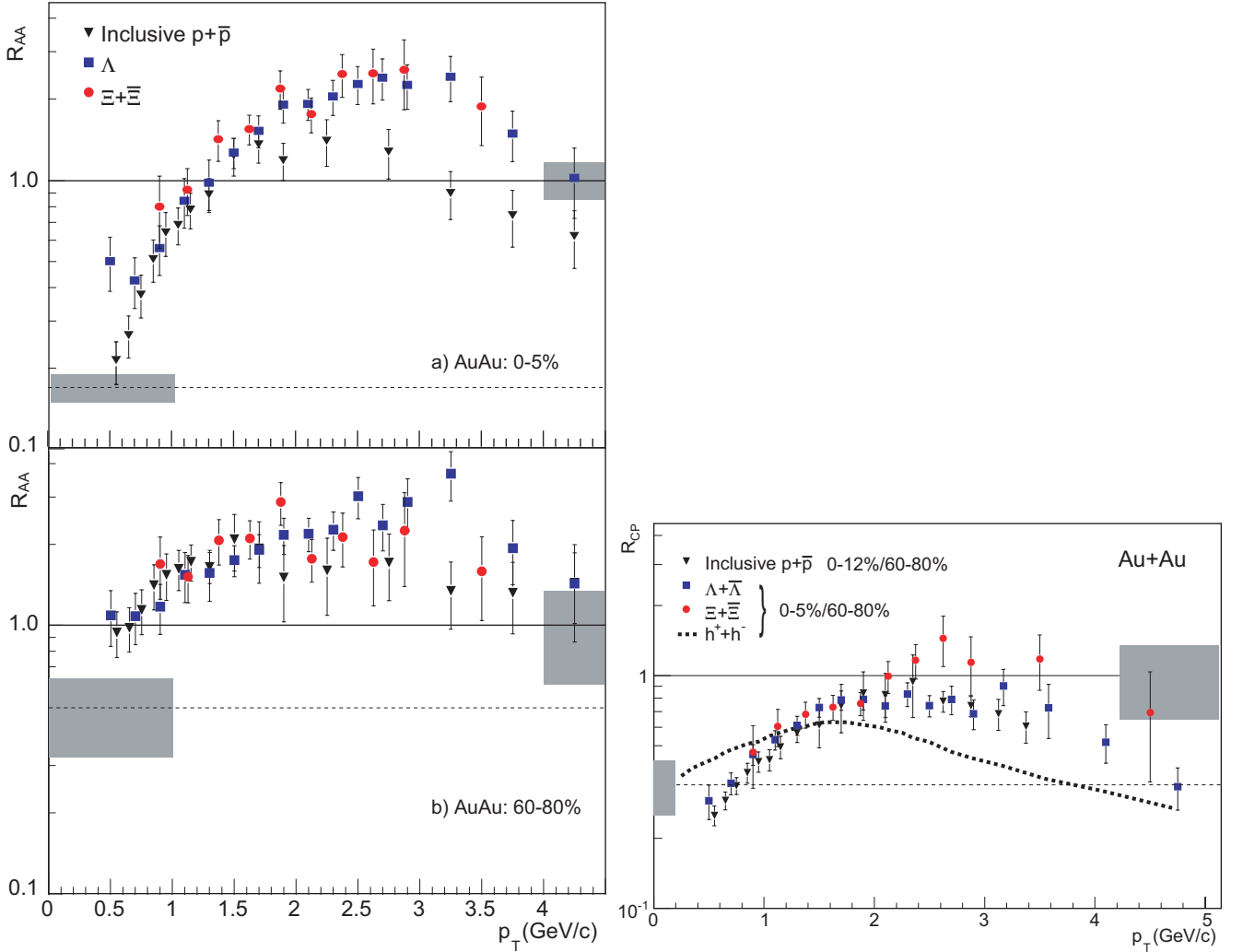


Figure 36: Left:  $R_{\text{AA}}$  for p+p [233, 234],  $\Lambda$  and  $\Xi^- + \bar{\Xi}^+$  for a) 0-5% and b) 60-80% most central Au+Au events at  $\sqrt{s_{\text{NN}}} = 200$  GeV. Right:  $R_{\text{CP}}$  measured in Au+Au events for  $\bar{p}$  (0-12%/60-80%) [234],  $\Lambda + \bar{\Lambda}$  and  $\Xi^- + \bar{\Xi}^+$  (0-5%/60-80%) [133]. The dashed curve shows the results for  $h^+ + h^-$  for 0-5%/60-80% [235]. In all plots the statistical and systematical errors are included. The band at unity shows the uncertainty on the binary scaling  $N_{\text{bin}}$  and the dashed line indicates the participant scaling ( $N_{\text{part}}$ ) with its uncertainty in a gray band.



Fig. 36 right shows that the  $R_{CP}$  of  $\Lambda$  is in agreement with the  $R_{CP}$  of protons out to  $p_t = 3.5$  GeV/ $c$ , while the  $R_{CP}$  of the  $\Xi$  shows slight enhancement in the higher  $p_t$  region. However, the errors are too large to draw any conclusion about an enhancement of strange particles with respect to non-strange particles.

Fig. 36 left shows  $R_{AA}$  for  $\Lambda$  and  $\Xi$  compared to inclusive  $p+\bar{p}$  measurements [233, 234]. The  $R_{AA}$  distributions of strange particles reach a maximum greater than unity for central (top) and for peripheral (bottom) events, which would imply a scaling close to binary collisions. In central Au+Au collisions the protons are significantly lower than the strange baryons.

Measurements of  $R_{CP}$  have shown that the Cronin effect cannot account for the relative difference between  $R_{AA}$  and  $R_{CP}$  between light quark and strange quark particles and among the strange particles themselves. It seems that the Cronin effect scales with the hadronic mass rather than the flavor content. Thus the Cronin effect for lambdas and protons is almost identical [236, 237], where the  $R_{AA}$  values are very different above  $p_t = 2$  GeV/ $c$ .

The momentum dependent strangeness enhancement is very similar in central and peripheral collisions, while the protons are consistent with  $R_{AA} = 1$  in central collisions. The extension of the measurement to higher momenta might show if the protons and strange baryons show the same  $p_t$  suppression. It is notable that the  $\Lambda$  and  $\Xi$   $R_{AA}$  values are in agreement with each other, which is not the case for the strangeness enhancement factors shown in the previous section. The  $\Omega$  might help further to separate the strangeness enhancement from the high  $p_t$  suppression.

## 7 Elliptic flow $v_2$ of strange particles

The elliptic flow  $v_2$  is the azimuthal momentum space anisotropy of particle emission from non-central collisions in the transverse direction with respect to the beam direction. Elliptic flow is described by the second harmonic coefficient of an azimuthal Fourier decomposition of the momentum distribution.

Elliptic flow is an observable which is directly related to the initial spatial anisotropy of the nuclear overlap region in the transverse plane, translated into to the observed momentum distribution of identified particles if quarks interact and thermalize in the early stage. It is important to understand the initial geometry and how it varies with the collision centrality and system size. To compare the strength of  $v_2$  of different centralities one has to correct for the initial eccentricity with respect to the reaction-plane of the collisions. A review of this experimental measurements can be found in [238].

### 7.1 $v_2$ scaling as a function of momentum

The  $v_2$  results are not unique to strangeness and thus we will only discuss them briefly in the context of mass and quark number scaling. Generally, any  $v_2$  discussion needs to distinguish between the low  $p_t$  regime, where hydrodynamics holds, and the high  $p_t$  regime, where quark number scaling indicates non-bulk production of the particles and their collective behavior. Up to  $p_t = 2$  GeV/ $c$  the strange meson and baryon fit very well in the hydrodynamic systematics, which assumes that the collective strength scales with the final hadron mass. Above 2 GeV/ $c$  the strange and non-strange particles do not scale with the hadron mass but rather with the number of valence quarks. This has been attributed to the fact that the partons in the thermal system prior to hadronization are already flowing collectively and then simply recombine into a hadron that flows with the added collectivity of all valence quarks. This can also be attributed to hydrodynamics but in the partonic system rather than the hadronic system, which is one of the signatures of the formation of the deconfined collective partonic phase.

Figure 37 shows the experimental evidence for this effect, and an attempt to address the universality of the quark number scaling by analyzing the centrality dependence of the scaling properties.

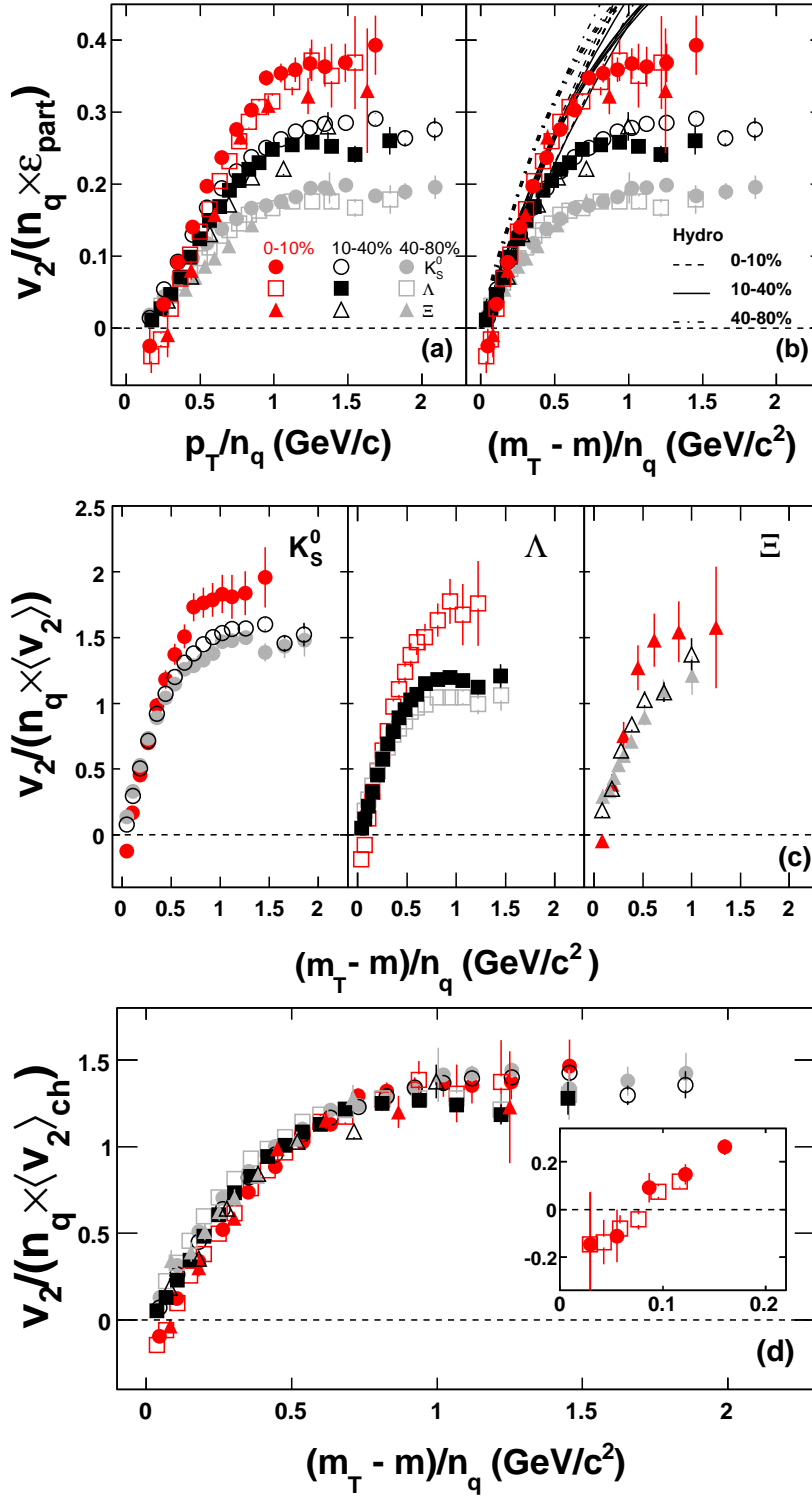


Figure 37: Elliptic flow  $v_2$  scaled by the number of quarks ( $N_q$ ) and participant eccentricity ( $\epsilon_{\text{part}}$ ),  $(v_2 / (N_q \times \epsilon_{\text{part}}))$ , of identified particles (particle + anti-particle) versus (a) the scaled  $p_T/N_q$  and (b)  $(m_T - m)/N_q$  for three centrality bins. For comparison, ideal hydrodynamic model calculations [245] are shown as lines in (b). In (c) the same data from (b) is shown, but scaled by the integrated  $v_2$  of each particle, instead of  $\epsilon_{\text{part}}$ . In (d) the data from (b) scaled by the integrated  $v_2$  of all charged hadrons is presented. The inset in (d) expands the low  $m_T$  region. The error bars only represent the statistical uncertainties. All data are for  $\sqrt{s_{\text{NN}}} = 200$  GeV Au + Au collisions [239].

Here the scaled  $v_2$  is normalized first by the participant eccentricity  $\epsilon_{\text{part}}$  derived from a Monte Carlo Glauber calculation. The plots (a) and (b) show the doubly scaled quantities from three centrality bins as a function of  $p_t/N_q$  and  $(m_t - m)/N_q$ , respectively, which takes out the hadronic mass dependence. It is interesting to note that, in both cases, at a given centrality the elliptic flow of all hadrons scales as observed for minimum-bias events. Upon dividing by the eccentricity the stronger collective motion in more central collisions becomes apparent, which is qualitatively consistent with ideal hydrodynamic model calculations, shown as lines in (b). However, there is no universal scaling with eccentricity in the STAR data which is in disagreement with the conclusions reached by PHENIX [242].

To further clarify the issue, instead of dividing the measured  $v_2$  by the corresponding eccentricity, in (c) the averaged  $v_2$  as a function of transverse momentum weighted with the measured spectra is shown. This scaling seems to work better, however, different hadrons seem to have different values of  $v_2$ , in particular for the top 10% centrality bin at the higher  $m_t$ .

In (d) the doubly scaled  $v_2$  is shown. This time the integrated values of  $v_2$  are extracted from the measurements of unidentified charged hadrons in the corresponding centrality bins. In this case the scaling seems to work best. It is interesting to point out that at the most central bin (see inset in (d)) the values of  $v_2$  become negative at low  $p_t$  for all hadrons. This is most likely caused by the strong radial flow developed in central Au+Au collisions, which has also been observed at SPS energies.

## 7.2 Partonic versus hadronic flow

Further evidence for early partonic collectivity is given by investigating in particular the flow of purely strange hadrons i.e. the  $\Omega$  and the  $\phi$ , both of which are expected to exhibit a significantly reduced interaction cross section with the surrounding hadronic medium. Figure 39 shows the  $v_2$  for multi-strange baryons in STAR. From these early measurements it could already be deduced that the  $\Xi$   $v_2$  follows the quark number scaling of the non-strange baryons. Recent preliminary high statistics measurements by STAR for vector mesons and multi-strange baryons are shown in Fig. 38 [241]. It is evident that they follow in strength and scaling exactly the same pattern than the light quark hadrons. Thus a major portion of the collective motion has to be developed in the early partonic stage.

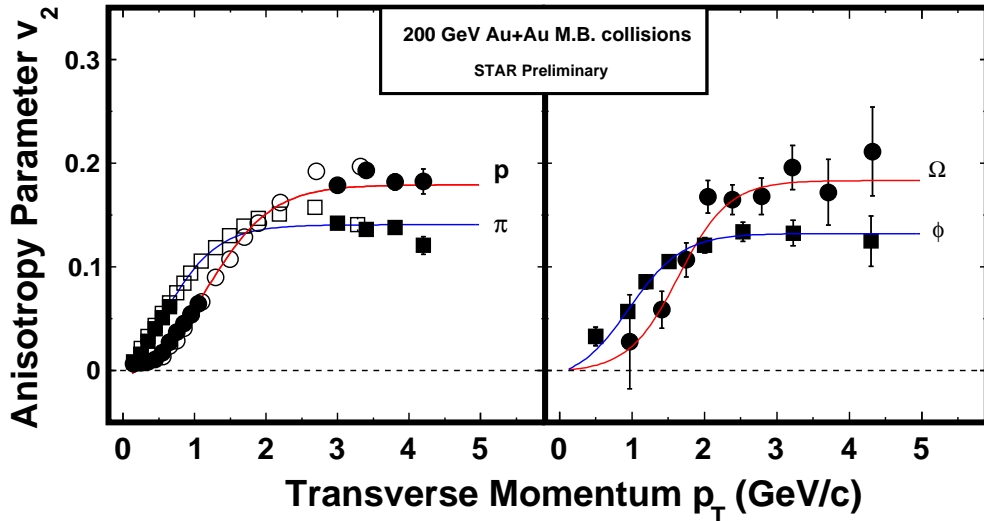


Figure 38: Right: Elliptic flow  $v_2$  as a function of  $p_t$  for  $\pi$ ,  $p$  (left) and  $\phi$ ,  $\Omega$  (right) in Au+Au minimum-bias collisions at  $\sqrt{s_{NN}} = 200$  GeV from STAR. Open symbols represent results from PHENIX [242]. Lines represent a fit inspired by the number of quark scaling [243].

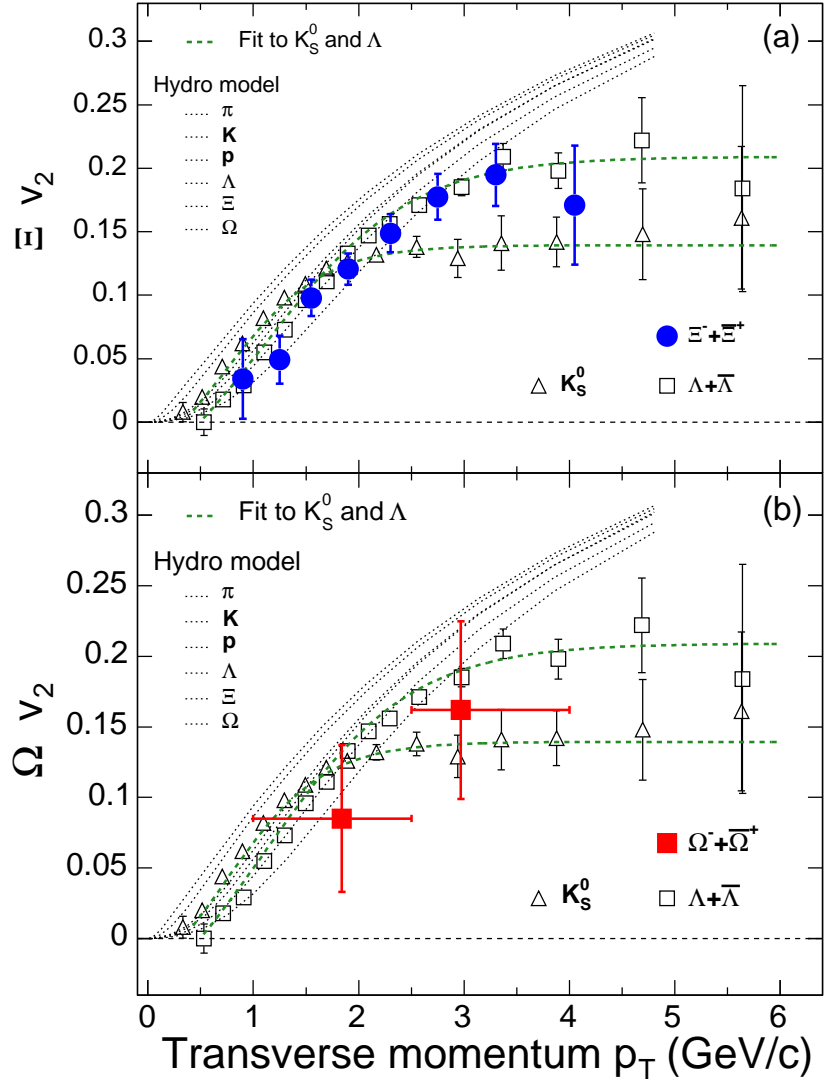


Figure 39: Elliptic flow  $v_2$  of (a)  $\Xi^- + \bar{\Xi}^+$  and (b)  $\Omega^- + \bar{\Omega}^+$  for  $\sqrt{s_{NN}} = 200$  GeV Au+Au minimum-bias collisions. The  $v_2$  of  $K_S^0$  and  $\Lambda$  [246] are shown as open symbols, and the results of the fits [243] are shown as dashed lines. Hydrodynamic model calculations [244] are shown as dotted lines for  $K$  and  $\Lambda$  and as solid lines for  $\Xi^-$  and  $\Omega^-$  masses, from top to bottom, respectively [240].

## 8 Conclusions

The wealth of data on strange hadron production collected in the recent years at the CERN-SPS and RHIC-BNL has allowed to establish a long list of observations on the properties of hot and dense hadronic matter produced in heavy ion reactions. The following list summarizes the main findings as discussed in the previous sections:

- The enhancement of the production of strange hadrons per participating nucleon relative to elementary p+p(Be) collisions is a well established experimental fact. The observed enhancement increases with the strangeness content of the hadron.
- A clear onset of the strangeness enhancement with center-of-mass energy has not yet been observed. In fact, the enhancement of particles with single strangeness increases toward lower energies in contrast to naive expectations.
- Transport models involving only hadronic degrees of freedom are not able to describe the measured enhancement of multi-strange baryons.
- Statistical models generally provide a reasonable description of strange particles yields at all energies. The properties of the fireball are determined by the chemical freeze-out parameters  $\mu_B$  and  $T_{ch}$ . These turn out to fall on a single freeze-out curve, if the center-of-mass energy is varied.
- A pronounced maximum of the relative strangeness production is seen around  $\sqrt{s_{NN}} = 7 - 8$  GeV and the energy evolution of the inverse slope parameters of kaon  $p_t$  spectra exhibits a drastic change in the same region. Both have been interpreted as an indication for a drastic change of the properties of the fireball due to the onset of deconfinement.
- The scaling properties of the  $\phi$  meson seem to rule out kaon coalescence as the dominant production mechanism. It might be more likely that from SPS energies upwards its origin is to a large extend partonic.
- The transverse mass spectra of  $\Xi$  and  $\Omega$  suggest that their kinetic freeze-out is happening in an earlier and hotter phase of the fireball evolution. The radial flow observed in these particles would thus be mainly partonic by origin and starts to build up in the SPS energy regime already. This is corroborated by the substantial elliptic flow of the  $\Omega$  and  $\phi$  measured at RHIC, which, due to their small hadronic cross section, can only develop in a partonic phase.
- The measured system size dependence reveals a more complicated pattern as predicted by statistical models via the transition from a canonical to a grand-canonical ensemble. The contribution of a deconfined phase might also alter the system size dependence in a significant way in addition to the volume effects in the statistical description. However, the observed behavior can to a large extend be explained in a natural way by the core-corona approach. Alternatively, the assumption that the strange quark production, in contrast to the  $N_{part}$  scaling of up and down quarks, scales with the number of binary collisions works with the notable exception of the  $\phi$  meson.
- Strange particles provide valuable information on the flavor dependence of intermediate and high  $p_t$  effects, such as high  $p_t$  suppression. The observed high baryon-meson ratio indicates that quark coalescence is dominating over fragmentation at intermediate  $p_t$ . The observed quark number scaling of the elliptic flow at intermediate  $p_t$  points to a partonic origin of the early pressure in the fireball.

Starting from the original suggestion of using strange particles as a probe for quark-gluon plasma formation, strangeness has turned out to be a versatile tool to study the properties of the matter produced in high energy nuclear reactions and has revealed many unexpected effects. Even though the interpretation of the observed strangeness enhancement might not be as straight forward as originally suggested, it seems there is no consistent explanation without invoking partonic degrees of freedom. Models that include only hadronic degrees of freedom are not able to describe the enhancement of multi-strange particles. Instead one finds that statistical approaches assuming full equilibration result in a much better description. Also the scaling properties of the  $\phi$  meson yields and spectra indicate that from SPS energies onwards its dominant production mechanism is of partonic origin, i.e. quark coalescence, while kaon coalescence cannot explain the observed features. This point of view is further strengthened by the phenomenology of radial and elliptic flow of strange particles and follows from the fact that particles with low hadronic cross section ( $\phi$ ,  $\Xi$ ,  $\Omega$ ) exhibit significant radial flow and that the elliptic flow of strange particles scales with the number of constituent quarks.

Important questions that remain are for instance: Is there a clear onset of strangeness enhancement observable when increasing the center-of-mass energy? There are some features in the existing data (the maximum of the  $K^+/\pi^+$  ratio and a sudden change in the energy dependence of the inverse slopes parameters of kaon  $p_t$  spectra) that can be interpreted in this way, but additional support for this findings is desirable. Can a unique connection of the enhancement of multi-strange particles to partonic equilibration be established or is this a result of other properties of the hadronization processes? What is the excitation function of flow phenomena (radial and elliptic) of strange particles and could this help to uniquely define the onset of deconfinement? Upcoming measurements at high energies (LHC), but also at lower energies (FAIR, RHIC, SPS) will provide important contributions to this strange and exciting picture.

## Acknowledgments

The authors would like to thank A. Andronic, J. Aichelin, F. Becattini, R. Bellwied, M. Bleicher, E. Bratkovskaya, M. Gaździcki, C. Greiner, H. Oeschler, K. Redlich, K. Šafařík, and H. Ströbele for many helpful and inspiring discussions. Special thanks go to A. Andronic, R. Bellwied, K. Šafařík, H. Ströbele and T. Schuster for reading the document and providing valuable corrections and comments.

This work was supported by U.S. Department of Energy Office of Science under contract numbers DE-FG02-94ER40845 and de-sc0003892/DE-PS02-09ER09-26.

## 9 Data compilation

### 9.1 Energy dependence

Figures 40 and 41 and the Tables 3–11 summarize the current data available on strange particle production in central Pb+Pb and Au+Au collisions.

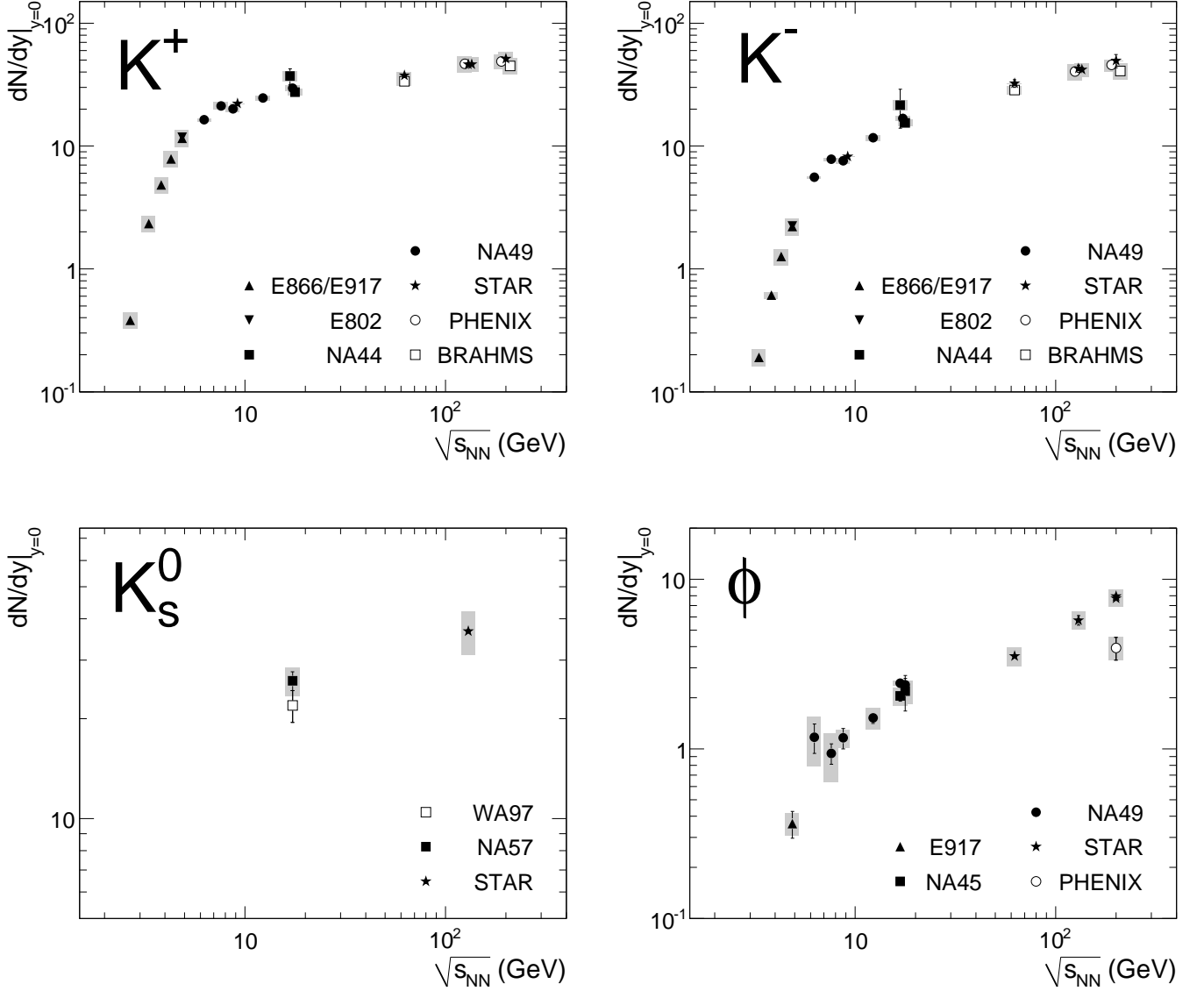


Figure 40: The rapidity densities  $dN/dy$  around midrapidity for  $K^+$ ,  $K^-$ ,  $K_S^0$ , and  $\phi$  measured in central nucleus-nucleus collisions as a function of  $\sqrt{s_{NN}}$ . The systematic errors are represented by the gray boxes.

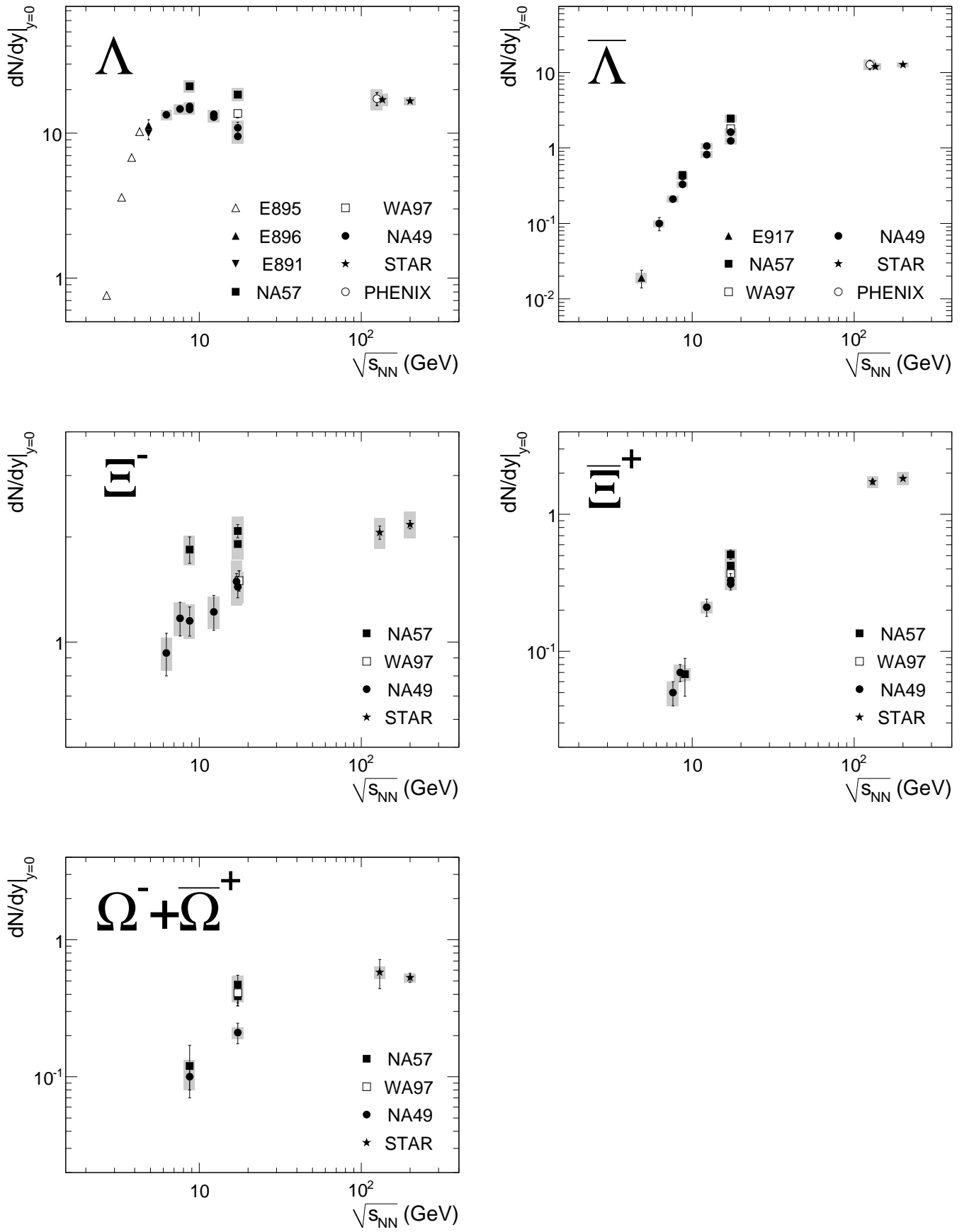


Figure 41: The rapidity densities  $dN/dy$  around midrapidity for  $\Lambda$ ,  $\bar{\Lambda}$ ,  $\Xi^-$ ,  $\bar{\Xi}^+$ , and  $\Omega^- + \bar{\Omega}^+$  measured in central nucleus-nucleus collisions as a function of  $\sqrt{s_{NN}}$ . The systematic errors are represented by the gray boxes.



Table 3: The rapidity densities  $dN/dy$  around midrapidity and the total multiplicities  $\langle N \rangle$  of  $K^+$  as measured in central nucleus-nucleus collisions at different  $\sqrt{s_{NN}}$ . Also listed are the centrality selection (Cent.) and the averaged number of participants ( $\langle N_{\text{part}} \rangle$ ). In most cases the statistical (first) and systematic (second) errors are given separately, while for a few measurements the quadratic sum of both is quoted (denoted by 'sum').

$\sqrt{s_{NN}}$ (GeV)	System	Cent.	$\langle N_{\text{part}} \rangle$	$dN/dy$	$\langle N \rangle$	Exp.	Ref.	Comnt.
2.68	Au+Au	0-5%		$0.381 \pm 0.015 \pm 0.057$	—	E866/E917	[163]	
3.32	Au+Au	0-5%		$2.34 \pm 0.05 \pm 0.35$	—	E866/E917	[163]	
3.83	Au+Au	0-5%		$4.84 \pm 0.09 \pm 0.73$	—	E866/E917	[163]	
4.29	Au+Au	0-5%		$7.85 \pm 0.21 \pm 1.18$	—	E866/E917	[163]	
4.87	Au+Au	0-5%		$11.55 \pm 0.24 \pm 1.73$	—	E866/E917	[163]	
4.87	Au+Au	0-5%	354	$11.79 \pm 0.37 \pm 1.77$	$24.2 \pm 0.9 \pm 3.6$	E802	[160]	
4.96	Au+Au	0-4%	363	—	$23.7 \pm 1.6 \pm 2.3$	E802	[161]	
6.27	Pb+Pb	0-7%	349	$16.4 \pm 0.6 \pm 0.4$	$40.7 \pm 0.7 \pm 2.2$	NA49	[126]	
7.62	Pb+Pb	0-7%	349	$21.2 \pm 0.8^{+1.5}_{-0.9}$	$52.9 \pm 0.9^{+3.0}_{-3.5}$	NA49	[126]	
8.73	Pb+Pb	0-7%	349	$20.1 \pm 0.3 \pm 1.0$	$59.1 \pm 1.9 \pm 3.0$	NA49	[125]	
9.2	Au+Au	0-10%	317	$23.0 \pm 4.4(\text{sum})$	—	STAR	[247]	
12.3	Pb+Pb	0-7%	349	$24.6 \pm 0.2 \pm 1.2$	$76.9 \pm 2.0 \pm 4.0$	NA49	[125]	
17.3	Pb+Pb	0-5%	362	$29.6 \pm 0.3 \pm 1.5$	$103.0 \pm 5.0 \pm 5.0$	NA49	[125]	
17.3	Pb+Pb	0-4%		$37.1 \pm 5.4(\text{sum})$	—	NA44	[248]	a)
17.3	Pb+Pb	0-3.7%		$27.5 \pm 0.2 \pm 1.6$	—	NA44	[175]	b)
62.4	Au+Au	0-10%		$33.6 \pm 0.8 \pm 2.7$	—	BRAHMS	[174]	c)
62.4	Au+Au	0-5%	347	$37.6 \pm 2.7(\text{sum})$	—	STAR	[122]	
130.0	Au+Au	0-6%	344	$46.3 \pm 3.0(\text{sum})$	—	STAR	[122]	
130.0	Au+Au	0-6%		$46.2 \pm 0.6 \pm 6.0$	—	STAR	[130]	
130.0	Au+Au	0-5%	348	$46.7 \pm 1.5 \pm 7.0$	—	PHENIX	[171]	
200.0	Au+Au	0-5%	351	$51.3 \pm 6.5(\text{sum})$	—	STAR	[122]	
200.0	Au+Au	0-5%	351	$48.9 \pm 6.3$	—	PHENIX	[128]	
200.0	Au+Au	0-10%	328	$45.0 \pm 0.67 \pm 6.75$	—	BRAHMS	[129]	
200.0	Au+Au	0-5%		—	$286.0 \pm 5.0 \pm 23.0$	BRAHMS	[166]	d)

Table 4: The rapidity densities  $dN/dy$  around midrapidity and the total multiplicities  $\langle N \rangle$  of  $K^-$  as measured in central nucleus-nucleus collisions at different  $\sqrt{s_{NN}}$ . Also listed are the centrality selection (Cent.) and the averaged number of participants ( $\langle N_{part} \rangle$ ). In most cases the statistical (first) and systematic (second) errors are given separately, while for a few measurements the quadratic sum of both is quoted (denoted by 'sum').

$\sqrt{s_{NN}}$ (GeV)	System	Cent.	$\langle N_{part} \rangle$	$dN/dy$	$\langle N \rangle$	Exp.	Ref.	Comnt.
3.32	Au+Au	0-5%		$0.19 \pm 0.01 \pm 0.03$	—	E866/E917	[163]	
3.83	Au+Au	0-5%		$0.61 \pm 0.02 \pm 0.09$	—	E866/E917	[163]	
4.29	Au+Au	0-5%		$1.26 \pm 0.04 \pm 0.19$	—	E866/E917	[163]	
4.87	Au+Au	0-5%		$2.21 \pm 0.03 \pm 0.33$	—	E866/E917	[163]	
4.87	Au+Au	0-5%	354	$2.24 \pm 0.05 \pm 0.34$	$4.14 \pm 0.09 \pm 0.62$	E802	[160]	
4.96	Au+Au	0-4%	363	—	$3.76 \pm 0.28 \pm 0.38$	E802	[161]	
6.27	Pb+Pb	0-7%	349	$5.58 \pm 0.07 \pm 0.11$	$10.3 \pm 0.1 \pm 0.2$	NA49	[126]	
7.62	Pb+Pb	0-7%	349	$7.8 \pm 0.1 \pm 0.2$	$16.0 \pm 0.2 \pm 0.4$	NA49	[126]	
8.73	Pb+Pb	0-7%	349	$7.58 \pm 0.12 \pm 0.4$	$19.2 \pm 0.5 \pm 1.0$	NA49	[125]	
9.2	Au+Au	0-10%	317	$8.7 \pm 2.0$ (sum)	—	STAR	[247]	
12.3	Pb+Pb	0-7%	349	$11.7 \pm 0.1 \pm 0.6$	$32.4 \pm 0.6 \pm 1.6$	NA49	[125]	
17.3	Pb+Pb	0-5%	362	$16.8 \pm 0.2 \pm 0.8$	$51.9 \pm 1.9 \pm 3.0$	NA49	[125]	
17.3	Pb+Pb	0-4%		$21.5 \pm 7.5$ (sum)	—	NA44	[248]	a)
17.3	Pb+Pb	0-3.7%		$15.4 \pm 0.5 \pm 1.0$	—	NA44	[175]	b)
62.4	Au+Au	0-10%		$28.6 \pm 0.8 \pm 2.3$	—	BRAHMS	[174]	c)
62.4	Au+Au	0-5%	347	$32.4 \pm 2.3$ (sum)	—	STAR	[122]	
130.0	Au+Au	0-6%	344	$42.7 \pm 2.8$ (sum)	—	STAR	[122]	
130.0	Au+Au	0-6%		$41.9 \pm 0.6 \pm 5.4$	—	STAR	[130]	
130.0	Au+Au	0-5%	348	$40.5 \pm 2.3 \pm 6.1$	—	PHENIX	[171]	
200.0	Au+Au	0-5%	351	$49.5 \pm 6.2$ (sum)	—	STAR	[122]	
200.0	Au+Au	0-5%	351	$45.7 \pm 5.2$	—	PHENIX	[128]	
200.0	Au+Au	0-10%	328	$40.9 \pm 0.63 \pm 6.13$	—	BRAHMS	[129]	
200.0	Au+Au	0-5%		—	$242.0 \pm 4.0 \pm 19.0$	BRAHMS	[166]	d)

Table 5: The rapidity densities  $dN/dy$  around midrapidity and the total multiplicities  $\langle N \rangle$  of  $K_S^0$  as measured in central nucleus-nucleus collisions at different  $\sqrt{s_{NN}}$ . Also listed are the centrality selection (Cent.) and the averaged number of participants ( $\langle N_{part} \rangle$ ). In most cases the statistical (first) and systematic (second) errors are given separately, while for a few measurements the quadratic sum of both is quoted (denoted by 'sum').

$\sqrt{s_{NN}}$ (GeV)	System	Cent.	$\langle N_{part} \rangle$	$dN/dy$	$\langle N \rangle$	Exp.	Ref.	Comnt.
17.3	Pb+Pb	0-4.5%		$26.0 \pm 1.7 \pm 2.6$	—	NA57	[204]	
17.3	Pb+Pb		351	$21.9 \pm 2.4$	—	WA97	[111, 250]	
130.0	Au+Au	0-6%		$33.9 \pm 1.1 \pm 5.1$	—	STAR	[130]	

Table 6: The rapidity densities  $dN/dy$  around midrapidity and the total multiplicities  $\langle N \rangle$  of  $\phi$  as measured in central nucleus-nucleus collisions at different  $\sqrt{s_{NN}}$ . Also listed are the centrality selection (Cent.) and the averaged number of participants ( $\langle N_{\text{part}} \rangle$ ). In most cases the statistical (first) and systematic (second) errors are given separately, while for a few measurements the quadratic sum of both is quoted (denoted by 'sum').

$\sqrt{s_{NN}}$ (GeV)	System	Cent.	$\langle N_{\text{part}} \rangle$	$dN/dy$	$\langle N \rangle$	Exp.	Ref.	Comnt.
4.87	Au+Au	0-5%	340	$0.362 \pm 0.065 \pm 0.054$	—	E917	[182]	
6.27	Pb+Pb	0-7%	349	$1.17 \pm 0.23 \pm 0.38$	$1.89 \pm 0.31 \pm 0.22$	NA49	[149]	
7.62	Pb+Pb	0-7%	349	$0.94 \pm 0.13 \pm 0.30$	$1.84 \pm 0.22 \pm 0.29$	NA49	[149]	
8.73	Pb+Pb	0-7%	349	$1.16 \pm 0.16 \pm 0.14$	$2.55 \pm 0.17 \pm 0.19$	NA49	[149]	
12.3	Pb+Pb	0-7%	349	$1.52 \pm 0.11 \pm 0.22$	$4.04 \pm 0.19 \pm 0.31$	NA49	[149]	
17.3	Pb+Pb	0-5%	362	$2.44 \pm 0.10 \pm 0.08$	$8.46 \pm 0.38 \pm 0.33$	NA49	[149]	
17.3	Pb+Pb	0-4%		$2.39 \pm 0.21$ (sum)	$7.6 \pm 1.1$ (sum)	NA49	[207]	
17.3	Pb+Au	0-7%		$2.05 \pm 0.14 \pm 0.25$	—	NA45	[181]	e)
17.3	Pb+Au	0-7%		$2.04 \pm 0.49 \pm 0.32$	—	NA45	[181]	f)
62.4	Au+Au	0-20%		$3.52 \pm 0.08 \pm 0.45$	—	STAR	[180]	
130.0	Au+Au	0-11%		$5.73 \pm 0.37 \pm 0.69$	—	STAR	[183]	
200.0	Au+Au	0-5%		$7.70 \pm 0.30 \pm 0.85$	—	STAR	[184]	
200.0	Au+Au	0-5%		$7.95 \pm 0.11 \pm 0.73$	—	STAR	[180]	
200.0	Au+Au	0-10%	325	$3.94 \pm 0.60 \pm 0.62$	—	PHENIX	[185]	

Table 7: The rapidity densities  $dN/dy$  around midrapidity and the total multiplicities  $\langle N \rangle$  of  $\Lambda$  as measured in central nucleus-nucleus collisions at different  $\sqrt{s_{NN}}$ . Also listed are the centrality selection (Cent.) and the averaged number of participants ( $\langle N_{\text{part}} \rangle$ ). In most cases the statistical (first) and systematic (second) errors are given separately, while for a few measurements the quadratic sum of both is quoted (denoted by 'sum').

$\sqrt{s_{NN}}$ (GeV)	System	Cent.	$\langle N_{\text{part}} \rangle$	$dN/dy$	$\langle N \rangle$	Exp.	Ref.	Comnt.
2.68	Au+Au	0-5%		$0.76 \pm 0.03$	$0.58 \pm 0.04$	E895	[249]	g)
3.32	Au+Au	0-5%		$3.6 \pm 0.1$	$5.5 \pm 0.3$	E895	[249]	g)
3.83	Au+Au	0-5%		$6.8 \pm 0.2$	$11.6 \pm 0.9$	E895	[249]	g)
3.83	Au+Au		342	—	$12.0 \pm 1.0$	E895	[131]	
4.29	Au+Au	0-5%		$10.25 \pm 0.3$	$16.0 \pm 1.0$	E895	[249]	g)
4.87	Au+Au	0-5%		$10.0 \pm 1.0$	—	E891	[143]	
4.87	Au+Au	0-5%			$16.7 \pm 0.5 \pm 1.7$	E896	[141]	
8.73	Pb+Pb	0-5%		$21.1 \pm 0.8 \pm 2.1$	—	NA57	[139]	
17.3	Pb+Pb	0-5%		$18.5 \pm 1.1 \pm 1.9$	—	NA57	[139]	
17.3	Pb+Pb	0-4.5%	349	$18.5 \pm 1.1 \pm 1.8$	—	NA57	[112]	
17.3	Pb+Pb		351	$13.7 \pm 0.9$	—	WA97	[111, 250]	
6.27	Pb+Pb	0-7%	349	$13.4 \pm 0.1 \pm 1.1$	$27.1 \pm 0.2 \pm 2.2$	NA49	[58]	
7.62	Pb+Pb	0-7%	349	$14.7 \pm 0.2 \pm 1.2$	$36.9 \pm 0.3 \pm 3.3$	NA49	[58]	
8.73	Pb+Pb	0-7%	349	$14.6 \pm 0.2 \pm 1.2$	$43.1 \pm 0.4 \pm 4.3$	NA49	[58]	
8.73	Pb+Pb	0-7%	349	$15.3 \pm 0.6 \pm 1.0$	$45.6 \pm 1.9 \pm 3.4$	NA49	[251]	h)
12.3	Pb+Pb	0-7%	349	$12.9 \pm 0.2 \pm 1.0$	$50.1 \pm 0.6 \pm 5.5$	NA49	[58]	
12.3	Pb+Pb	0-7%	349	$13.5 \pm 0.7 \pm 1.0$	$47.4 \pm 2.8 \pm 3.5$	NA49	[251]	h)
17.3	Pb+Pb	0-10%	335	$9.5 \pm 0.1 \pm 1.0$	$44.9 \pm 0.6 \pm 8.0$	NA49	[58]	
17.3	Pb+Pb	0-10%	335	$10.9 \pm 1.0 \pm 1.3$	$44.1 \pm 3.2 \pm 5.0$	NA49	[251]	h)
130.0	Au+Au	0-5%		$17.3 \pm 1.8 \pm 2.8$	—	PHENIX	[134]	
130.0	Au+Au	0-5%		$17.0 \pm 0.4 \pm 1.7$	—	STAR	[145]	c)
200.0	Au+Au	0-5%	352	$16.7 \pm 0.2 \pm 1.1$	—	STAR	[133]	c)

Table 8: The rapidity densities  $dN/dy$  around midrapidity and the total multiplicities  $\langle N \rangle$  of  $\bar{\Lambda}$  as measured in central nucleus-nucleus collisions at different  $\sqrt{s_{\text{NN}}}$ . Also listed are the centrality selection (Cent.) and the averaged number of participants ( $\langle N_{\text{part}} \rangle$ ). In most cases the statistical (first) and systematic (second) errors are given separately, while for a few measurements the quadratic sum of both is quoted (denoted by 'sum').

$\sqrt{s_{\text{NN}}}$ (GeV)	System	Cent.	$\langle N_{\text{part}} \rangle$	$dN/dy$	$\langle N \rangle$	Exp.	Ref.	Comnt.
4.87	Au+Au	0-12%		$0.019^{+0.004+0.003}_{-0.005-0.002}$	—	E917	[142]	
8.73	Pb+Pb	0-5%		$0.44 \pm 0.03 \pm 0.04$	—	NA57	[139]	
17.3	Pb+Pb	0-5%		$2.47 \pm 0.14 \pm 0.25$	—	NA57	[139]	
17.3	Pb+Pb	0-4.5%	349	$2.44 \pm 0.14 \pm 0.24$	—	NA57	[112]	
17.3	Pb+Pb		351	$1.8 \pm 0.2$	—	WA97	[111, 250]	
6.27	Pb+Pb	0-7%	349	$0.10 \pm 0.02 \pm 0.01$	$0.16 \pm 0.02 \pm 0.03$	NA49	[58]	
7.62	Pb+Pb	0-7%	349	$0.21 \pm 0.02 \pm 0.02$	$0.39 \pm 0.02 \pm 0.04$	NA49	[58]	
8.73	Pb+Pb	0-7%	349	$0.33 \pm 0.02 \pm 0.03$	$0.68 \pm 0.03 \pm 0.07$	NA49	[58]	
8.73	Pb+Pb	0-7%	349	$0.42 \pm 0.04 \pm 0.04$	$0.74 \pm 0.04 \pm 0.06$	NA49	[251]	h)
12.3	Pb+Pb	0-7%	349	$0.82 \pm 0.03 \pm 0.08$	$1.82 \pm 0.06 \pm 0.19$	NA49	[58]	
12.3	Pb+Pb	0-7%	349	$1.06 \pm 0.08 \pm 0.10$	$2.26 \pm 0.25 \pm 0.20$	NA49	[251]	h)
17.3	Pb+Pb	0-10%	335	$1.24 \pm 0.03 \pm 0.13$	$3.07 \pm 0.06 \pm 0.31$	NA49	[58]	
17.3	Pb+Pb	0-10%	335	$1.62 \pm 0.16 \pm 0.2$	$3.87 \pm 0.18 \pm 0.40$	NA49	[251]	h)
130.0	Au+Au	0-5%		$12.7 \pm 1.8 \pm 2.0$	—	PHENIX	[134]	
130.0	Au+Au	0-5%		$12.3 \pm 0.3 \pm 1.2$	—	STAR	[145]	
200.0	Au+Au	0-5%	352	$12.7 \pm 0.2 \pm 0.9$	—	STAR	[133]	

Table 9: The rapidity densities  $dN/dy$  around midrapidity and the total multiplicities  $\langle N \rangle$  of  $\Xi^-$  as measured in central nucleus-nucleus collisions at different  $\sqrt{s_{NN}}$ . Also listed are the centrality selection (Cent.) and the averaged number of participants ( $\langle N_{\text{part}} \rangle$ ). In most cases the statistical (first) and systematic (second) errors are given separately, while for a few measurements the quadratic sum of both is quoted (denoted by 'sum').

$\sqrt{s_{NN}}$ (GeV)	System	Cent.	$\langle N_{\text{part}} \rangle$	$dN/dy$	$\langle N \rangle$	Exp.	Ref.	Comnt.
3.83	Au+Au		342	—	$0.17 \pm 0.05$	E895	[131]	
8.73	Pb+Pb	0-10%		$1.84 \pm 0.16 \pm 0.18$	—	NA57	[139]	
17.3	Pb+Pb	0-10%		$1.91 \pm 0.05 \pm 0.19$	—	NA57	[139]	
17.3	Pb+Pb	0-4.5%	349	$2.08 \pm 0.09 \pm 0.21$	—	NA57	[112]	
17.3	Pb+Pb		351	$1.5 \pm 0.1$	—	WA97	[111, 250]	
6.27	Pb+Pb	0-7%	349	$0.93 \pm 0.13 \pm 0.10$	$1.50 \pm 0.13 \pm 0.17$	NA49	[58]	
7.62	Pb+Pb	0-7%	349	$1.17 \pm 0.13 \pm 0.13$	$2.42 \pm 0.19 \pm 0.29$	NA49	[58]	
8.73	Pb+Pb	0-7%	349	$1.15 \pm 0.11 \pm 0.13$	$2.96 \pm 0.20 \pm 0.36$	NA49	[58]	
12.3	Pb+Pb	0-7%	349	$1.22 \pm 0.14 \pm 0.13$	$3.80 \pm 0.26 \pm 0.61$	NA49	[58]	
17.3	Pb+Pb	0-10%	335	$1.44 \pm 0.10 \pm 0.15$	$4.04 \pm 0.16 \pm 0.57$	NA49	[58]	
17.3	Pb+Pb	0-10%	335	$1.49 \pm 0.08 \pm 0.22$	$4.12 \pm 0.20 \pm 0.62$	NA49	[189]	
130.0	Au+Au	0-10%		$2.00 \pm 0.14 \pm 0.20$	—	STAR	[132]	c)
200.0	Au+Au	0-5%	352	$2.17 \pm 0.06 \pm 0.19$	—	STAR	[133]	

Table 10: The rapidity densities  $dN/dy$  around midrapidity and the total multiplicities  $\langle N \rangle$  of  $\Xi^+$  as measured in central nucleus-nucleus collisions at different  $\sqrt{s_{NN}}$ . Also listed are the centrality selection (Cent.) and the averaged number of participants ( $\langle N_{\text{part}} \rangle$ ). In most cases the statistical (first) and systematic (second) errors are given separately, while for a few measurements the quadratic sum of both is quoted (denoted by 'sum').

$\sqrt{s_{NN}}$ (GeV)	System	Cent.	$\langle N_{\text{part}} \rangle$	$dN/dy$	$\langle N \rangle$	Exp.	Ref.	Comnt.
8.73	Pb+Pb	0-10%		$0.068 \pm 0.021 \pm 0.007$	—	NA57	[139]	
17.3	Pb+Pb	0-10%		$0.422 \pm 0.023 \pm 0.042$	—	NA57	[139]	
17.3	Pb+Pb	0-4.5%	349	$0.51 \pm 0.04 \pm 0.05$	—	NA57	[112]	
17.3	Pb+Pb		351	$0.37 \pm 0.06$	—	WA97	[111, 250]	
7.62	Pb+Pb	0-7%	349	$0.05 \pm 0.01 \pm 0.01$	$0.12 \pm 0.02 \pm 0.03$	NA49	[58]	
8.73	Pb+Pb	0-7%	349	$0.07 \pm 0.01 \pm 0.01$	$0.13 \pm 0.01 \pm 0.02$	NA49	[58]	
12.3	Pb+Pb	0-7%	349	$0.21 \pm 0.03 \pm 0.02$	$0.58 \pm 0.06 \pm 0.13$	NA49	[58]	
17.3	Pb+Pb	0-10%	335	$0.31 \pm 0.03 \pm 0.03$	$0.66 \pm 0.04 \pm 0.08$	NA49	[58]	
17.3	Pb+Pb	0-10%	335	$0.33 \pm 0.04 \pm 0.05$	$0.77 \pm 0.04 \pm 0.12$	NA49	[189]	
130.0	Au+Au	0-10%		$1.70 \pm 0.12 \pm 0.17$	—	STAR	[132]	c)
200.0	Au+Au	0-5%	352	$1.83 \pm 0.05 \pm 0.20$	—	STAR	[133]	

Table 11: The rapidity densities  $dN/dy$  around midrapidity and the total multiplicities  $\langle N \rangle$  of  $\Omega^- + \bar{\Omega}^+$  as measured in central nucleus-nucleus collisions at different  $\sqrt{s_{NN}}$ . Also listed are the centrality selection (Cent.) and the averaged number of participants ( $\langle N_{\text{part}} \rangle$ ). In most cases the statistical (first) and systematic (second) errors are given separately, while for a few measurements the quadratic sum of both is quoted (denoted by 'sum').

$\sqrt{s_{NN}}$ (GeV)	System	Cent.	$\langle N_{\text{part}} \rangle$	Particle	$dN/dy$	$\langle N \rangle$	Exp.	Ref.	Comnt.
8.73	Pb+Pb	0-11%		$\Omega^-$	$0.085 \pm 0.046 \pm 0.009$	—	NA57	[139]	
8.73	Pb+Pb	0-11%		$\bar{\Omega}^+$	$0.035 \pm 0.020 \pm 0.004$	—	NA57	[139]	
17.3	Pb+Pb	0-11%		$\Omega^-$	$0.259 \pm 0.037 \pm 0.026$	—	NA57	[139]	
17.3	Pb+Pb	0-11%		$\bar{\Omega}^+$	$0.129 \pm 0.022 \pm 0.013$	—	NA57	[139]	
17.3	Pb+Pb	0-4.5%	349	$\Omega^-$	$0.31 \pm 0.07 \pm 0.05$	—	NA57	[112]	
17.3	Pb+Pb	0-4.5%	349	$\bar{\Omega}^+$	$0.16 \pm 0.04 \pm 0.02$	—	NA57	[112]	
17.3	Pb+Pb		351	$\Omega^- + \bar{\Omega}^+$	$0.41 \pm 0.08$	—	WA97	[111, 250]	
8.73	Pb+Pb	0-7%	349	$\Omega^- + \bar{\Omega}^+$	$0.10 \pm 0.02 \pm 0.02$	$0.14 \pm 0.03 \pm 0.04$	NA49	[59]	
17.3	Pb+Pb	0-23.5%	262	$\Omega^-$	$0.14 \pm 0.03 \pm 0.01$	$0.43 \pm 0.09 \pm 0.03$	NA49	[59]	
17.3	Pb+Pb	0-23.5%	262	$\bar{\Omega}^+$	$0.07 \pm 0.02 \pm 0.01$	$0.19 \pm 0.04 \pm 0.02$	NA49	[59]	
130.0	Au+Au	0-10%		$\Omega^- + \bar{\Omega}^+$	$0.55 \pm 0.11 \pm 0.06$	—	STAR	[132]	c)
200.0	Au+Au	0-5%	352	$\Omega^- + \bar{\Omega}^+$	$0.53 \pm 0.04 \pm 0.04$	—	STAR	[133]	

## Comments

- a) Measured in the rapidity range  $2.7 < y < 2.9$ .
- b) Measured in the rapidity range  $2.4 < y < 3.5$ .
- c) The  $dN/dy$  value is based on the  $p_t$  extrapolation using the Boltzmann function.
- d) The value of the total multiplicity is based on the extrapolation using the single Gaussian.
- e) Measured in the rapidity range  $2.0 < y < 2.4$ .
- f) Measured via the decay channel  $\phi \rightarrow e^+ + e^-$  in the rapidity range  $2.1 < y < 2.65$ .
- g) Preliminary data only, shown on Quark Matter 2001 conference [249].
- h) Data in [251] are not corrected for feed-down from weak decays and are therefore superseded by the values given in [58].



## List of Variables

$A$	: Atomic weight
$b$	: Impact parameter
$c$	: Velocity of light
$\beta$	: $v/c$
$\beta_s$	: Surface velocity
$\beta_\perp$	: Transverse expansion velocity
$c\tau$	: Lifetime
$dE/dx$	: Specific energy loss
$dN/dy$	: Rapidity density
$E_S$	: Strangeness enhancement factor
$\langle E \rangle / \langle N \rangle$	: Energy density / particle density
$\gamma$	: Lorentz factor
$\gamma_s$	: Strange quark fugacity
$\gamma_q$	: Fugacity for quark flavor $q$
$\epsilon_{\text{part}}$	: Participant eccentricity
$I$	: Isospin
$J$	: Spin
$\kappa$	: String tension
$\lambda_S$	: Wroblewski factor
$m$	: Mass
$m_e$	: Electron mass
$m_P$	: Proton mass
$m_s$	: Strange quark mass
$m_t$	: Transverse mass
$\mu_B$	: Baryo-chemical potential
$N$	: Multiplicity
$N_{\text{bin}}$	: Number of binary collisions
$N_{\text{light}}$	: Number of light ( $u, d$ ) quarks in a hadron
$N_{\text{part}}, N_P$	: Number of participants
$N_q$	: Number of quarks of type $q$ in a hadron
$N_{\text{PC}}$	: Number of corona participants
$N_s$	: Number of strange quarks in a hadron
$n_B$	: Baryon density
$n_s$	: Number density of (anti-)strange quarks
$P$	: Parity
$p_t, p_\perp$	: Transverse momentum
$p$	: Total momentum
$Q$	: $Q$ -value of a given reaction

$R$	: Anti-baryon-baryon ratio
$R_{AA}$	: Nuclear suppression factor
$R_{CP}$	: Nuclear suppression factor
$R_s$	: Fireball radius
$RMS_y$	: RMS width of rapidity distribution
$r$	: Radius parameter
$\rho$	: Boost angle $\rho = \tanh^{-1} \beta_{\perp}$
$s$	: Entropy density
$S$	: Strangeness
$\sigma_i$	: Width of rapidity distribution of particle type $i$ (Gauss)
$\sigma_{\text{inel}}^{\text{NN}}$	: Inelastic nucleon-nucleon cross section
$\sqrt{s_{\text{coll}}}$	: Center-of-mass energy of a binary collision
$\sqrt{s_{\text{NN}}}$	: Center-of-mass energy in nucleon-nucleon system
$T$	: Temperature
$T_{\text{ch}}$	: Chemical freeze-out temperature
$T_{\text{fo}}$	: Thermal freeze-out temperature
$T_C$	: Critical temperature
$T_{\text{max}}$	: Maximum kinetic energy transfer
$T^*$	: Inverse slope parameter
$\tau^{\text{eq}}$	: Equilibration time
$\tau_{\text{fo}}$	: Decoupling times in hydro freeze-out
$V$	: Volume
$v_s$	: Surface velocity
$v_{\perp}$	: Transverse expansion velocity
$v_2$	: Elliptic flow coefficient
$Y$	: Yield
$Y_{\text{core}}$	: Yield in core
$Y_{\text{corona}}$	: Yield in corona
$y$	: Rapidity
$y_{\text{beam}}$	: Beam rapidity
$Z$	: Atomic charge
$z$	: Particle charge

# References

- [1] Y. Aoki et al., *JHEP* 06 (2009) 088.
- [2] A. Bazavov et al., *Phys. Rev. D* 80 (2009) 014504.
- [3] Z. Fodor and S.D. Katz, *JHEP* 04 (2004) 050.
- [4] C.R. Allton et al., *Phys. Rev. D* 66 (2002) 074507.
- [5] Y. Hatta and T. Ikeda, *Phys. Rev. D* 67 (2003) 014028.
- [6] P. de Forcrand and O. Philipsen, *JHEP* 01 (2007) 077.
- [7] J. Rafelski and B. Müller, *Phys. Rev. Lett.* 48 (1982) 1066.
- [8] P. Koch, J. Rafelski, and W. Greiner, *Phys. Lett. B* 123 (1983) 151.
- [9] P. Koch, B. Müller, and J. Rafelski, *Phys. Rep.* 142 (1986) 167.
- [10] K. Nakamura et al. (Particle Data Group), *J. Phys. G* 37 (2010) 075021.
- [11] J. Rafelski and J. Letessier, *J. Phys. G* 30 (2004) S1.
- [12] J. Rafelski, J. Letessier and A. Tounsi, *Acta Phys. Pol. B* 27 (1996) 1037.
- [13] J. Schaffner-Bielich, *J. Phys. G* 30 (2004) R245.
- [14] I. Arsene et al. (BRAHMS Collaboration), *Nucl. Phys. A* 757 (2005) 1.
- [15] B.B. Back et al. (PHOBOS Collaboration), *Nucl. Phys. A* 757 (2005) 28.
- [16] J. Adams et al. (STAR Collaboration), *Nucl. Phys. A* 757 (2005) 102.
- [17] K. Adcox et al. (PHENIX Collaboration), *Nucl. Phys. A* 757 (2005) 184.
- [18] E.V. Shuryak and I. Zahed, *Phys. Rev. D* 70 (2004) 054507.
- [19] S. Datta, F. Karsch, P. Petreczky, and I. Wetzorke, *Nucl. Phys. B (Proc. Suppl.)* 119 (2003) 487.
- [20] M. Asakawa and T. Hatsuda, *Phys. Rev. Lett.* 92 (2004) 012001.
- [21] J.O. Andersen and M. Strickland, *Ann. Phys.* 317 (2005) 281.
- [22] W. Greiner and D.H. Rischke, *Phys. Rep.* 264 (1996) 183.
- [23] T.S. Biró, P. Lévai, and B. Müller, *Phys. Rev. D* 42 (1990) 3078.
- [24] T. Altherr and D. Seibert, *Phys. Rev. C* 49 (1994) 1684.
- [25] N. Bilić, J. Cleymans, I. Dadić, and D. Hislop, *Phys. Rev. C* 52 (1995) 401.
- [26] Z. Xu and C. Greiner, *Phys. Rev. C* 71 (2005) 064901.
- [27] S. Mrówczyński, *Acta Phys. Pol. B* 37 (2006) 427.
- [28] K.P. Das and R. Hwa, *Phys. Lett. B* 68 (1977) 459.
- [29] R.J. Fries, B. Müller, C. Nonaka, and S.A. Bass, *Phys. Rev. C* 68 (2003) 044902.
- [30] V. Greco, C.M. Ko, and P. Lévai, *Phys. Rev. C* 68 (2003) 034904.
- [31] J.H. Chen et al., *Phys. Rev. C* 78 (2008) 034907
- [32] B. Müller, R.J. Fries, and S.A. Bass, *Phys. Lett. B* 618 (2005) 77
- [33] R. Hwa and C.B. Yang, *arXiv:nucl-th/0602024* and *Phys. Rev. C* 75 (2007) 054904.
- [34] C. Greiner and S. Leupold, *J. Phys. G* 27 (2001) L95.
- [35] J. Kapusta and I. Shovkovy, *Phys. Rev. C* 68 (2003) 014901.
- [36] P. Huovinen and J. Kapusta, *Phys. Rev. C* 69 (2004) 014902.
- [37] P. Braun-Munzinger, J. Stachel, and C. Wetterich, *Phys. Lett. B* 596 (2004) 61.
- [38] J. Noronha-Hostler, C. Greiner, and I.A. Shovkovy, *Phys. Rev. Lett.* 100 (2008) 252301.
- [39] J. Noronha-Hostler, H. Ahmad, J. Noronha, and C. Greiner, *Phys. Rev. C* 82 (2010) 024913.

- [40] R. Hagedorn, *Nuovo Cimento Suppl.* 6 (1968) 311.
- [41] R. Hagedorn, *Nuovo Cimento Suppl.* 3 (1965) 147.
- [42] U. Heinz, *Nucl. Phys. A* 661 (1999) 140c.
- [43] R. Stock, *Phys. Lett. B* 456 (1999) 277.
- [44] F. Becattini and U. Heinz, *Z. Phys. C* 76 (1997) 269.
- [45] D. Zschesche, S. Schramm, J. Schaffner-Bielich, H. Stöcker, and W. Greiner, *Phys. Lett. B* 547 (2002) 7.
- [46] M. Bleicher et al., *J. Phys. G* 25 (1999) 1859.
- [47] S.A. Bass et al., *Prog. Part. Nucl. Phys.* 41 (1998) 225.
- [48] H. Sorge, H. Stöcker, and W. Greiner, *Nucl. Phys. A* 498 (1989) 567c.
- [49] W. Cassing and E.L. Bratkovskaya, *Phys. Rep.* 308 (1999) 65.
- [50] B. Zhang, C.M. Ko, B.-A. Li, and Z. Lin, *Phys. Rev. C* 61 (2000) 067901.
- [51] K. Werner, F.-M. Liu, and T. Pierog, *Phys. Rev. C* 74 (2006) 044902.
- [52] H. Petersen, M. Bleicher, S.A. Bass, and H. Stöcker, *arXiv:0805.0567*.
- [53] T. Sjöstrand, S. Mrenna, and P. Skands, *JHEP* 05 (2006) 026.
- [54] B. Andersson, G. Gustafson, and H. Pi, *Z. Phys. C* 57 (1993) 485.
- [55] E.L. Bratkovskaya et al., *Phys. Rev. C* 69 (2004) 054907.
- [56] W. Cassing and E.L. Bratkovskaya, *Nucl. Phys. A* 831 (2009) 215.
- [57] H. Petersen, M. Mitrovski, T. Schuster, and M. Bleicher, *Phys. Rev. C* 80 (2009) 054910.
- [58] C. Alt. et al. (NA49 Collaboration), *Phys. Rev. C* 78 (2008) 034918.
- [59] C. Alt et al. (NA49 Collaboration), *Phys. Rev. Lett.* 94 (2005) 192301.
- [60] S. Soff et al., *Phys. Lett. B* 471 (1999) 89.
- [61] F. Antinori et al. (WA97 Collaboration), *Eur. Phys. J. C* 11 (1999) 79.
- [62] T. Anticic et al. (NA49 Collaboration), *Phys. Rev. C* 80 (2009) 034906.
- [63] H. Weber, E.L. Bratkovskaya, W. Cassing, and H. Stöcker, *Phys. Rev. C* 67 (2003) 014904.
- [64] W. Cassing and E.L. Bratkovskaya, *Phys. Rev. C* 78 (2008) 034919.
- [65] F. Becattini, M. Gaździcki, and J. Sollfrank, *Eur. Phys. J. C* 5 (1998) 143.
- [66] P. Braun-Munzinger, I. Heppe, and J. Stachel, *Phys. Lett. B* 465 (1999) 15.
- [67] S. Wheaton, J. Cleymans, and M. Hauer, *Comp. Phys. Comm.* 180 (2009) 84.
- [68] G. Torrieri et al, *Comp. Phys. Comm.* 167 (2005) 229.
- [69] A. Kisiel, T. Tałuć, W. Broniowski, and W. Florkowski, *Comp. Phys. Comm.* 174 (2006) 669.
- [70] F. Becattini, J. Cleymans, A. Keränen, E. Suhonen, and K. Redlich, *Phys. Rev. C* 64 (2001) 024901.
- [71] J. Sollfrank, *J. Phys. G* 23 (1997) 1903.
- [72] J. Cleymans and K. Redlich, *Phys. Rev. C* 60 (1999) 054908.
- [73] J. Letessier and J. Rafelski, *Phys. Rev. C* 59 (1999) 947.
- [74] J. Letessier and J. Rafelski, *Eur. Phys. J. A* 35 (2008) 221.
- [75] A. Andronic, P. Braun-Munzinger, and J. Stachel, *Nucl. Phys. A* 772 (2006) 167.
- [76] F. Becattini, M. Gaździcki, A. Keränen, J. Manninen, and R. Stock, *Phys. Rev. C* 69 (2004) 024905.
- [77] A. Andronic, P. Braun-Munzinger, and J. Stachel, *Phys. Lett. B* 673 (2009) 142.
- [78] F. Becattini, J. Manninen, and M. Gaździcki, *Phys. Rev. C* 73 (2006) 044905.
- [79] M. Bleicher and J. Aichelin, *Phys. Lett. B* 530 (2002) 81.

- [80] B.I. Abelev et al. (STAR collaboration), *Phys. Rev. Lett.* 97 (2006) 132301.
- [81] C. Markert, G. Torrieri, and J. Rafelski, Proceedings of PASI 2002, *arXiv:hep-ph/0206260*.
- [82] P. Braun-Munzinger, J. Cleymans, H. Oeschler, and K. Redlich, *Nucl. Phys. A* 697 (2002) 902.
- [83] P. Braun-Munzinger and J. Stachel, *J. Phys. G* 28 (2002) 1971.
- [84] J. Cleymans, H. Oeschler, K. Redlich, and S. Wheaton, *Phys. Lett. B* 615 (2005) 50.
- [85] A. Tawfik, *J. Phys. G* 31 (2005) S1105.
- [86] F. Becattini and L. Ferroni, *Eur. Phys. J. C* 35 (2004) 243.
- [87] I. Kraus, J. Cleymans, H. Oeschler, K. Redlich, and S. Wheaton, *Phys. Rev. C* 76 (2007) 064903.
- [88] J. Cleymans, H. Oeschler, K. Redlich, and S. Wheaton, *J. Phys. G* 32 (2006) S165.
- [89] J. Rafelski and M. Danos, *Phys. Lett. B* 97 (1980) 279.
- [90] S. Hamieh, K. Redlich, and A. Tounsi, *Phys. Lett. B* 486 (2000) 61.
- [91] T. Abbott et al. (E802 Collaboration), *Phys. Rev. Lett.* 64 (1990) 847.
- [92] T. Abbott et al. (E802 Collaboration), *Phys. Rev. Lett.* 66 (1991) 1567.
- [93] T. Abbott et al. (E802 Collaboration), *Phys. Lett. B* 291 (1992) 341.
- [94] S.E. Eiseman et al. (E810 Collaboration), *Phys. Lett. B* 248 (1990) 254.
- [95] S.E. Eiseman et al. (E810 Collaboration), *Phys. Lett. B* 297 (1992) 44.
- [96] S. Abatzis et al. (WA85 Collaboration), *Phys. Lett. B* 244 (1990) 130.
- [97] A. Bamberger et al. (NA35 Collaboration), *Z. Phys. C* 43 (1989) 25.
- [98] J. Bartke et al. (NA35 Collaboration), *Z. Phys. C* 48 (1990) 191.
- [99] E. Anderson et al. (NA36 Collaboration), *Phys. Lett. B* 294 (1992) 127.
- [100] T. Alber et al. (NA35 Collaboration), *Z. Phys. C* 64 (1994) 195.
- [101] F. Wang, H. Liu, H. Sorge, N. Xu, and J. Yang, *Phys. Rev. C* 61 (2000) 064904.
- [102] S. Abatzis et al. (WA85 Collaboration), *Phys. Lett. B* 259 (1991) 508.
- [103] S. Abatzis et al. (WA85 Collaboration), *Phys. Lett. B* 270 (1991) 123.
- [104] S. Abatzis et al. (WA85 Collaboration), *Phys. Lett. B* 316 (1993) 615.
- [105] S. Abatzis et al. (WA85 Collaboration), *Phys. Lett. B* 347 (1995) 158.
- [106] S. Abatzis et al. (WA85 Collaboration), *Phys. Lett. B* 359 (1995) 382.
- [107] S. Abatzis et al. (WA85 Collaboration), *Phys. Lett. B* 393 (1997) 210.
- [108] S. Abatzis et al. (WA85 Collaboration), *Phys. Lett. B* 447 (1999) 178.
- [109] S. Abatzis et al. (WA94 Collaboration), *Phys. Lett. B* 354 (1995) 178.
- [110] S. Abatzis et al. (WA94 Collaboration), *Phys. Lett. B* 400 (1997) 239.
- [111] E. Andersen et al. (WA97 Collaboration), *Phys. Lett. B* 449 (1999) 401.
- [112] F. Antinori et al. (NA57 Collaboration), *J. Phys. G* 32 (2006) 427.
- [113] C. Blume et al. (for the NA49 Collaboration), *J. Phys. G* 35 (2008) 044004.
- [114] S. Margetis, K. Šafařík, and O. Villalobos Bailie, *Annu. Rev. Nucl. Part. Sci.* 50 (2000) 299.
- [115] R.J. Glauber, *Phys. Rev.* 100 (1955) 242.
- [116] M.L. Miller, K. Reygers, S.J. Sanders, and P. Steinberg, *Annu. Rev. Nucl. Part. Sci.* 57 (2007) 205.
- [117] G. Torrieri, *J. Phys. G* 36 (2009) 064007.
- [118] M. Mitrovski et al. (for the NA49 Collaboration), *J. Phys. G* 37 (2010) 094003.
- [119] B.I. Abelev et al. (STAR Collaboration), *Phys. Rev. C* 77 (2008) 044908.

- [120] T. Susa et al. (for the NA49 Collaboration), *Nucl. Phys. A* 698 (2002) 491c.
- [121] I. Chemakin et al. (E910 Collaboration), *Phys. Rev. Lett.* 85 (2000) 4868.
- [122] B.I. Abelev et al. (STAR Collaboration), *Phys. Rev. C* 79 (2009) 034909.
- [123] S.V. Afanasiev et al. (NA49 Collaboration), *Nucl. Instrum. Meth. Phys. Sect. A* 430 (1999) 210.
- [124] M. Anderson et al. (STAR Collaboration), *Nucl. Instrum. Meth. Phys. Sect. A* 499 (2003) 659.
- [125] S. Afanasiev et al. (NA49 Collaboration), *Phys. Rev. C* 66 (2002) 054902.
- [126] C. Alt et al. (NA49 Collaboration), *Phys. Rev. C* 77 (2008) 024903.
- [127] K. Adcox et al. (PHENIX Collaboration), *Phys. Rev. C* 69 (2004) 024904.
- [128] S.S. Adler et al. (PHENIX Collaboration), *Phys. Rev. C* 69 (2004) 034909.
- [129] I. Arsene et al. (BRAHMS Collaboration), *Phys. Rev. C* 72 (2005) 014908.
- [130] C. Adler et al. (STAR Collaboration), *Phys. Lett. B* 595 (2004) 143.
- [131] P. Chung et al. (E895 Collaboration), *Phys. Rev. Lett.* 91 (2003) 202301.
- [132] J. Adams et al. (STAR Collaboration), *Phys. Rev. Lett.* 92 (2004) 182301.
- [133] J. Adams et al. (STAR Collaboration), *Phys. Rev. Lett.* 98 (2007) 062301.
- [134] K. Adcox et al. (PHENIX Collaboration), *Phys. Rev. Lett.* 89 (2002) 092302.
- [135] B. Alessandro et al. (ALICE Collaboration), *J. Phys. G* 32 (2006) 1295.
- [136] S. Radomski (for the NA45 Collaboration), *J. Phys. G* 35 (2008) 044003.
- [137] C. Alt et al. (NA49 Collaboration), *Phys. Rev. C* 73 (2006) 044910.
- [138] M. Kaneta et al. (NA44 Collaboration), *J. Phys. G* 23 (1997) 1865.
- [139] F. Antinori et al. (NA57 Collaboration), *Phys. Lett. B* 595 (2004) 68.
- [140] L. Ahle et al. (E802 Collaboration), *Phys. Rev. Lett.* 81 (1998) 2650.
- [141] S. Albergo et al. (E896 Collaboration), *Phys. Rev. Lett.* 88 (2002) 062301.
- [142] B.B. Back et al. (E917 Collaboration), *Phys. Rev. Lett.* 87 (2001) 242301.
- [143] S. Ahmad et al. (E891 Collaboration), *Phys. Lett. B* 382 (1996) 35.
- [144] C. Adler et al. (STAR Collaboration), *Phys. Rev. Lett.* 86 (2001) 4778.
- [145] C. Adler et al. (STAR Collaboration), *Phys. Rev. Lett.* 89 (2002) 092301.
- [146] J. Adams et al. (STAR Collaboration), *Phys. Rev. Lett.* 92 (2004) 112301.
- [147] C. Alt et al. (NA49 Collaboration), *Eur. Phys. J. C* 45 (2006) 343.
- [148] C. Alt et al. (NA49 Collaboration), *Phys. Rev. Lett.* 94 (2005) 052301.
- [149] C. Alt et al. (NA49 Collaboration), *Phys. Rev. C* 78 (2008) 044907.
- [150] B.I. Abelev et al. (STAR Collaboration), *Phys. Lett. B* 673 (2009) 183.
- [151] M. Gaździcki and D. Röhrich, *Z. Phys. C* 71 (1996) 55.
- [152] J.C. Dunlop and C.A. Ogilvie, *Phys. Rev. C* 61 (2000) 031901(R), Erratum-ibid. *Phys. Rev. C* 64 (2001) 019901(E).
- [153] G. Agakishiev et al. (HADES Collaboration), *Phys. Rev. Lett.* 103 (2009) 132301.
- [154] A. Andronic, P. Braun-Munzinger, and K. Redlich, *Nucl. Phys. A* 765 (2006) 211.
- [155] F. Antinori et al. (NA57 Collaboration), *J. Phys. G* 37 (2010) 045105.
- [156] B.I. Abelev et al. (STAR Collaboration), *Phys. Rev. C* 75 (2007) 064901.
- [157] F. Becattini and J. Manninen, *J. Phys. G* 35 (2008) 104013.
- [158] A.K. Wróblewski, *Acta Phys. Pol. B* 16 (1985) 379.
- [159] L. Ahle et al. (E802 Collaboration), *Phys. Rev. C* 57 (1998) R466.

- [160] L. Ahle et al. (E802 Collaboration), *Phys. Rev. C* 58 (1998) 3523.
- [161] L. Ahle et al. (E802 Collaboration), *Phys. Rev. C* 60 (1999) 044904.
- [162] L. Ahle et al. (E866 and E917 Collaboration), *Phys. Lett. B* 476 (2000) 1.
- [163] L. Ahle et al. (E866 and E917 Collaboration), *Phys. Lett. B* 490 (2000) 53.
- [164] J. Barette et al. (E877 Collaboration), *Phys. Rev. C* 62 (2000) 024901.
- [165] J. Klay et al. (E895 Collaboration), *Phys. Rev. C* 68 (2003) 054905.
- [166] I.G. Bearden et al. (BRAHMS Collaboration), *Phys. Rev. Lett.* 94 (2005) 162301.
- [167] M. Gaździcki and D. Röhrich, *Z. Phys. C* 65 (1995) 215.
- [168] W. Cassing, E.L. Bratkovskaya, and S. Juchem, *Nucl. Phys. A* 674 (2000) 249.
- [169] M. Gaździcki, M.I. Gorenstein, and P. Seyboth, *Acta Phys. Pol. B* 42 (2011) 307.
- [170] M. Gaździcki and M.I. Gorenstein, *Acta Phys. Pol. B* 30 (1999) 2705.
- [171] K. Adcox et al. (PHENIX Collaboration), *Phys. Rev. Lett.* 88 (2002) 242301.
- [172] U. Heinz, J. Sollfrank, H. Sorge, and N. Xu, *Phys. Rev. C* 59 (1999) 1637.
- [173] R. Hagedorn, *CERN-TH-4100/85* (1985).
- [174] I.C. Arsene et al. (BRAHMS Collaboration), *Phys. Lett. B* 687 (2010) 36.
- [175] I.G. Bearden et al. (NA44 Collaboration), *Phys. Rev. C* 66 (2002) 044907.
- [176] Z.-W. Lin, S. Pal, C.M. Ko, B.-A. Li, and B. Zhang, *Nucl. Phys. A* 698 (2002) 375c.
- [177] J. Cleymans, H. Oeschler, K. Redlich, and S. Wheaton, *Eur. Phys. J. A* 29 (2006) 119.
- [178] P. Braun-Munzinger, J. Stachel, J.P. Wessels, and N. Xu, *Phys. Lett. B* 365 (1996) 1.
- [179] F. Becattini and J. Cleymans, *J. Phys. G* 34 (2007) S959.
- [180] B.I. Abelev et al. (STAR Collaboration), *Phys. Rev. C* 79 (2009) 064903.
- [181] D. Adamová et al. (NA45 Collaboration), *Phys. Rev. Lett.* 96 (2006) 152301.
- [182] B.B. Back et al. (E917 Collaboration), *Phys. Rev. C* 69 (2004) 054901.
- [183] C. Adler et al. (STAR Collaboration), *Phys. Rev. C* 65 (2002) 041901(R).
- [184] J. Adams et al. (STAR Collaboration), *Phys. Lett. B* 612 (2005) 181.
- [185] S.S. Adler et al. (PHENIX Collaboration), *Phys. Rev. C* 72 (2005) 014903.
- [186] F. Antinori et al. (NA57 Collaboration), *J. Phys. G* 30 (2004) 823.
- [187] E. Schnedermann and U. Heinz, *Phys. Rev. C* 50 (1994) 1675.
- [188] F. Antinori et al. (NA57 Collaboration), *J. Phys. G* 32 (2006) 2065.
- [189] S.V. Afanasiev et al. (NA49 Collaboration), *Phys. Lett. B* 538 (2002) 275.
- [190] C. Meurer et al. (for the NA49 Collaboration), *J. Phys. G* 30 (2004) S1325.
- [191] M.I. Gorenstein, K.A. Bugaev, and M. Gaździcki, *Phys. Rev. Lett.* 88 (2002) 132301.
- [192] H. van Hecke, H. Sorge, and N. Xu, *Phys. Rev. Lett.* 81 (1998) 5764.
- [193] S.A. Bass and A. Dumitru, *Phys. Rev. C* 61 (2000) 064909.
- [194] D. Teaney, J. Lauret, and E.V. Shuryak, *Phys. Rev. Lett.* 86 (2001) 4783.
- [195] D. Teaney, J. Lauret, and E.V. Shuryak, *arXiv:nucl-th/0110037*.
- [196] M. Kliemant, B. Lungwitz, and M. Gaździcki, *Phys. Rev. C* 69 (2004) 044903.
- [197] C. Blume et al. (for the NA49 Collaboration), *J. Phys. G* 31 (2005) S685.
- [198] L. van Hove, *Phys. Lett. B* 118 (1982) 138.
- [199] M. Gaździcki et al., *Braz. J. Phys.* 34 (2004) 322.
- [200] H.J. Drescher, M. Hladik, S. Ostapchenko, T. Pierog, and K. Werner, *Phys. Rep.* 350 (2001) 93.

- [201] H.J. Drescher, F.M. Liu, S. Ostapchenko, T. Pierog, and K. Werner, *Phys. Rev. C* 65 (2002) 054902.
- [202] Y.B. Ivanov and V.N. Russkikh, *Eur. Phys. J. A* 37 (2008) 139.
- [203] H. Petersen, J. Steinheimer, M. Bleicher, and H. Stöcker, *J. Phys. G* 36 (2009) 055104.
- [204] F. Antinori et al. (NA57 Collaboration), *J. Phys. G* 31 (2005) 1345.
- [205] C. Blume et al. (for the NA49 Collaboration), *J. Phys. G* 34 (2007) S951.
- [206] I.G. Bearden et al. (BRAHMS Collaboration), *Phys. Rev. Lett.* 93 (2004) 102301.
- [207] S.V. Afanasiev et al. (NA49 Collaboration), *Phys. Lett. B* 491 (2000) 59.
- [208] T. Anticic et al. (NA49 Collaboration), *Eur. Phys. J. C* 68 (2010) 1.
- [209] P. Braun-Munzinger, D. Magestro, K. Redlich, and J. Stachel, *Phys. Lett. B* 518 (2001) 41.
- [210] A. Tounsi and K. Redlich, *J. Phys. G* 28 (2002) 2095.
- [211] K. Aamodt et al. (ALICE Collaboration), *Phys. Rev. D* 82 (2010) 052001.
- [212] K. Aamodt et al. (ALICE Collaboration), *Eur. Phys. J. C* 68 (2010) 89.
- [213] V. Khachatryan et al. (CMS Collaboration), *JHEP* 1009 (2010) 091.
- [214] J. Takahashi et al. (for the STAR Collaboration), *arXiv:0809.0823*.
- [215] O. Barannikova et al. (for the STAR Collaboration), *J. Phys. G* 31 (2005) S93.
- [216] J. Takahashi et al. (for the STAR Collaboration), *J. Phys. G* 36 (2009) 064074.
- [217] P. Bozek, *Acta Phys. Pol. B* 36 (2005) 3071.
- [218] K. Werner, *Phys. Rev. Lett.* 98 (2007) 152301.
- [219] J. Aichelin and K. Werner, *Phys. Rev. C* 79 (2009) 064907.
- [220] F. Becattini and J. Manninen, *Phys. Lett. B* 673 (2009) 19.
- [221] C. Höhne et al. (for the NA49 Collaboration), *Nucl. Phys. A* 715 (2003) 474c.
- [222] A.R. Timmins et al. (for the STAR Collaboration), *Nucl. Phys. A* 830 (2009) 829c.
- [223] H. Caines et al. (for the STAR Collaboration), *J. Phys. G* 31 (2005) S1057.
- [224] M.A.C. Lamont et al. (for the STAR Collaboration), *J. Phys. G* 32 (2006) S105.
- [225] M. Gyulassy, P. Levai, and I. Vitev, *Nucl. Phys. B* 594 (2001) 371.
- [226] I. Vitev and M. Gyulassy, *Phys. Rev. Lett.* 89 (2002) 252301.
- [227] A. Salgado and U. Wiedemann, *Phys. Rev. Lett.* 89 (2002) 092303.
- [228] B.I. Abelev et al. (STAR Collaboration), *Phys. Rev. Lett.* 97 (2006) 152301.
- [229] P. Abreu et al. (DELPHI Collaboration), *Eur. Phys. J. C* 17 (2000) 207.
- [230] B. Alper et al., *Nucl. Phys. B* 100 (1975) 237.
- [231] I. Vitev and M. Gyulassy, *Phys. Rev. C* 65 (2002) 041902(R).
- [232] B.I. Abelev et al. (STAR Collaboration), *Phys. Rev. Lett.* 99 (2007) 112301.
- [233] J. Adams et al. (STAR Collaboration), *Phys. Lett. B* 637 (2006) 161.
- [234] B.I. Abelev et al. (STAR Collaboration), *Phys. Rev. Lett.* 97 (2006) 152301.
- [235] J. Adams et al. (STAR Collaboration), *Phys. Rev. Lett.* 91 (2003) 172302.
- [236] B. Abelev et al. (STAR Collaboration), *Phys. Rev. C* 76 (2007) 54903.
- [237] J. Adams et al. (STAR Collaboration), *Phys. Rev. C* 70 (2004) 064907.
- [238] P. Sorensen, *arXiv:0905.0174*.
- [239] B.I. Abelev et al. (STAR Collaboration), *Phys. Rev. C* 77 (2008) 054901.
- [240] J. Adams et al. (STAR Collaboration), *Phys. Rev. Lett.* 95 (2005) 122301.



- [241] S. Shi et al. (for the STAR Collaboration), *Nucl. Phys. A* 830 (2009) 187c.
- [242] M. Issah et al. (for the PHENIX collaboration), *arXiv:nucl-ex/0604011*.
- [243] X. Dong, S. Esumi, P. Sorensen, N. Xu, and Z. Xu, *Phys. Lett. B* 597 (2004) 328.
- [244] P. Huovinen, P.F. Kolb, U. Heinz, P.V. Ruuskanen, and S.A. Voloshin, *Phys. Lett. B* 503 (2001) 58.
- [245] P. Huovinen and P.V. Ruuskanen, *Annu. Rev. Nucl. Part. Sci.* 56 (2006) 163.
- [246] J. Adams et al. (STAR Collaboration), *Phys. Rev. Lett.* 92 (2004) 052302.
- [247] B.I. Abelev et al. (STAR Collaboration), *Phys. Rev. C* 81 (2010) 024911.
- [248] I.G. Bearden et al. (NA44 Collaboration), *Phys. Lett. B* 471 (1999) 6.
- [249] C. Pinkenburg et al. (for the E895 Collaboration), *Nucl. Phys. A* 698 (2002) 495c.
- [250] F. Antinori et al. (for the WA97 Collaboration), *Nucl. Phys. A* 661 (1999) 130c.
- [251] T. Anticic et al. (NA49 Collaboration), *Phys. Rev. Lett.* 93 (2004) 022302.